Fall 2013

Engineered metal based nanomaterials in aqueous environments: interactions, transformations and implications

Imali Ama Mudunkotuwa
University of Iowa

Recommended Citation

Mudunkotuwa, Imali Ama. "Engineered metal based nanomaterials in aqueous environments: interactions, transformations and implications." PhD (Doctor of Philosophy) thesis, University of Iowa, 2013.
http://ir.uiowa.edu/etd/5028.

ENGINEERED METAL BASED NANOMATERIALS IN AQUEOUS ENVIRONMENTS: INTERACTIONS, TRANSFORMATIONS AND IMPLICATIONS

by

Imali Ama Mudunkotuwa

A thesis submitted in partial fulfillment
of the requirements for the Doctor of
Philosophy degree in Chemistry
in the Graduate College of
The University of Iowa

December 2013

Thesis Supervisor: Professor Vicki H. Grassian

Graduate College
The University of Iowa
Iowa City, Iowa

CERTIFICATE OF APPROVAL

PH.D. THESIS

This is to certify that the Ph.D. thesis of

Imali Ama Mudunkotuwa

has been approved by the Examining Committee
for the thesis requirement for the Doctor of
Philosophy degree in Chemistry
at the December 2013 graduation.

Thesis Committee: ___________________________________
Vicki H. Grassian, Thesis Supervisor

____
Sarah C. Larsen

____
Christopher M. Cheatum

____
Amanda J. Haes

____
David M. Cwiertny

To my beloved parents,
without whom I would never have come this far
and
my dearest husband Charith
who stood by me through thick and thin

ACKNOWLEDGMENTS

First and foremost, I would like to thank my advisor, Professor Vicki Grassian, for the inspiration, opportunities and the learning experiences provided to me. You constantly challenged me to “raise the bar” and at the same time made me believe in myself so that I can rise up to the challenges. Many thanks also to my past and present committee members, Professors Sarah Larsen, Chris Pigge, Chris Cheatum, Gary Small, Amanda Haes and David Cwiertny, for all of your support, conversations (scientific or not), and help whenever I walked into your office .

A special thank you goes to Dr. John Pettibone, Dr. Shaowei Bian, Dr. Larissa Stebounova and Dr. Jonas Baltrusaitis for all the experiences I gathered from you while working in the lab. Also many thanks to all the members of the Grassian research group, past and present for putting up with endless troubleshooting discussions and practice sessions whenever there is a seminar coming up.

A note of thank you to the Department of Chemistry IT staff including Bryan Ringen for being extremely patient and helpful with all the software issues I face during the time of actually writing down the thesis.

I would also like to extend my heartfelt gratitude to all the faculty members in the Department of Chemistry, University of Colombo, Sri Lanka for paving me the path to my graduate studies. A special note of thank you to Dr. Ramanee Wijesekera; my undergraduate research advisor for all her patience and guidance during my first research experience.

I thank all my friends and family who always believed in me and encouraged me to do my best, especially those in Iowa City. You guys made this far away land feel like a home away from home and was there with me through some of the toughest times in my life. Gayan aiya, Lahiru, Thilinee, Thelma akki, Sanjeewa and Charith, thank you very much for always being there irrespective of the circumstances. Also Thank you Marie for all those “chats” that made me feel so much better afterwards. Also thank you Kokila aunty for helping me out in the times of need.

Most importantly, a very special thank you for my Ammi (Mom) and Thaththi (Dad) for the unwavering and endless support from day one all the way to this very moment. I will always remember how you stayed up late in the night with me when I was studying, picking me up from the library even after you long days of work and giving me anything and everything I need to succeed in my studies. If not for you I would never be where I am today. Also to my darling sister (Bims) and brother (Kassa) who always managed to put a smile on my face whenever I was too stressed or down. Then last but not least to my loving husband Charith who came to my life at the most unexpected moment, stood by me through thick and thin and gave me the strength to be myself. Your unconditional love and faith never cease to amaze me. Without you I would not be complete.

ABSTRACT

Nanoscience and nanotechnology offer potential routes towards addressing critical issues such as clean and sustainable energy, environmental protection and human health. Specifically, metal based nanomaterials are found in a wide range of applications and therefore hold a greater potential of possible release into the environment or for the human to be exposed. Understanding the aqueous phase behavior of metal and metal oxide nanomaterials is a key factor in the safe design of these materials because their interactions with living systems are always mediated through the aqueous phase. Broadly the transformations in the aqueous phase can be classified as dissolution, aggregation and adsorption which are dependent and linked processes to one another. The complexity of these processes at the liquid-solid interface has therefore been one of the grand challenges that has persisted since the beginning of nanotechnology. Although classical models provide guidance for understanding dissolution and aggregation of nanoparticles in water, there are many uncertainties associated with the recent findings. This is often due to a lack of fundamental knowledge of the surface structure and surface energetics for very small particles. Therefore currently the environmental health and safety studies related to nanomaterials are more focused on understanding the surface chemistry that governs the overall processes in the liquid-solid interfacial region at the molecular level.

The metal based nanomaterials focused on in this dissertation include TiO_2, ZnO, Cu and CuO. These are among the most heavily used in a number of applications ranging from uses in the construction industry to cosmetic formulation. Therefore they are produced in large scale and have been detected in the environment. There is debate within the scientific community related to their safety as a result of the lack of

understanding on the surface interactions that arise from the detailed nature of the surfaces. Specifically, the interactions of these metal and metal oxide nanoparticles with environmental and biological ligands in the solutions have demonstrated dramatic alterations in their aqueous phase behavior in terms of dissolution and aggregation. Dissolution and aggregation are among the determining factors of nanoparticle uptake and toxicity. Furthermore, solution conditions such as ionic strength and pH can act as controlling parameters for surface ligand adsorption while adsorbed ligands themselves undergo surface induced structural and conformational changes. Because, nanomaterials in both the environment and in biological systems are subjected to a wide range of matrix conditions they are in fact dynamic entities. Thus monitoring and tracking these nanomaterials in real systems is extremely challenging and requires a thorough understanding of the surface chemistry governing their transformations.

The work presented in this dissertation attempts to bridge the gap between the dynamic processing of these nanomaterials, the details of the molecular processes that occur at the liquid-solid interfacial region and potential interactions. Extensive nanomaterial characterization is an integral part of these investigations and all the materials presented are thoroughly analyzed for particle size, shape, surface area, bulk and surface compositions. Detailed spectroscopic analysis was used to acquire molecular information of the processes in the liquid-solid interfacial region and the outcomes are linked with the macroscopic analysis with the aid of light scattering techniques. Furthermore, emphasis is given to the size dependent behavior and theoretical modeling is adapted giving careful consideration to the details of the physicochemical characterization and molecular information unique to the nanomaterials.

TABLE OF CONTENTS

CHAPTER

LIST OF TABLES

Table

LIST OF FIGURES

Figure

CHAPTER 1

INTRODUCTION

Nanoscience and nanotechnology offer new opportunities for making superior materials for use in a wide range of applications important in industry, energy and health.[1-7] Because of their use, we can expect that these manufactured materials have the potential to get into the environment sometime during production, distribution, use or disposal.[8] Thus, there are many questions as to the EHS of nanomaterials.[9-14] Metal-based nanomaterials including, metals, metal oxides and metal sulfides, in particular are a *large* percentage of nanomaterials that are being already used in consumer products.[9,15-17] Additionally, there is the continued development of these nanomaterials for energy applications and other emerging uses.[18-20] Table 1 provides a list some of the many uses of several different metal-based nanomaterials.

The potential of uncontrolled release of nanomaterials into the environment during their product life cycle has raised some concerns as there is little known about the environmental fate, transformation and toxicity of these materials.[21-23] Based on the evidence of detrimental health effects caused by nanoscale combustion derived particulates and other small particles in air (ultrafines), it is a fair prediction that engineered nanoparticles could negatively impact the environment and human health.[24-27] Table 1 list several literature references for some recent laboratory studies on the environmental, health and safety studies of some metal-based nanomaterials.[1,25,26,28-43] In addition to these laboratory studies, there is recent concrete field evidence that engineered nanoparticles can make their way into the atmosphere and the hydrosphere.[44,45] This suggests risk of exposure to these materials via inhalation and ingestion by drinking water. Therefore, a forward looking approach is required for the development of nanotechnology that involves the balance between technological advancements of this innovative field of science along with an emphasis on the data and knowledge needed to better understand environmental, health and safety issues of these materials.

Table 1.1: Examples of metal-based nanomaterial applications and literature references of some recent EH&S studies.

Metal-Based Nanomaterial	Applications	Recent EHS Studies
Ag	Antibacterial and disinfecting agent (textiles, healthcare, refrigerators, air conditioners, washing machines), anti-corrosive coating (paints and coatings), microelectronic industry (wiring, encapsulation and connections), catalysis.	1, 25, 28-30
Al, Al_2O_3	Catalyst supports, antibacterial and disinfecting agent (textiles, plastics, coatings), transparent conductive and optical coating (optical lenses, windows and flooring), wear-resistant additive, heat transfer fluid, cosmetic filler, water-proof material.	26, 31
CeO_2	Catalysis and catalyst supports, solid oxide fuel cells (electrode materials), sintering additives, heat resistant alloy coatings, uv absorbent, superconducting materials (buffer layer)	32-35
Cu, CuO	Antibacterial and disinfecting agent (textiles, plastics and coatings), microelectronic industry (wiring and connections), catalysis (rocket propellant combustion), gas sensors, thermo-electronics, superconductors.	36-39
Fe, Fe_2O_3, Fe_3O_4	Environmental remediation (removal of actinides from waste water), magnetic data storage, biomedical applications (MRI contrast agents, magnetic separations, targeted drug delivery), semiconductor, microwave devices.	37, 39
TiO_2	Photocatalysis, antibacterial and disinfecting agent (paint and coatings, ceramics, glass), cosmetics, uv resistors (sunscreens), air purification, semiconductors, astronautics, and solar cells.	35, 37, 38, 40
ZnO	Electronic and electrical industry, cosmetics and cosmoceuticals (sunscreens, anti-agers, moisturizer), piezoelectric, high temperature lubricants, flame retardant, dental cement, photocatalytic decontamination, solar cell electrodes, paint pigments.	33, 35, 37, 38, 40, 41

Toward this end, it is important to recognize that there are major challenges for understanding nanomaterials in the environment as a result of the large surface to volume ratio and the large contribution of the surface free energy in the overall total free energy of the particle.[46-49] For any given particle, the total free energy is the sum of the free energy contributions from the bulk and surface of the particle:

$$G_{particle} = G_{bulk} + G_{surface} \qquad (Eq: 1.1)$$

For nanoparticles the contribution of the $G_{surface}$ to $G_{particle}$ is on the order of that of G_{bulk} because as the size of the particles decrease the percentage of atoms at the surface increases. For example, consider a 1 cm^3 cube, the percentage of atoms at the surface is miniscule, on the order of ~10^{-5}%. However, if this cube is divided into much smaller cubes with 10 nm sides then ~10% of the atoms will be on the surface. Figure 1.1 taken from Nützenadel *et al*. illustrates this decrease in surface atom percentage of palladium clusters as the size changes from the micron to nanoscale.[50] From this plot, it can be easily seen why the surface free energy component for these very small particles in the nanoscale size regime, especially for those with dimensions less than 10 nm becomes a significant component of the total free energy. Furthermore, for a spherical particle, e.g. a liquid droplet, $G_{surface}$ can be expressed as:

$$G_{surface} = \gamma A \qquad (Eq: 1.2)$$

where γ is the surface energy and A is the surface area. However, most metal-based nanoparticles are in fact not spherical but instead have facets with specific crystallographic orientations. Thus, $G_{surface}$ cannot be expressed simply as in Eq: 1.2 but instead will have several terms for each crystallographic plane contributing to the overall

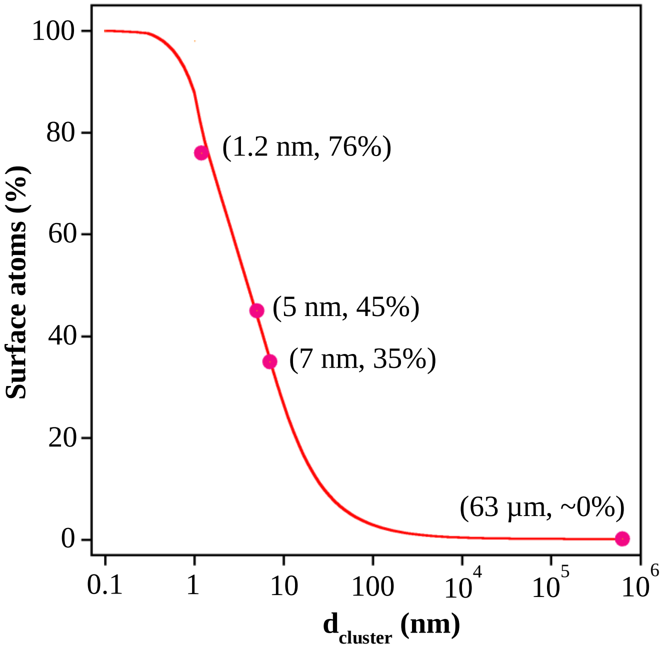

Figure 1.1: Percentage of surface atoms as a function of cluster diameter of palladium clusters. (Reprinted with kind permission from Springer Science + Business Media: C. Nützenadel, A. Züttel, D. Chartouni, G. Schmid and L. Schlapbach, *Eur. Phys. J. D*, **8(**2), 2000, 245-250, Fig.1)

surface free energy. Additionally for metal-based nanoparticles, the size and shape of nanomaterials give rise to unique surface electronic states that consequently affects the surface energy. Therefore, in a field of science which is “all about the size”, it is essential to have an in depth understanding of the surface chemistry governing the processes.[51] A successful approach requires a theoretical framework supported by experimental data.

1.1 Detailed Nature of Surface Structure and Energetics at the Nanoscale

As already noted metal and metal oxide nanoparticles are not spherical but instead have faceted structures with different interaction energies depending on shape and different surface planes as well as the details of surface adsorption and speciation. Nanoparticles of metals and metal oxides are known to exhibit unique reactivity and enhanced chemical activity because of the presence of different surface crystal planes and surface defects as well as surface reconstruction and surface relaxation between layers. Below is an overview of some important aspects of nanoparticle surfaces as it relates to understanding the properties of nanomaterials. An interesting fact to note is that many of these unusual properties are associated with those having dimensions of less than 10 nm.[52-55]

1.1.1 Surface Structure and Energetics in Controlling Phase Stability

The thermodynamic crossovers in phase stability of various materials as a function of decreasing size highlight the important role that surface free energy plays. For nanoscale particles, this crossover leads to the stabilization of what are normally considered high energy phases for a particular. For example, anatase, the lowest energy phase for nanoscale TiO_2, is stabilized relative to rutile, the lowest energy phase for bulk TiO_2, γ-Al_2O_3 is stabilized relative to α-Al_2O_3 and tetragonal and cubic ZrO_2 are stabilized relative to the monoclinic phase.[56-58] Navrotsky *et. al.* discuss quite extensively on the competition between surface energy and the energetics of phase transformations of various metal oxides and oxyhydroxides.[56,59] In their studies, spontaneous oxidation of Co^{2+} and reduction of H_2O has been observed for CoO nanoparticles smaller than 8 nm which is not seen with larger particles. Furthermore, 13 nm Mn_2O_3 particles were observed to reduce partially to Mn_3O_4 when heated in air at 975 K whereas 38 nm particles were not reduced until above 1138 K which is the expected temperature for this conversion according to standard thermodynamic data. Chen *et al.* has shown under some conditions there can be self-limiting oxidation behavior of Cu nanoparticles at 298 K leading to thinner oxide layers than the bulk which was related to the compressive stress in the Cu_2O (111) layers formed.[60] These results provide important evidence for size dependent redox properties for metal and metal oxides on the nanoscale. In general, the measured surface energy of a material is an average of different crystal planes, defects, edges, corners, kinks, pits and steps. Although an average value can satisfactorily explain the behavior of bulk materials, it can be misleading when applied to nanomaterials. This has been evident in the several orders of magnitude error in oxygen fugacity and the hundreds of degree temperature difference observed in the calculated redox phase equilibrium of transition metal oxides using bulk thermodynamic parameters.[59] Additionally, a series of studies on different morphologies of ZnO and TiO_2 nanocrystals has shown significantly different surface enthalpies. Zhang *et. al.* has studied the hydrous and anhydrous surfaces of ZnO nanoparticles, nanoporous composites, nanorods, and nanotetrapods.[61] Park *et. al.* has looked at TiO_2 nanoparticles, nanowires and sea-urchin-like structures.[62] Change in surface energies with morphology was observed to be significantly higher in ZnO than in TiO_2. In both of these studies, the trends in surface energy variation were successfully correlated to the exposed crystal planes of the materials.

1.1.2 Surface Adsorption, Relaxation and Reconstruction

The presence of surface functional groups and adsorbates impact the stability of nanomaterials. A study on the stability of nanocrystalline single-phase zirconia (ZrO_2) by Radha *et.al.* showed that the stability crossover between monoclinic and tetragonal zirconia occurs at a particle size of 28 ± 6 nm and 34 ± 5 nm for hydrous and anhydrous states respectively.[63] The different crossover size thresholds for hydrous and anhydrous states highlights the impact of the stabilizing effects of water adsorption and hydroxylation that contributes towards lowering the surface energy for nanoscale particles. Strong water adsorption by less stable phases has been observed in several studies.[57,61,62] Fang *et. al.* observed that the wettability of metal oxides are closely related to the surface energy of the nanoparticles.[63] However, regardless of the magnitude of the surface energy there are a variety of synthetic routes that allow for kinetic control enabling the formation of nanomaterials with less phase stability (high surface energy). The prevalence of these less stable nanomaterials largely depends on surface stabilization with capping agents, ions or water molecules yielding materials which are metastable. Removal of these surface stabilizing groups under certain conditions can result in a phase transformation of the nanomaterial. Fang *et. al.* highlight the importance of evaluating the surface energies of as received nanomaterials under ambient conditions for environmental studies over the more frequently studied “pure” materials at elevated temperatures and low pressures.[63]

A study of the detailed surface structure of 3 – 5 nm Au crystals using diffraction intensity oscillations around the Bragg peaks has shown inhomogeneous relaxations by bond length shortening for edge and surface atoms.[64] These relaxations are found to be coordination and facet dependent with the largest bond contractions observed for edge atoms (~0.2 Å), the next largest for the (100) surface atoms (~0.13 Å) and the smallest for atoms in (111) facets (~ 0.05 Å). Additionally, experimental diffraction peaks of 3.5 nm Au nanocrystals were compared to two models. The first model was for the unrelaxed surface and the second model accounted for shorter distances between Au atoms at the surface and the underlying plane below. The comparison showed that the experimental data were best represented by the MD simulation that took into account relaxation. Because the proportion of surface atoms is higher than the bulk in nanoscale, the bulk atoms are affected by such relaxation processes as seen by changes in the lattice parameters of these materials. Gilbert *et. al.* has studied ligand coated ZnS nanoparticles which showed that such relaxations, despite the surface stabilizing capping agents result in internal strain and stiffening of the lattice structure in the nanoparticles.[65] Surface-bound ligands have also shown to contribute towards the internal strain by enhancing it in the order of covalent < electrostatic < van-der-Waals interactions with the surface atoms which is not unexpected as covalent bonds stabilize surface atoms to a greater extent.[66] Understanding of these effects is important as they impact many nanoscale phenomena (interfacial stability, reactivity, mechanical and electronic properties) and are directly related to the surface structure and surface energy of the particles.

1.2 Nanoparticles in the Aqueous Environment

Generally the nanomaterial interactions with living systems are mediated through the aqueous phase.[67] For example when they are inhaled they get into the lung fluid and oral ingestion lead them to the blood plasma via saliva and other various fluids in the gastrointestinal tract. Once in the plasma, the nanoparticles can potentially find their way into the cells where the interactions are mediated in the cytosolic fluid.[68,69] Furthermore, plant roots can take up these nanoparticles which can result bioaccumulation and biomagnification.[70] The exposure to engineered metal oxide nanoparticles can be both intentional as well as unintentional originating from their applications and disposal respectively.[8,71] The ultimate fate and the toxicological effects of these nanomaterials in both the environmental and biological media are directly affected by their transformation that occurs via surface ligand adsorption/displacement, aggregation and dissolution.[72-75] Although adsorption and dissolution are well understood for the bulk scale materials the same cannot be said about those at the nanoscale. Furthermore aggregation is a nanoscale phenomenon taking place to reduce the high surface energy. Figure 1.2 illustrates the detailed nature of these transformations at the liquid-solid interface compared to the broad categorization. As extensively discussed in Section 1.1, their unique surface chemistry can manifest significant deviations from the properties of their bulk counterparts. Therefore the exact mechanisms, thermodynamic parameters and kinetics of these transformations for nanoscale materials need investigation and are currently an extremely active area of research.

Nanomaterials in most cases are surface functionalized to inhibit aggregation.[31,76-79] In the absence of functionalization, even pristine nanomaterials have surface functional groups ranging from hydroxyls to acetates, carbonates to long-chained polymeric surfactants that spontaneously adsorb on to the surface during the synthesis. Upon release into the environment, especially into aqueous environments these initial surface ligands can potentially be displaced or undergo changes.[72,80-83]

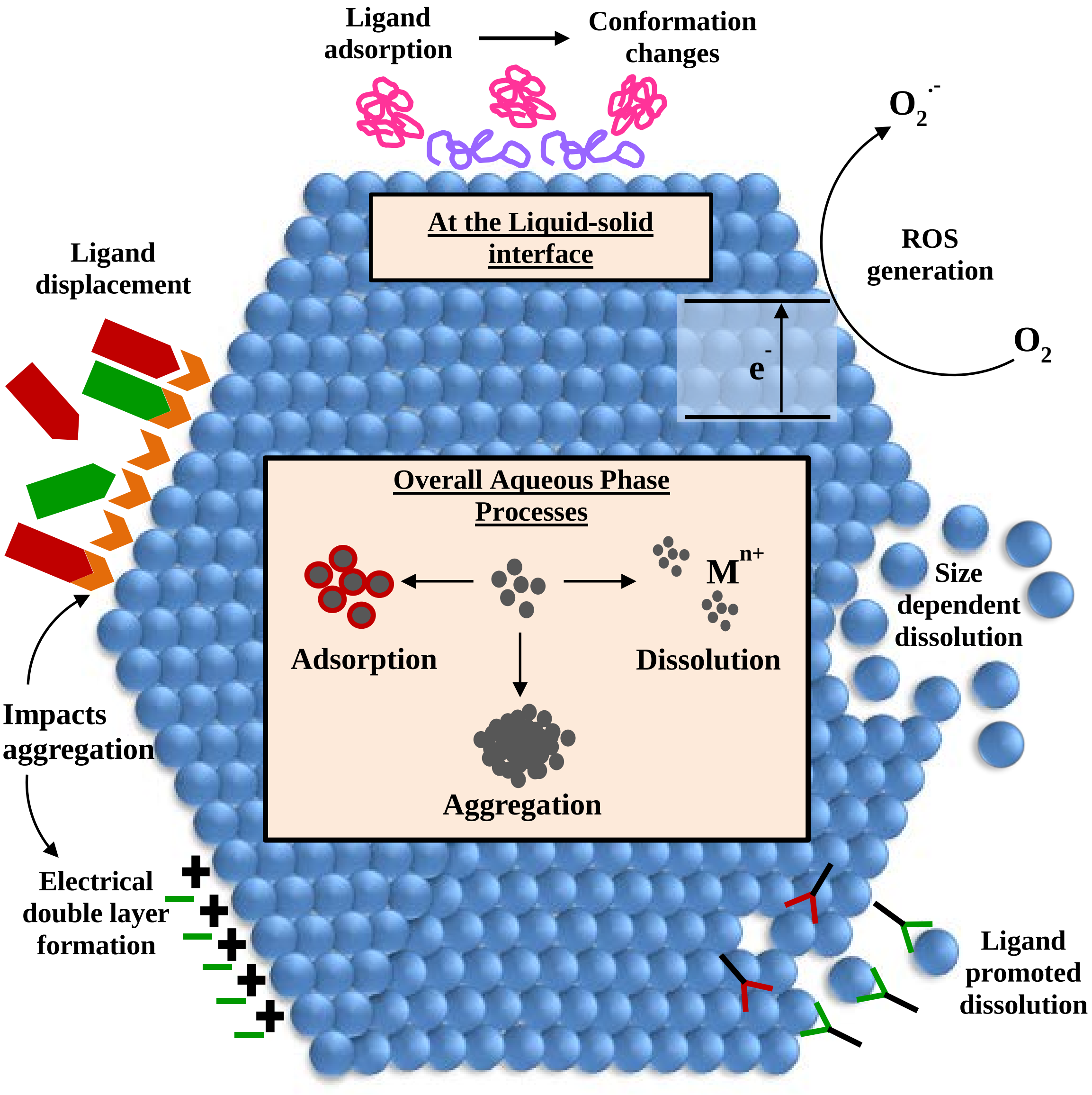

Figure 1.2: Aqueous phase transformations of a metal based nanoparticle. The inset shows the overall processes which are categorized as ligand adsorption, aggregation and dissolution. However these overall processes are quite complex as illustrated by the detailed processes observed at the liquid- solid interface at the nanoparticle surface.

Natural water systems contain a wide range of organic and inorganic ligands starting from simple nitrates, sulfates, oxalates and citrates to more complex humic and fulvic acids.[84-87] Furthermore, if these nanomaterials are internalized in biological systems, a series of complex ligand displacements can take place where a wide variety of proteins and enzymes can interact with these surfaces.[88-91] In biological systems, surface ligand displacement by proteins lead to the formation of "protein corona" which is considered to define the biological identity of the particle.[92] Additionally, ligand displacement reactions in aqueous systems can convert the "native form" of the nanomaterials into a "water-soluble/insoluble form" or a "biocompatible form".[93-95] Surface ligand adsorption has been shown to impact nanomaterial behavior in vital ways as this will impact everything from secondary size (through aggregation) to water solubility to soil mobility and to the ability of nanomaterials to get into cells.[96] Thus, understanding the environmental impact of nanomaterials requires knowledge on the impacts of surface ligand displacement.

Dissolution results in the generation of metal atoms or ions that can have known toxic effects.[30,97-99] From the particle perspective, nanoparticle dissolution will result in the formation of nanoparticles that are smaller than the original primary particles.[100] These even smaller particles will have potentially different properties.[48,51] The presence of different crystallographic planes can lead to anisotropic dissolution resulting in changes in the particle morphology as the particle gets smaller. Dissolution can also potentially impact nanoparticle aggregation by causing de-aggregation as the particles within the aggregate dissolve.[101] For nanoparticle aggregation, again taken from the particle perspective, there is a change in (secondary) size and density with a resulting decrease in available surface area, which may impact surface chemistry including nanoparticle dissolution. These issues – the impact of nanoparticle aggregation on dissolution and the impact of nanoparticle dissolution on aggregation – are not well understood but are important in the broader context of understanding the mobility of nanoparticles in the environment. Several studies have shown that nanoparticle aggregation decreases both the rate and extent of dissolution.

Rubasinghege *et. al.* have clearly shown that proton-promoted dissolution of goethite (α-FeOOH) rods are greatly hindered as a result of aggregation.[102] In particular, dissolution of nanorods in different aggregated states was compared to that of microrods. In this study, it was shown that isolated nanorods showed an enhanced dissolution rate on a per mass and per surface area basis compared with larger microrods. This enhanced activity (~3 times greater than surface area effects) was assigned to the larger fraction of (021) surface planes which are more active and readily dissolve. However upon aggregation of the nanorods the microrods dissolved to a much greater extent. This aggregation reduces the exposed active surfaces to the solution and changes viscosity and diffusion coefficients of the species within the confined regions of the aggregates and thereby slows the dissolution process. In another study, it has been shown that dissolution is inhibited for galena (PbS) nanocrystals when the nanocrystals surfaces are closely adjacent to each other and dissolution rates are facet dependent.[103] Pre-dissolution crystal structures observed by HRTEM (Figure 1.3) show these nanocrystals to be terminated by six primary (100) facets, eight small (111) facets and twelve small (110) facets forming a cub-octahedral shape (Figure 1.3a and 1.3c). Upon dissolution (110) and (111) faces were observed to develop at a faster rate and dissolution occurred symmetrically around the nanocrystals in the absence of aggregation (Figure 1.3b). The images of aggregated nanocrystals show faster dissolution of the faces exposed to the bulk solution relative to the faces within the confined regions with surface separations of 1-2 nm (Figure 1.3d). It has been suggested that solution properties are altered within the confined regions of the aggregates in addition to the reduction in the exposed surface area.

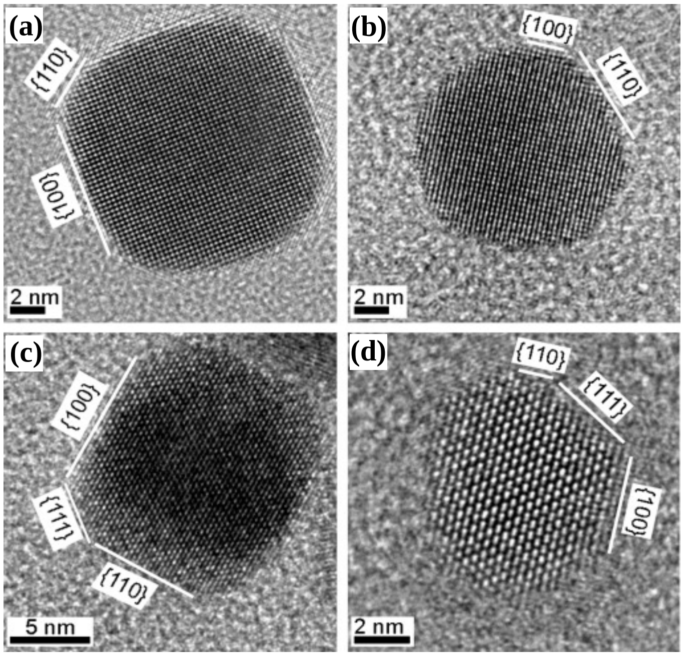

Figure 1.3: HRTEM images of isolated PbS nanocrystals (a) prior to dissolution viewed along [100] axis (b) after 3 hour dissolution viewed along [100] axis (c) prior to dissolution viewed along [110] axis (d) after 3 hour dissolution viewed along [110] axis. (Reprinted from J. Liu, D.M. Arguete, J.R. Jinschek, J. D. Rimstidt and M. F. Hochella, Jr, The non-oxidative dissolution of galena nanocrystals: insights into mineral dissolution rates as a function of grain size, shape and aggregation state, *Geochim. Cosmochim. Acta*, **72**(24), 5984-5996. Copyright (2008), with permission from Elsevier.)

Not only can aggregation impact dissolution, dissolution can cause aggregates to come apart. Figure 1.4 clearly illustrates this behavior for copper nanoparticles. These copper nanoparticles have an oxide coating and readily aggregate at circumneutral pH. TEM images of Cu nanoparticles (12 nm in diameter) in pH 7.0 water (Figure 1.4a) shows tightly aggregated particles making it difficult to distinguish specific nanoparticles. In contrast, images of particles that have been in pH 3.0 in the presence of citric acid (Figure 1.4b) are easily distinguishable and no longer appear as aggregated but instead as individual particles.

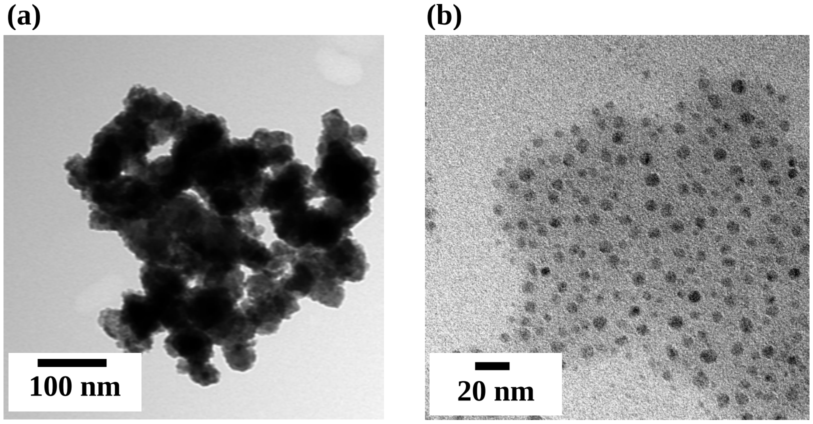

Figure 1.4: Aggregation and dissolution of Cu nanoparticles in different solutions. TEM images of Cu nanoparticles in (a) pH 7.0 water (b) 1.5 mM citric acid at pH 3.0.

Ligands play a dual role in these processes, as an adsorbate causing both a de-aggregation to occur while enhancing dissolution through a ligand-promoted process. Because both dissolution and aggregation depend on aqueous conditions such as pH, ionic strength and ligands there is a need for detailed investigations of nanoparticle dissolution and aggregation with emphasis on particle size and morphology under various environmental conditions.[104] Especially very small nanoparticles (dimensions < 10 nm) have the potential of being uniquely distinct from the bulk.

1.3 Theoretical Models of Finer Particles in Aqueous Phase

1.3.1 Ostwald-Freundlich Relation - Size Dependent Dissolution:

Toxicity of metal-based nanoparticles does not always originate from the particle itself but instead from the ability of these small particles to dissolve leading to ions in solution. For example, ZnO and CuO nanoparticles are considered nontoxic, however, because of their high solubility the producing Zn^{2+} and Cu^{2+} ions are found to induce various cytotoxicity.[14,36,38,41] Classically, a modified form of Kelvin equation (3), also known as the Ostwald-Freundlich equation, is used to describe the size dependent solubility of nanoparticles.[105]

$$\frac{S}{S_0} = exp\left(\frac{2\gamma V}{RTr}\right) \qquad (Eq: 1.3)$$

where S is the solubility (in mol kg^{-1}) of spherical particles with radius r, S_0 is the solubility of the bulk, V is the molecular volume (in m^3 mol^{-1}), γ is the surface free energy in mJ m^{-2}, R is the gas constant and T is the temperature. According to eq. 1.3, the solubility increases exponentially as the particle size decreases. It is evident in this relationship that the surface energy and particle size strongly determine the solubility of the nanomaterials. The most significant enhancement in the calculated solubility is expected for very small particles (size < 10 nm).

There is some experimental evidence that suggests nanoparticle dissolution does not follow this simple model and some studies have reported suppressed dissolution as the particles become smaller.[106] Schmidt and Vogelsberger describe an unusual size dependent dissolution maximum above the saturation concentration for nanoscale TiO_2, a commonly considered insoluble metal oxide.[107] In another study, Erbs *et. al.* showed no discernible size dependence on the rate of reductive dissolution for 3.4 – 5.9 nm ferrihydrite ($Fe_5HO_8.4H_2O$) particles.[108] However, the deduced pre-exponential factor which relates to the reagent surface encounters was shown to be six fold greater when comparing 3.4 nm to 5.9 nm. They propose that this enhancement is a result of water molecules ordering at the nanoparticle surface impacting diffusion properties in the near surface region giving rise to a size dependent pre-exponential factor.

Deviations from predictions afforded by eq. 1.3 can be expected due to a lack of detailed knowledge of the surface free energy (γ), its size dependence as well as its dependence on the details of the surface structure (e.g. surface defects and different crystal facets present).[103] In particular, nanoparticles surfaces feature a relatively larger number of edge and corner atoms which are well known to be preferred detachment sites.[108] The enhanced activity of these sites is not accounted for. Aggregation, on the other hand, reduces the effective surface area of the nanoparticles exposed to the solution.[102,103,105] The chemical behavior of the aqueous solution in the confined regions within aggregates is observed to be different because their viscosities are increased.[104,109] Therefore, the diffusion coefficients of the species within this region are likely to be significantly lowered compared to the bulk solution resulting in a decreased rate of dissolution. Additionally, the concentration gradient of the dissolved species from the particle surface to the bulk solution is much smaller in these confined regions as a result of the overlap of diffusion layers of the particles.[103] This concentration gradient is considered to act as a driving force for dissolution and a decrease in the gradient results in a reduction of the flux of atoms or ions away from the surface.

1.3.2 Derjaguin-Landau-Verwey-Overbeek (DLVO) Theory:

Besides dissolution, aggregation of metal-based nanoparticles readily occurs in the aqueous solutions.[110-114] Aggregation destabilizes aqueous particle suspensions leading to flocculation and sedimentation.[84,114,115] Particle suspension stability is usually modeled by classical Derjaguin-Landau-Verwey-Overbeek theory (DLVO theory) or extended DLVO theory.[77,99] In classic DLVO theory, particle suspension stability is determined by the net electrostatic surface interactions between the particles. Assuming spherical particles, the total interaction energy is given as the sum of attractive van-der-Waals forces and electrostatic repulsive forces between these spheres:

$$V_{total} = V_{vdw} + V_{elec} \qquad (Eq: 1.4)$$

Attractive van-der-Waals forces are given by,

$$V_{vdw} = -\frac{A_H}{6}\left[\frac{2a_1a_2}{R^2-(a_1+a_2)^2}+\frac{2a_1a_2}{R^2-(a_1-a_2)^2}+ln\frac{R^2-(a_1+a_2)^2}{R^2-(a_1-a_2)^2}\right] \qquad (Eq: 1.5)$$

where A_H is the overall Hamaker constant, a_1 and a_2 are the particle radii and R is the distance between the centers of the particles. Values for the Hamaker constant are available in the literature but for less common materials, this can be calculated by:

$$A_{121} = (\sqrt{A_{22}} - \sqrt{A_{11}})^2 \qquad (Eq: 1.6)$$

where A_{121} is the overall Hamaker constant for the aggregation of two nanoparticles of composition “1” when suspended in a medium “2”. A_{11} and A_{22} are Hamaker constants of the individual nanoparticles in a vacuum.[115]

Electrostatic repulsive forces, which depend on the particle radius (a) and the double layer thickness ($1/\kappa$), are given by:

$$V_{elec} = 4\pi\varepsilon\psi_0\frac{a_1a_2}{a_1+a_2}ln[1+\exp(-\kappa x)\ \ ] \ \ (in\ the\ case\ of\ \kappa a > 5) \qquad (Eq: 1.7)$$

$$V_{elec} = 4\pi\varepsilon\Upsilon_1\Upsilon_2a_1a_2\left(\frac{k_BT}{e}\right)^2\frac{\exp(-\kappa x)}{a_1+a_2+x} \ \ (in\ the\ case\ of\ \kappa a < 5) \qquad (Eq: 1.8)$$

$$Y_i = \frac{8\tanh\left(\frac{e\psi_0}{4k_BT}\right)}{1+\left[1-\frac{2\kappa a_i+1}{(\kappa a_i+1)^2}tanh^2\left(\frac{e\psi_0}{4k_BT}\right)\right]^{\frac{1}{2}}} \qquad (Eq: 1.9)$$

$$\kappa = \left[\frac{1000e^2N_A(2I)}{\varepsilon k_BT}\right]^{1/2} \qquad (Eq: 1.10)$$

where ε is the permittivity of solvent, ψ_0 is the surface potential, k_B is the Boltzmann constant, x is the distance between the particle surfaces, a is the radius of the particles, N_A is the Avogadro's constant, I is the ionic strength of the solution and κ is the inverse Debye length.

Aggregation occurs when the attractive forces between particles are larger than the repulsive forces. At close approach, if the repulsive forces are greater than the attractive forces, it will create an energy barrier for particle aggregation and, without collisions with sufficient energy, aggregation will not occur.[77] In such situations, particles will not aggregate and suspensions will be stable. If particles have sufficient energy to overcome this energy barrier, then the particles will aggregate.

The solution pH and ionic strength can significantly impact the magnitude of these forces which will ultimately determine the net interaction force.[74,77,99] If one considers the details of the surface composition of metals and metal oxides in aqueous solutions, these particles are often hydroxylated through reactions with water as shown below:

$$M + H_2O \rightarrow M - OH + H^+ \qquad (Eq{:}\,1.11)$$

Based on the solution pH, the hydroxylated surface can undergo protonation or deprotonation:

$$M - OH + H^+ \rightarrow M - OH_2^+ \qquad (Eq{:}\,1.12)$$

$$M - OH \rightarrow M - O^- + H^+ \qquad (Eq{:}\,1.13)$$

The pH at which the surface charge density of the nanoparticles is zero is defined as the point of zero charge (pH_{ZPC}) or isoelectric point (pH_{IEP}).[111] At this pH, the highest degree of aggregation is observed since there are no repulsive forces to keep the particles apart.[99,115] In the absence of specific adsorption of ions in solution pH_{ZPC} is the same as pH_{IEP}. When $pH_{solution} < pH_{ZPC}$ the surface charge is positive and for $pH_{solution} > pH_{ZPC}$ the surface charge is negative. Therefore pH of the suspension plays a key role in determining the repulsive interactions between particles. The pH_{ZPC} of metals and metal oxide nanoparticles have a broad range of values depending on size, phase, surface face and method of preparation.[111,116,117] The aggregation results in colloidal suspensions with wide size distributions.[118,119]

Classical DLVO theory has been further extended to account for the non-electrostatic interactions.[77,99] When the nanoparticle surfaces are coated with surface adsorbed ligands, the interactions between the solvent molecules and the ligands can be responsible for the steric stabilization of the particles which arises from osmotic and elastic contributions.[31,77,120] Osmotic contribution depends on the molecular volume of solvent (v_1), volume fraction of polymer within the coating layer (Φp), the Flory-Huggins interaction parameter (χ), particle radius (a), polymer layer thickness (w) and the distance between the particle centers (R) and can be given as follows for three different regions:[31,120-122]

$$V_{osm} = 0, (2w \leq d) \qquad (Eq: 1.14)$$

$$V_{osm} = \frac{4\pi R k_B T \Phi_p^2}{v_1}\left(\frac{1}{2} - \chi\right)\left(w - \frac{d}{2}\right)^2, (w \leq d < 2w) \qquad (Eq: 1.15)$$

$$V_{osm} = \frac{4\pi R k_B T \Phi_p^2}{v_1}\left(\frac{1}{2} - \chi\right) w^2 \left(\frac{d}{2w} - \frac{1}{4} - ln\left(\frac{d}{w}\right)\right)^2, (d < w) \qquad (Eq: 1.16)$$

The elastic repulsive energy results (V_{elas}) from the entropy loss that occurs upon the compression of the coating layer and is considered to give a significant contribution when the distance between particles does not exceed the particle diameter. Taking all these interactions into consideration the extended DLVO theory calculates the total interaction energy:

$$V_{total} = V_{vdw} + V_{elec} + V_{osm} + V_{elas} \qquad (Eq: 1.17)$$

Extended DLVO theory can be useful in studying the aggregation in aqueous environments because dissolved organic matter and proteins that can adsorb on nanoparticle surfaces are often polymeric in nature with a large number of functional groups consisting carboxylate and phenolic groups.[84,115,123] However, the extent of steric stability will greatly depend on the mode of adsorption; chemisorbed compared to more weakly physisorbed. Changes in the environmental milieu can result in displacement of the steric stabilizers and release the potentially reactive nanomaterials.

1.4 Implications for the Environmental Fate, Transport and Toxicity

Released nanoparticles in the environment, even those of the same bulk composition, can have different properties based on its initial application and the surface properties.[9] They can be primary particles, aggregated particles, particles embedded in a matrix or functionalized.[16] Depending on environmental factors such as pH, ionic strength, presence of complexing molecules the surface chemistry of these particles can be modified resulting in de-aggregation, aggregation and surface ligand adsorption. The final form of the nanoparticles in the environment will largely impact their distribution, uptake and toxicity.[124] Surface ligand adsorption impacts both the dissolution and aggregation of these materials. Dissolution results in mobilization of ions and smaller nanoparticles and with the aid of complexing molecules they can be taken up by plants and animals as well. Nanomaterials are expected to have enhanced dissolution properties relative to the bulk but detailed studies on the relationship between nanoparticle structure, nanoparticle size and dissolution are lacking.[105] Aggregation in turn affects dissolution of these nanomaterials. Therefore, despite the broad classification introduced in section 1.2 surface ligand adsorption, dissolution and aggregation are processes which are dependent on one another. Thus changes in one process can potentially affect the others. This makes investigations in the aqueous phase to be extremely challenging. Furthermore the complexities of aqueous environmental matrices can intervene with obtaining any useful information on nanomaterial fate, transport and toxicity.

There is a debate in the scientific community on existing high concentration-high toxicity relationship because high concentration of nanomaterials leads to high degree of aggregation that can potentially result in "bulk-like" material with no "nano effects" whereas the actual risks are affiliated with much lower level concentration of the same materials.[23,125] Although these terms "bulk like" materials with no "nano effects" is used, they are not scientifically useful from a number of perspectives. While aggregation will result in a much larger secondary particle size, the density of the aggregate will not be the same as the bulk but instead will depend on the packing of the nanoparticles. Second, the highly active surfaces of the nanoparticles that make up the aggregate can disappear in some cases (e.g. PbS – *vide supra*) in other cases they can simply be buried (e.g. Cu – *vide supra*). The extent of the accessibility of these interfaces will depend on the density of the aggregate and the packing of the particles that make up the aggregate. Under conditions where dissolution occurs within the aggregates, these buried reactive surfaces can become exposed (Figure 1.4).

Furthermore, it can be debated that there are at least two scenarios of concern with respect to nanomaterials in the environment. The first is that there will be a persistent low level of nanomaterials in the environment that have the potential to be harmful from a long term exposure level perspective. The second scenario relates to large plumes of nanomaterials getting into the environment as a result of an episodic event that includes a disaster such as an explosion of a factory producing large quantities of nanomaterials. Since ***metal-based nanomaterials are dynamic not static entities*** and change significantly over time and under different environmental conditions it is important to understand their interactions leading to the respective transformations in order to better understand and regulate the implications.

1.5 Introduction to Thesis Chapters

The broad, overall objective of the research presented in this dissertation was the determination of fate and transformation of engineered metal based nanomaterials in aqueous environments as a function of physical properties (*f[size, morphology]*) and solution conditions (*f[pH, ionic strength, solution ligands]*). All projects were conducted both macroscopically as well as at the molecular scale to understand the fundamentals governing the environmental processing.

In chapter 2, the general experimental protocols and instrumental techniques used to achieve the overall objective are outlined. The experiments were classified into four sections; (1) physicochemical characterization (2) aqueous phase ligand adsorption (3) quantitative nanoparticle dissolution and (4) nanoparticle-nanoparticle interactions and aggregation. Physicochemical characterization was conducted using transmission electron microscopy (TEM), powder X-ray diffraction (p-XRD), BET surface area measurements and X-ray photoelectron spectroscopy (XPS). Both surface and bulk characterizations are conducted to identify any specific surface contributions towards environmental processing. The well characterized materials are used in the quantitative batch studies to investigate both ligand adsorption and nanoparticle dissolution using high performance liquid chromatography (HPLC) and inductively coupled plasma optical emission spectroscopy (ICP-OES) respectively. Spectroscopic analyses with attenuated total reflectance Fourier transform infrared (ATR-FTIR) spectroscopy was used to probe the liquid –solid interphase at the nanoparticle surface to understand the molecular interactions. Dynamic and static light scattering techniques were used to study the aggregation behavior under a wide range of solution conditions. Surface charge measurements were used to compliment the aggregation behavior observed.

In chapter 3, the focus is on understanding the impact of ligand adsorption on the aggregation and the effect on mobilization. To probe these behaviors TiO_2 nanoparticles were used due to their heavy use leading to the high risk of release into the environment.

The adsorption of citric acid which is a representative ligand in both environmental and biological media was studied as a function of solution pH. The pH dependent adsorption of citric acid on TiO_2 nanoparticles as shown in the study drastically altered the aggregation behavior of the nanoparticles. These alterations were also in turn pH dependent. Furthermore, the spectroscopic studies revealed that the surface speciation of adsorbed citric acid can be different from the solution. The DLVO theory calculations using the surface charge measurement complimented the observation of dynamic and light scattering techniques.

In chapter 4, the implications of aging on the environmental processing of metal based nanoparticles are investigated. Here an oxidized sample of copper nanoparticles (thick CuO coating) was compared to newly purchased Cu nanoparticles (thin oxide coating). Both samples were purchased from the same vendor and the aged sample was stored under ambient conditions for 3 years. The extensive physicochemical characterization revealed that both physical and chemical properties of these particles have changed. These changes were in fact reflected in their environmental processing with lower levels of dissolution, different modes of ligand adsorption and different aggregation behavior. This provides good evidence of metal oxide nanoparticles as dynamic entities with constantly changing properties. The ligands used in this study were citric and oxalic acid.

In chapter 5, the size dependent dissolution of ZnO nanoparticles and the effect of complexing ligands on the size dependent behavior are discussed. The dissolution was conducted at pH 7.5 and in the absence of ligands was indeed size dependent. However, the size dependent dissolution was completely masked in the presence of citric acid which enhanced the dissolution by several folds. Nevertheless this effect was very much ligand specific as the size dependence was retained in the presence of bovine serum albumin (BSA). Furthermore, in this study the dissolution measurements were used to estimate the surface energy of the ZnO nanoparticles using a classical model. This resulted in an underestimation of surface energy as a result of lack of surface details accounted for in the model. This highlighted the importance of incorporating surface contributions in the prediction models for nanoparticles in solution which are obviously quite different from the fine particles in micron scale.

In chapter 6, a detailed spectroscopic investigation of histidine adsorption on TiO_2 nanoparticles in conjunction with batch adsorption studies is presented. This was aimed at better understanding the nano-bio interactions as histidine is an essential amino acid found as a component in many biomolecules. The spectroscopic data suggested strong interactions between the imidazole side chain and the carboxylate functional groups with the nanoparticles. However the adsorption was also reversible and therefore by fitting the batch adsorption data to the Langmuir isotherm the free energy, adsorption equilibrium constant and maximum adsorption was calculated. The experiments were conducted at pH 7.4 in order to simulate physiological conditions. The aggregation experiments showed that unlike citric acid, histidine has no impact on the aggregation.

The conclusions and future directions for this research are given in Chapter 7. Collectively, these studies will contribute towards the growing database on the potential environmental and health implications of nanoscience and nanotechnology. In particular, it is expected that these studies will help answer questions concerning the transformation and fate of manufactured nanomaterials and will also provide an understanding of the unique surface properties and surface chemistry of nanoparticles.

CHAPTER 2

EXPERIMENTAL METHODS

The research presented in this dissertation was conducted using a variety of experimental methods and techniques in order to investigate the aqueous phase behavior of engineered metal based nanoparticles. By using both macroscopic and microscopic scale analyses along with the extensive physicochemical characterization of the materials it is expected that this research will contribute towards developing a conceptual framework for understanding the fate, transport and potential toxicity of nanomaterials. Furthermore, the studies conducted here are envisioned to aid in their safe design. This chapter outlines the general experimental protocols. The specific details of each project is discussed in greater details in the respective chapters as these protocols were tailored to investigate different aspects of the aqueous phase behavior.

2.1 Physicochemical Characterization Techniques

2.1.1 Transmission Electron Microscopy (TEM)

The size and the morphology of engineered metal oxide nanoparticles were determined by JEOL JEM-1230 Transmission Electron Microscope (TEM). Sample preparation for the TEM analysis is as follows. A dilute suspension of nanoparticles in water was sonicated for 30 minutes. A TEM grid was dipped in this suspension and was dried overnight in a desiccator. Once dried the TEM analysis was performed. The TEM grids were carbon coated Cu grids (CF150-Cu) purchased from Electron Microscopy Sciences. The nanoparticle size was given as the average diameter of 100 – 300 particles.

2.1.2 Powder X-ray Diffraction

Bulk crystalline phases of the nanoparticles were examined using powder X-ray Diffraction. Dry powder samples were placed in a 0.2μm well sample holder and pressed with a glass slide to get a smooth surface. A Rigaku Miniflex II Diffractometer with a Co source was used to collect the XRD patterns between angles of 2θ from 25^o – 90^o.

2.1.3 BET Surface Area Measurements

Brauner-Emmett-Teller (BET) analysis using the seven-point N_2-BET adsorption isotherm was performed with a Quantachrome 4200e surface area analyzer to determine the specific surface area (m^2/g) of nanoparticle dry powders. The sample was placed in the calibrated cell and degassed overnight at 100 ^0C prior to the analysis. The physical adsorption of N_2 gas on the nanomaterial surface is quantified using its relative pressures (P/P_0). The slope and the intercept of seven point N_2-BET adsorption isotherm (eq. 2.1), yield the monolayer coverage of the adsorbed N_2 gas.

$$\frac{1}{W[\left(\frac{P_0}{P}\right)-1]}=\frac{1}{W_mC}+\frac{C-1}{W_mC}.\left(\frac{P}{P_0}\right) \qquad (Eq\text{: }2.1)$$

Here W – Weight of the adsorbed N_2 gas, W_m – Weight of the adsorbate constituting a monolayer and C is a constant. The specific surface area was reported as the average of triplicate measurements.

2.1.4 X-ray Photoelectron Spectroscopy (XPS)

X-ray photoelectron spectroscopy is used in probing the nanoparticle surfaces to identify the surface functional groups, surface elemental composition and the corresponding oxidation states. XPS ejects core electrons using X-rays to induce relaxation of higher energy level electron into a lower energy level, simultaneously releasing a photoelectron with a characteristic binding energy (E_B). The kinetic energy (E_k) of the photoelectron is measure which is related to its binding energy according to the Einstein equation,

$$E_B=hv-E_k-\varphi \qquad (Eq\text{: }2.2)$$

where φ is the work function of the spectrometer. The sample preparation consists of pressing the nanoparticle sample on to the indium foil mounted on the XPS stub. Then the sample was placed in the analysis chamber with its pressure maintained at 10^{-9} Torr. The collected data was analyzed using *CasaXPS* data processing software.

2.2 Aqueous Phase Ligand Adsorption Studies

2.2.1 High Performance Liquid Chromatography (HPLC) – Quantitative Batch Adsorption Measurements

Ligand adsorption by nanoparticles was quantified using the Dionex Ultimate 3000 Dionex HPLC system equipped with a UV-visible diode array detector. The sample preparation for batch adsorption studies was conducted according to the following protocol. A fixed solid loading of nanoparticles (2g/L) was suspended in a series of known ligand concentrations in scintillation vials and allowed to mix overnight one and end-over-end circular rotator (Cole-Palmer) to ensure equilibrium adsorption. Then aliquots of these solutions were filtered with 0.2 µm (Xpertec) syringe driven filters, centrifuged and the supernatant was analyzed for the remaining ligand concentration using the HPLC analysis. The amount of ligands adsorbed at the equilibrium was calculated by taking the difference between the initial and final concentrations. The mobile phase and the detector parameters varied according to the ligand of interest and are given in detail in the respective chapters.

2.2.2 Attenuated Total Reflectance Fourier Transform (ATR-FTIR) Spectroscopy – Molecular-based Surface Adsorption

Ligand adsorption at the solid-liquid interface region was studied at the molecular scale using ATR-FTIR spectroscopy. This is based on the phenomenon of total internal reflection of IR radiation at the boundary between two media.[82,126,127] A light beam undergoes total internal reflection when it is propagating in an optically dense medium (n_1) and approaches the optically rare medium (n_2) with an angle of incidence (θ) greater than the critical angle (θ_c). This creates an evanescent field in the optically rare medium with electric field amplitude that decays exponentially with the distance from the surface. The penetration depth (d_p) is defined as the distance required to decreases the electric field amplitude to e^{-1} of its value at the surface which is given by,

$$d_p = \frac{\lambda}{2\pi n_1 n_2 (sin^2\theta - n_{21}^2)^{1/2}} \qquad (Eq: 2.3)$$

where λ is the wavelength and $n_{21} = n_2/n_1$. The magnitude of d_p is 1.46 µm for the AMTIR crystal. Therefore it is an excellent probe to study the interfacial region in the presence of strongly absorbing solvents as water. In a typical ATR-FTIR experiment, a thin film was generated on the AMTIR crystal (Figure 2.1) by making a suspension of nanomaterial and then drop-cast on to the ATR crystal. Then the liquid phase is pumped over the film using the flow cell and changes in the IR spectra was monitored and analyzed. Solution phase spectra were collected in each case for comparison.

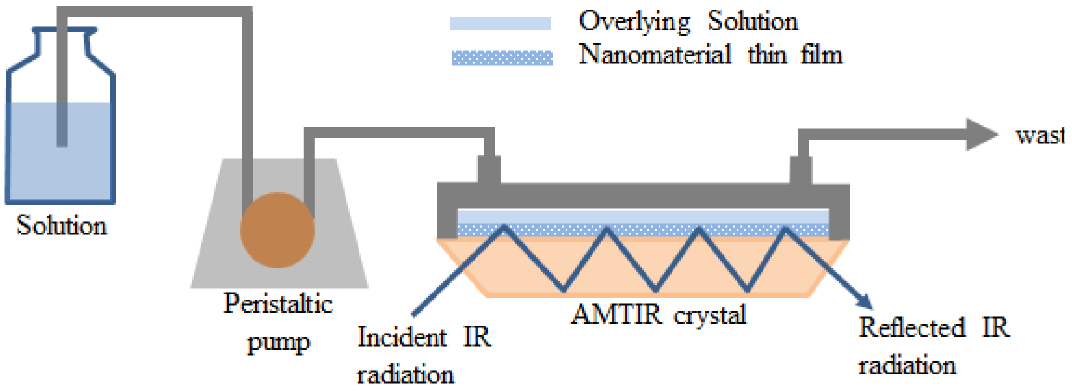

Figure 2.1: Schematic representation of a typical ATR-FTIR experimental setup.

ATR-FTIR spectroscopy also provides quantitative information of the liquid-solid interface. Depending on the size of the ATR crystal the radiation can undergo single or multiple reflections. The absorbance obtained by this technique when multiple reflections occur is not a classical measurement (continuous absorbance of light over a continuous path length) but a summation of discrete reflections.[127] However this difference is reported to be insignificant in the literature and therefore the spectra collected allows calculating the concentration (c) of adsorbed species using the Beer's law given by

$$A = \varepsilon l c = \varepsilon n d_p \qquad (Eq: 2.4)$$

where ε is the molar absorption coefficient and n is the number of internal reflections at the ATR element interface.[126,127]

2.3 Quantitative Nanoparticle Dissolution Studies

The aqueous phase dissolution was quantified using a Varian inductively coupled plasma optical emission spectrophotometer (ICP-OES). Here the nanoparticle suspensions were allowed to mix for 24 hours on the end-over-end Cole Palmer rotator and aqueous phase was filtered and centrifuged. The supernatant was diluted appropriately using 1 M HCl solution and analyzed for the dissolved ions using ICP-OES. Two different methods were employed in the centrifugation steps depending on the extent of aggregation. For particles forming large aggregates (≥ 200 nm) 0.2 μm (Xpertec) syringe driven filters were used and the filtrate was centrifuged for 14,000 rpm for 20 minutes. However, if the aggregate sizes were small (< 200 nm) Amicon Ultra-4 centrifugal filter units (1-2 nm pore size, Millipore) were used and centrifuged at 7500 rpm for 30 minutes. For the ICP-OES analysis five standard solutions with known ion concentrations were used. The supernatant collected after the filtration and centrifugation is imaged using TEM in order to ensure no nanoparticles are getting through the filters.

2.4 Nanoparticle-Nanoparticle Interactions and Aggregation Studies

2.4.1 Sedimentation Profiling using Static Light Scattering

Sedimentation profiles of nanoparticles in the aqueous suspensions yield qualitative information of aggregation. Those of which aggregate heavily sediments at a faster rate than the ones aggregating to a lesser extent. This faster sedimentation results in decreasing scattering intensity as a function of time in contrast to constant scattering intensity for stable suspensions.

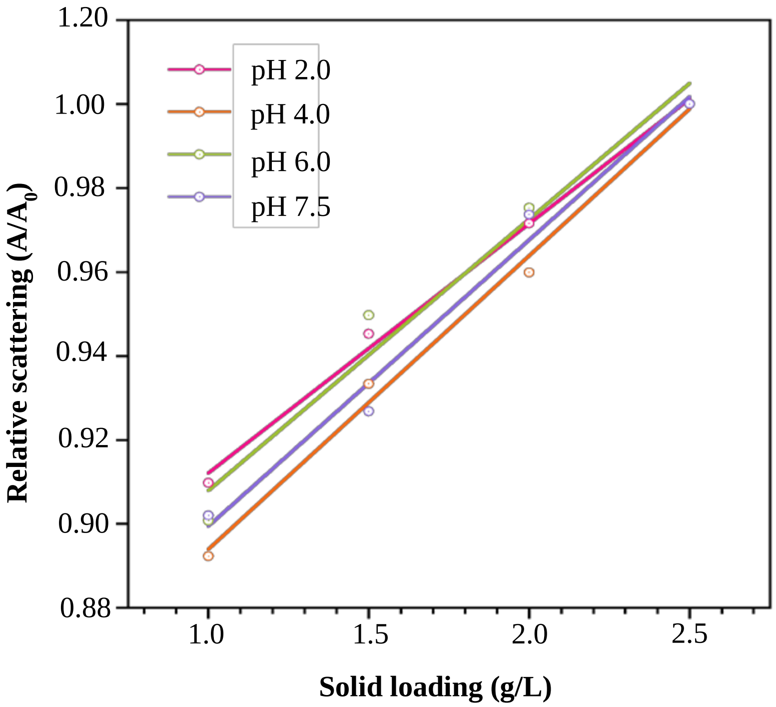

Figure 2.2: Calibration series for TiO_2 sedimentation measured at 508 nm. The suspensions were prepared by mixing TiO_2 nanoparticles in 0.03 M NaCl solutions and then leaving the suspension overnight to achieve the equilibrium aggregate sizes.

Sedimentation profiles are obtained by sonicating nanoparticle suspensions for a fixed period of time, equilibrating for 24 hours to achieve steady state aggregation and measuring the absorbance at 508 nm as a function of time. The absorbance is considered to be proportional to the light scattered by the nanoparticles in the solution. Figure 2.2 illustrates that particle concentration is directly proportional to light scattering at this wavelength. The suspensions were agitated immediately prior to the analysis.

2.4.2 Dynamic Light Scattering (DLS) – Hydrodynamic Diameter

Nanoparticle aggregation in the aqueous medium is quantitatively investigated by dynamic light scattering. The particles in a suspension undergo Brownian motion as a result of the random collisions with the solvent molecules causing diffusion. The diffusion coefficient (D) of a spherical particle size according to the Stokes-Einstein equation,

$$D = \frac{k_B T}{3\pi\eta d} \qquad (Eq: 2.5)$$

where k_B is the Boltzmann constant, η is the viscosity, T is the absolute temperature and d is the hydrodynamic diameter. In the DLS instrument, a laser beam was directed through the nanoparticle suspensions causing scattering as a result of this motion. Thus the intensity fluctuations as function of time is monitored and analyzed using autocorrelation functions. This is illustrated in Figure 2.3. The decay constant of these functions are related to the diffusion coefficient of the particles of the medium which is used to calculate the hydrodynamic diameter from Eq: 2.5. Hydrodynamic diameter gives a more realistic view of the nanoparticle size in the aqueous medium which is always larger than the primary size as a result of aggregation. This is a quantitative size analysis technique complimentary to the sedimentation profiling. The sample preparation for DLS analysis consists of sonicating the nanoparticle suspension and allowing 24 hr to achieve the steady state aggregation. The sample was agitated to re-suspend the particles prior to analysis.

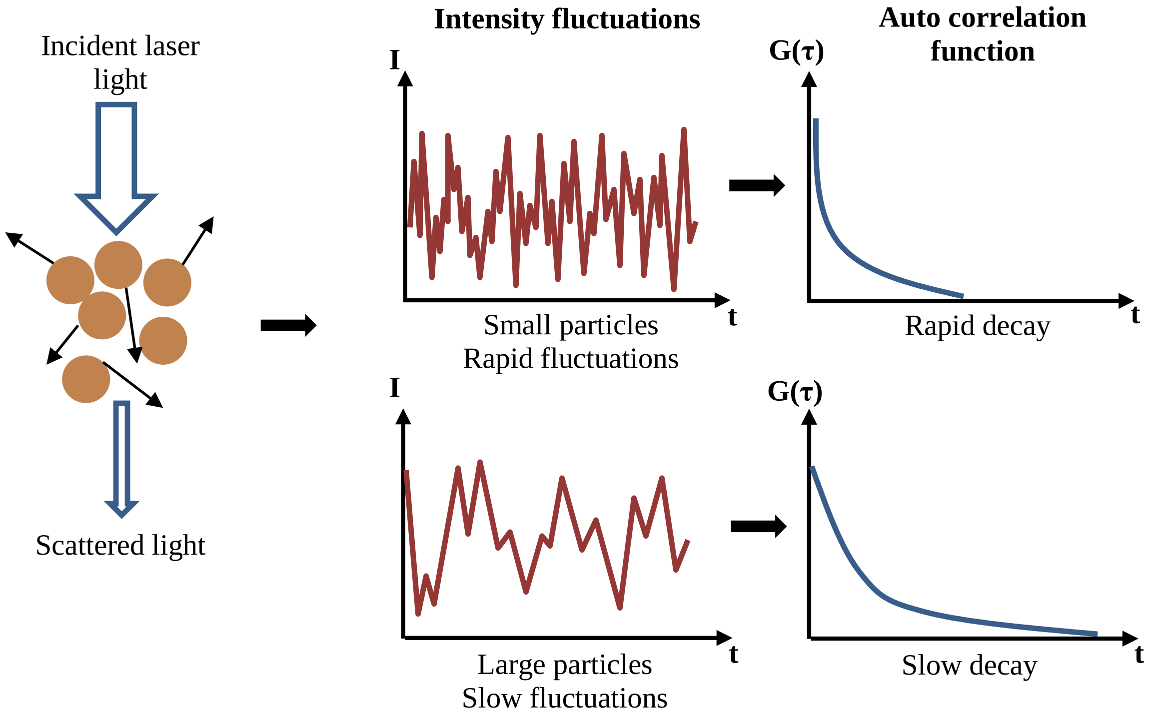

Figure 2.3: Determination of particle size by dynamic light scattering.

2.4.3 Zeta Potential – Surface Charge Measurements

The surface charge of nanoparticles plays a key role in their suspension stability and aggregation behavior. This was measured by the zeta potential mode of the DLS instrument in order to better explain the aggregation patterns of the nanoparticles of interest. Zeta potential is the potential between the particle surface and the “slipping plane” of the “electrical double layer”. Particles suspended in the aqueous medium have charged surfaces (negative or positive). Thus in order to maintain the electric neutrality opposite charged ions in the medium attracts to the surface forming ion clusters and ionized layers. This region is referred to as the “electrical double layer”. The counter ion concentration gradually decreases with the distance from the surface. This double layer is further divided into the Stern layer and the diffuse layer. The ions in the Stern layer are strongly attracted to the surface and the ions in diffuse layer are in motion. When the particles undergo Brownian motion, not only the ions in the Stern layer but also a portion in the diffuse layer moves. The boundary in diffuse layer at which the ions move with the particle is referred to as the “slipping plane” (Figure 2.4).

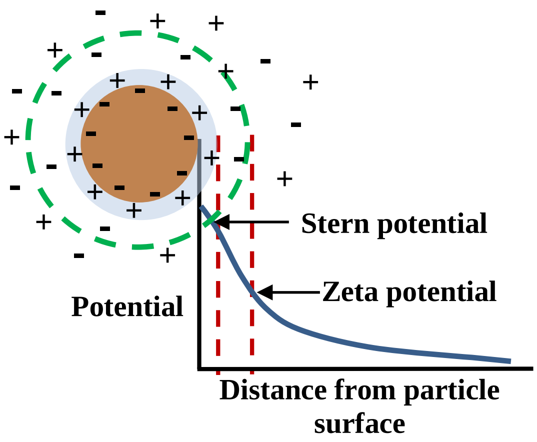

Figure 2.4: Schematic diagram representing the concept of zeta potential.

In the zeta potential mode of the DLS instrument the nanoparticles were placed in an electric field and the velocity of the particles was measure by electrophoretic light scattering. The frequency of the laser light scattered by the particles is different from the incident light and the frequency shift (v_D) is related to the particle mobility (U) by,

$$v_D = \frac{Un}{\lambda} sin\theta \qquad (Eq: 2.6)$$

where λ is the wavelength of the incident light, n is the refractive index of the medium and θ is the scattering angle. Then for aqueous solutions containing electrolytes the zeta potential is calculated from,

$$Z = \frac{\eta}{\varepsilon_0 \varepsilon_r} U \qquad (Eq: 2.7)$$

where ε_0 and ε_r are the dielectric constants in vacuum and of the solvent respectively. The sample preparation for zeta potential measurements consists of sonicating the nanoparticle suspension and allowing 24 hr equilibrate. The sample was agitated to re-suspend the particles prior to analysis.

CHAPTER 3

CITRIC ACID ADSORPTION ON TiO_2 NANOPARTICLES IN AQUEOUS SUSPENSIONS AT ACIDIC AND CIRCUMNEUTRAL pH: SURFACE COVERAGE, SURFACE SPECIATION AND ITS IMPACT ON NANOPARTICLE-NANOPARTICLE INTERACTIONS

3.1 Abstract

Citric acid plays an important role as a stabilizer in several nanomaterial syntheses and is a common organic acid found in nature. Here, the adsorption of citric acid onto TiO_2 anatase nanoparticles with a particle diameter of ca. 4 nm is investigated at circumneutral and acidic pHs. This study focuses on both the details of the surface chemistry of citric acid on TiO_2, including measurements of surface coverage and speciation, and its impact on nanoparticle behavior. Using macroscopic and molecular-based probes, citric acid adsorption and nanoparticle interactions are measured with quantitative solution phase adsorption measurements, attenuated total reflection-FTIR spectroscopy, dynamic light scattering techniques, and zeta-potential measurements as a function of solution pH. The results show that surface coverage is a function of pH and decreases with increasing pH. Surface speciation differs from the bulk solution and is time dependent. After equilibration, the fully deprotonated citrate ion is present on the surface regardless of the highly acidic solution pH indicating pKa values of surface adsorbed species are lower than those in solution. Nanoparticle interactions are also probed through measurements of aggregation and the data show that these interactions are complex and depend on the detailed interplay between bulk solution pH and surface chemistry.

3.2 Introduction

Citric acid is a tricarboxylic acid, with $pK_{a1} = 3.13$, $pK_{a2} = 4.76$, $pK_{a3} = 6.40$, that can form several species (H_3Cit, H_2Cit^-, $HCit^{2-}$, and Cit^{3-}) depending on solution pH (Figure 3.1). In addition to its natural abundance in the environment, citrate ion is often used in nanomaterials synthesis to control both the size and morphology of nanomaterials. Because the citrate ion is a useful capping group that can undergo facile exchange with other functional groups, it is an important surface ligand for the preparation of a wide range of nanomaterials with complex surface functionality that can be used in a number of biomedical and sensor applications.[128-131] Furthermore, Yin *et al.* and Liu *et al.* report selective formation of anatase nanocrystallites from $TiCl_4$ in hydrothermal autoclaving in the presence of organic acids including citric acid.[132,133] These studies show that phase composition and size control are sensitive to the organic acid used due to surface adsorption during crystal growth.

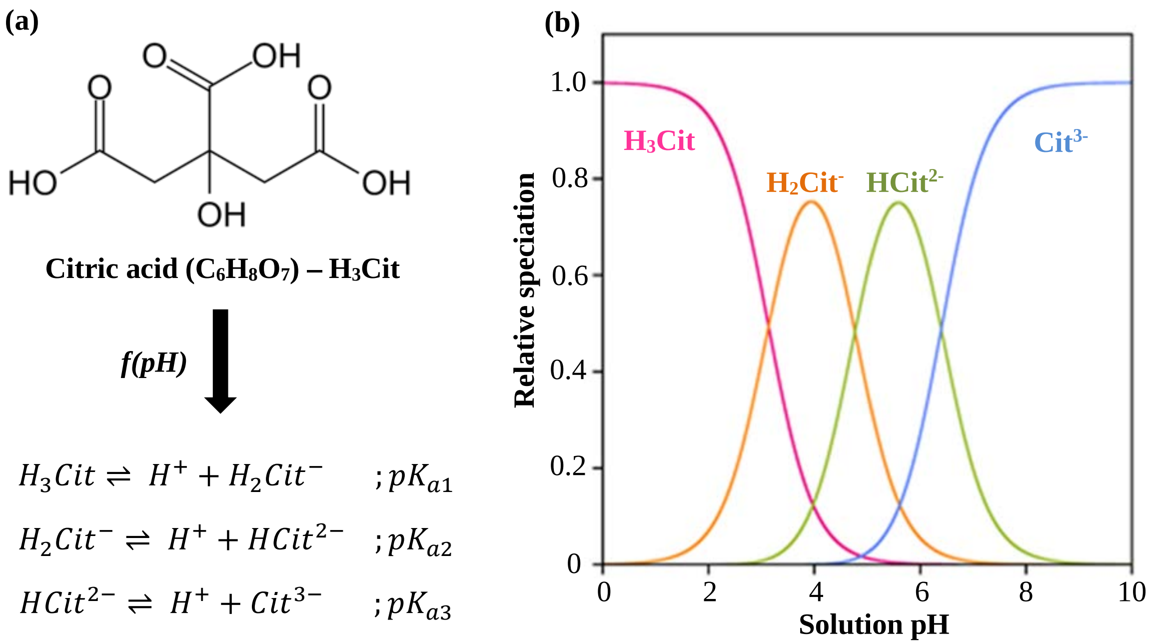

Figure 3.1: Citric acid ($pK_{a1}=3.13$, $pK_{a2}=4.76$, $pK_{a3}=6.40$). (a) Molecular structure and deprotonation (b) Calculated relative speciation of citric acid from pK_a values as a function of pH.

Citric acid is also found in human plasma (0.1 mM) that can result in its interaction with foreign species entering the body.[134] Additionally, the estimated total organic acid concentration in soil solutions has been reported to be in the range of 10-100 µM and can reach as high as 1 mM in the rhizosphere.[135] These organic acids are being heavily studied as a result of their role in mineral dissolution, detoxification of metals as chelating agents, and ultimately determining the fate and transformation of inorganic pollutants.[136-138] Citric acid based studies are also considered to be good analogues for the functional groups in more complex humic acids that can provide insight into adsorption mechanisms.

The focus of this study is on surface adsorption and surface chemistry of citric acid on ca. 4 nm TiO_2 (anatase) at circumneutral and acidic pH as nanoparticle surfaces play a key role in their behavior. Although our particular interests are related to the chemistry of nanomaterials in the environment, the results of this study can be more broadly applied to understanding the detailed surface chemistry of this important ligand. In particular, the adsorption of citric acid has been studied here with emphasis on pH effects using quantitative solution phase adsorption measurements to determine surface coverage and ATR-FTIR spectroscopy to probe surface speciation. Additionally, nanoparticle-nanoparticle interactions and the stability of nanoparticle suspensions with and without citric acid have been followed with light scattering techniques as a function of pH. Although few studies integrate these different types of measurements to provide a quantitative description of surface coverage, surface speciation, and nanoparticle interactions, there is the potential to gain additional insights into the adsorption of citrate on nanoparticle surfaces by integrating these experimental results. Thus, the current study provides important insights into the use of citrate as a capping agent and stabilizer of nanoparticles in aqueous suspensions. It also provides much needed experimental data on the interactions of nanomaterials with common ligands found in the environment.

3.3 Experimental Methods

3.3.1 Nanoparticle Characterization

Powder X-ray diffraction (XRD) was used to determine the bulk crystalline phase of TiO_2 nanoparticles. Diffraction patterns were collected using a Rigaku Miniflex II diffractometer with a Co source. The specific surface area of the particles was determined from seven-point N_2-BET adsorption isotherm measurements using a Quantachrome 4200e surface area analyzer. Samples were degassed for 3 h at 573 K prior to the analysis.

3.3.2 Quantitative Solution Phase Adsorption/Desorption Studies.

Adsorption and desorption studies were conducted at pH 2.0, 4.0, 6.0, and 7.5. Stock solutions of 100 mM citric acid were prepared at pH 2.0, 4.0, 6.0, and 7.5 at 293 K. Solutions at pH 2.0 and 4.0 contained 0.01 and 0.0001 N HCl solutions, while solutions at pH 6.0 and 7.5 contained 25 mM of MES and HEPES, respectively. pH adjustment at higher pHs was done by NaOH solution (8 M). As a result of the ionic strength of pH 2.0 solution and pH adjustments, all the solutions were prepared to have an ionic strength of 0.03 M NaCl. The adsorption experiments were conducted according to the following protocol.

From the solutions prepared above, 6 mL aliquots were added into 7 mL glass vials. To each of these vials, appropriate volumes of citric acid (100 mM) were added to obtain a concentration range of 0.1-5 mM in the reactors. Prior to the addition of the solid, 1 mL of sample was drawn out from each vial for the quantification of the initial citric acid concentration. A TiO_2 solid loading of 2.0 g/L in the reactors was used. After mixing, the reactors were crimp sealed, covered in aluminum foil to inhibit any photo-induced chemistry, and mixed on a Cole-Parmer circular rotator for 24 h. After completion of the mixing, suspension pH was measured. Then, from each reactor two aliquots (~1 mL each) were drawn out with a disposable syringe, passed through a 0.2 µm syringe-driven filter (Xpertec) into separate centrifugation vials, and centrifuged at 14000 rpm for 20 min to separate the solution from the TiO_2 nanoparticles.

One set of these samples was analyzed using an Agilent HPLC equipped with a diode array UV-vis detector at 226 nm using 0.01N H_2SO_4 as the mobile phase. The instrument response was measured with respect to known standards of citric acid and converted into aqueous phase concentrations. The standards were prepared fresh for each set of reactors. The concentration of the adsorbed citric acid was then determined using the difference of the initial and final citric acid concentrations in the aqueous phase.

Experiments were conducted to investigate the reversibility of citric acid adsorption onto TiO_2 nanoparticles. For an adsorption study conducted with 3 mM of citric acid, the suspension was divided into five 1 mL aliquots and centrifuged for 20 min. The supernatant was decanted off and the remaining particles were re-suspended in fresh solutions of the same initial pH and transferred to a 7 mL glass vial, and the same procedure as in the adsorption study carried out to obtain the amount of citric acid in the solution.

3.3.3 Quantitative Solution Phase Nanoparticle Dissolution Studies.

A second set of the samples discussed above for quantitative adsorption measurements were analyzed using a Varian Inductively Coupled Plasma Optical Emission Spectrophotometer (ICP-OES) for any dissolved titanium. These centrifuged samples were diluted to 5 mL with 1 M HCl solutions prior to analysis.

3.3.4 ATR-FTIR Spectroscopy for Molecular Level Adsorption Studies.

Solution phase attenuated total reflectance Fourier transform infrared (ATR-FTIR) spectroscopy measurements were recorded of 100 mM citric acid solutions prepared at several different pH values (pH 2.0, 4.0, 6.0, and 7.5) using a Thermo-Nicolet FTIR Spectrometer equipped with a MCT/A detector. Additionally, citric acid adsorption onto TiO_2 surface was also probed with ATR-FTIR spectroscopy. For surface adsorption studies, a thin, evenly coated TiO_2 film was deposited onto an AMTIR crystal element in a horizontal ATR cell (Pike Technologies, Inc.). The film was prepared by placing a suspension of TiO_2 (1.5 mg in 1 mL of Optima water) onto the crystal and drying overnight. The deposited film was slowly flushed with a stream of water to eliminate any loosely bound particles. Citric acid solutions (0.1, 0.2, 0.5, 1, 2, 5, and 10 mM) of constant ionic strength were prepared and then introduced into the horizontal cell. Initially, spectra were collected after 5 min. Additional experiments were conducted at pH 2.0 and pH 6.0 for longer periods of time to equilibrate the solution. Spectra were collected in the spectral range extending from 500 to 4000 cm^{-1} at an instrument resolution of 4 cm^{-1}.

3.3.5 Nanoparticle-Nanoparticle Interactions and Aggregation Measurements

Nanoparticle-nanoparticle interactions and the aggregation behavior of 4 nm TiO_2 particle suspensions at 0.03-0.04 M ionic strength were examined at pH 2.0, 4.0, 6.0, and 7.5. Sedimentation experiments were conducted with a UV-vis spectrometer by monitoring the changes in the light scattering when passed through TiO_2 suspensions (2.0 g/L) as a function of time. Suspensions were prepared in a 1 cm path length cuvette, agitated, and placed in the UV-vis instrument and the amount of transmitted light (λ = 508 nm) was measured over time. The solutions were left overnight to reach the steady state aggregation, and therefore, no aggregation was assumed to occur during the time of the measurement. Therefore, the sedimentation is solely attributed to the gravitational settling depending on the particle size. A linear relationship between the scattered light and the TiO_2 suspension concentrations was observed for particle suspension concentrations of 0.5-2.0 g/L at 508 nm (Figure 2.2).

A commercial dynamic light scattering (DLS) instrument (Malvern Zetasizer Nano ZS) equipped with a green laser at 532 nm was used to obtain the size distribution of aggregates in the absence and the presence of citric acid. For DLS measurements, suspensions were prepared at 0.01 g/L solid loading of TiO_2 in appropriate pH solutions. The pH solutions were passed through a 0.2 µm syringe driven filter to minimize the influence of unwanted dust particles. Samples were allowed to sit overnight to ensure the aggregation had reached its steady state. Aggregate sizes were studied over a range of citric acid concentrations (0-0.2 mM).

In addition, the surface charge of the nanoparticles was measured using the zeta potential mode of the Malvern Zetasizer Nano ZS. All suspensions were prepared to have a solid loading of 0.05 g/L, 0.1 mM of citric acid, and a fixed ionic strength of 0.03 M. The suspensions were allowed to equilibrate for 24 h after mixing. Measurements were made at pH 2.0, 3.0, 4.0, 5.0, 6.0, and 7.0. These experiments were also conducted in the absence of citric acid.

3.4 Results and Discussions

3.4.1 Nanoparticle Characterization.

XRD analysis confirmed that the TiO_2 nanoparticles consist entirely of anatase. The measured surface area using a seven-point BET analysis showed an average value of 219±3 m^2/g from four replicate measurements. A previous TEM characterization of these 5 nm particles has shown a size distribution between 2 and 5 nm with an average nanoparticle diameter of 3.5±1.5 nm.[139] These nanoparticles are referred to as 4 nm particles herein.

3.4.2 Citric Acid Adsorption on TiO_2 Nanoparticles at T=293K: Surface Coverage as f(pH).

Citric acid adsorption on 4 nm TiO_2 nanoparticles was carried out at pH 2.0, 4.0, 6.0, and 7.5. For 2 g/L of TiO_2 nanoparticles, the initial and the final pH of the reactors were the same for pH 2.0, 6.0, and 7.5, while the reactors with initial pH 4.0 was raised to values ranging from pH 4.5 to 5.5. The general trend of citric acid adsorption onto the TiO_2 nanoparticles is a decrease with increasing solution pH. The surface area normalized uptake of citric acid at saturation coverage is given in Table 3.1 and goes from $9.7\pm0.4 \times10^{13}$ to $3.1\pm0.4 \times10^{13}$ molecules cm^{-2} at the lowest and highest pH values of 2.0 and 7.5, respectively. Saturation coverage was determined to occur at concentrations greater than 2 mM (Figure 3.2) and these values represent the average of four different independent measurements of solution phase concentrations between 2 and 5 mM.

Table 3.1: Quantitative measurements of saturation surface coverage for citric acid on TiO_2 nanoparticles in solution at pH 2.0, 4.0, 6.0 and 7.5.

pH	Surface coverage (molecules cm^{-2})
2.0	$9.7 \pm 0.4 \times 10^{13}$
4.0	$7.5 \pm 0.3 \times 10^{13}$
6.0	$6.3 \pm 0.5 \times 10^{13}$
7.5	$3.1 \pm 0.4 \times 10^{13}$

The decrease in surface coverage by over a factor of 3 is not unexpected since the surface charge of TiO_2 nanoparticles and the citric acid species increase in negativity simultaneously with the increasing pH. Zeta potential measurements showed a zero point charge pH (pH_{zpc}) of TiO_2 nanoparticles to be pH 4.2 in the absence of citric acid. This value is close to the pH_{zpc} (pH 4.6-6.5 for sizes between 3.6 and 8.1 nm) reported in the literature for TiO_2 nanoparticles of this size. Therefore, the surface charge of these particles is mostly positive for pH<4.0 and negative for pH>4.0.[114]

As shown in Figure 3.1, the major fraction of citrate species in the solution is neutral/monoanionic, mono/ dianionic, and trianionic in these three pH ranges of <4.0, between 4.0 and 6.0, and >6.0, respectively. As the solution pH increases, the repulsive forces between the nanoparticles and the negatively charged anions increase resulting in the observed decrease in the uptake.

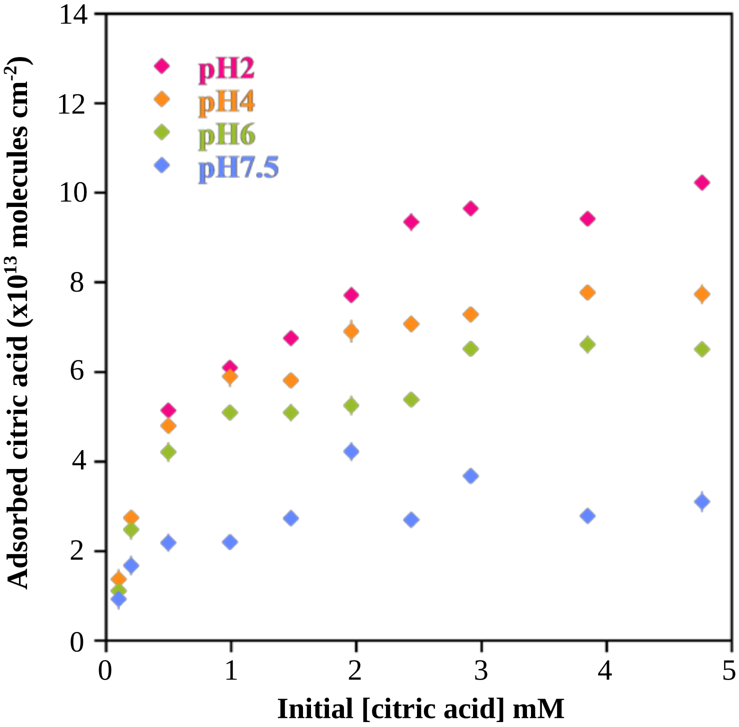

Figure 3.2: Isotherms for the adsorption of citric acid on TiO_2 nanoparticles at 293 K and pH 2.0, 4.0, 6.0 and 7.5. A plateau is seen above citric acid concentrations of 2 mM indicating saturation coverage. The saturation coverage, i.e. the maximum number of adsorbed molecules cm^{-2} is determined using the specific surface area as determined by BET analysis.

This observed trend is in good agreement with previous studies on citric acid adsorption by goethite.[137,138] However, the degree of drop in citric acid uptake is smaller for the nanoscale TiO_2 particles compared to that of goethite in these studies with the 3-fold decrease when going from pH 5.5 to pH 8.0 for goethite in contrast to the 3-fold decrease from pH 2.0 to pH 7.5 for TiO_2 nanoparticles.

Reversibility measurements showed that the adsorption of citric acid at all pH values was irreversible. Furthermore, the ATR-FTIR experiments showed no decrease in the peak intensities when the citrate adsorbed TiO_2 surface was washed with water which confirmed the results of the reversibility studies. Studies of citric acid adsorption onto iron and aluminum oxides have shown inner-sphere complexes forming on the surface in the pH range considered.[137,138,140] Since inner-sphere surface complexation typically represents a more strongly coordinated surface species that can be irreversible at 293 K, it can be proposed that citric acid adsorption on TiO_2 nanoparticles is mostly likely inner sphere in nature (*vide infra*).

3.4.3 Citric Acid Adsorption on TiO_2 Nanoparticles at T=293K: Nanoparticle Dissolution as a f(pH) with and without the Presence of Citric Acid.

Although from thermodynamics, bulk TiO_2 is known to be insoluble in aqueous media at 298 K, experimental observations have been made to suggest that for very small nanoparticles dissolution can occur given that solubility, due to size dependent surface free energies, is size dependent. Schmidt and Vogelsberger report that TiO_2 precipitated by the hydrolysis of titanium tetraisopropoxide shows saturation dissolution at micromoles per liter and that particle size, morphology, pH, and temperature were shown to affect dissolution behavior.[107] Because the current study is focused on 4 nm TiO_2, measurements were done to determine if dissolution can occur for these nanoscale materials. Since citrate is potentially a polydentate adsorbate, it can form a strongly coordinating complex on the surface which can result in oxide dissolution associated with the simultaneous detachment of two metal cations from the surface.[140,141] However, ICP-OES studies showed no dissolution of TiO_2 nanoparticles taking place in the presence of citric acid under all pH conditions investigated.

3.4.4 Citric Acid Adsorption on TiO_2 Nanoparticles at T=293 K: Solution Phase Speciation Compared to Surface Speciation as f(pH).

In solution, citric acid is fully protonated at pH 2.0, partially deprotonated at pH 4.0 and 6.0, and it is fully deprotonated at pH 7.5 (Figure 3.1b). As shown in Figure 3.3, the fully deprotonated citrate ion has prominent absorption bands near 1570 and 1391 cm^{-1} and a weak band around 1280 cm^{-1}. The two prominent bands, 1570 and 1391 cm^{-1}, are assigned to the asymmetric and symmetric stretching motions of the carboxylate group, respectively.[136-138,140,142-145]

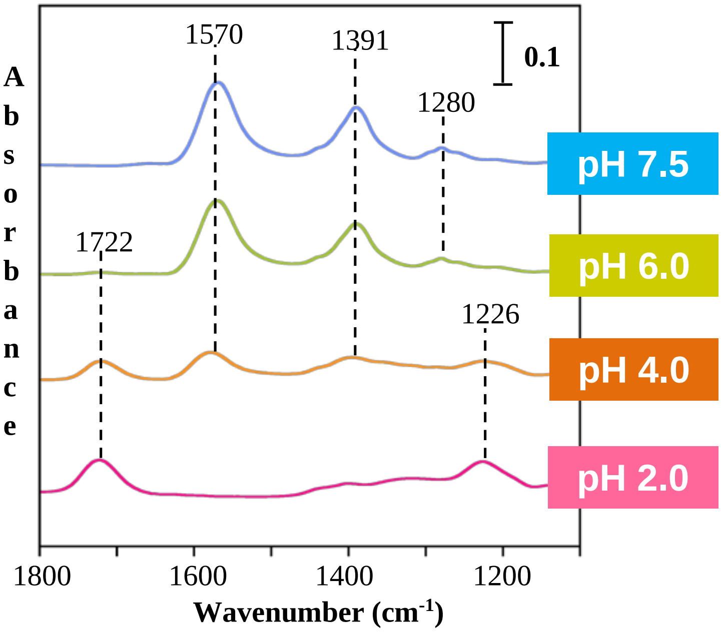

Figure 3.3: ATR-FTIR spectra of 100 mM citric acid solutions at different solution pH.

The weaker band at 1280 cm^{-1} is assigned to coupled stretches and bends of the carboxylate group. With decreasing pH, the bands at 1570 and 1391 cm^{-1} diminish in intensity and at pH 2.0 are no longer present. Instead, absorption bands at 1722 and 1226 cm^{-1} are evident. These new bands correspond to the C=O stretching motion and coupled C-(OH) stretching and C-O-H bending motions, respectively.[9-11, 14, 17-20] ATR-FTIR solution phase spectra agree well with the calculated speciation fractions shown in Figure 3.1b.

Spectroscopic measurements as a f(pH) gave useful information about the citrate-surface adsorbed complex. ATR-FTIR spectra of adsorbed citric acid onto TiO_2 nanoparticles as a function of citric acid concentrations (ranging from 0.1 to 10 mM) and pH are shown in Figure 3.4. These spectra were recorded 5 min after introduction of the solution phase. A comparison of ATR-FTIR spectra recorded of 10 mM solution phase citric acid at all four pHs investigated to the spectra recorded in the presence of TiO_2 (given by the dotted line) shows that there is no contribution of solution phase absorbance to the adsorbed spectra shown in Figure 3.4.

These ATR-FTIR spectra shown in Figure 3.4 provide information on surface speciation and indicate differences from speciation in solution. The most prominent difference between the solution spectra (Figure 3.3) and surface adsorbed spectra (Figure 3.4) is observed at pH 2.0. The bands at 1570 and 1391 cm^{-1} which are not present in the pH 2.0 solution phase are present for adsorbed citric acid at pH 2.0. Furthermore, the band at 1722 cm^{-1} observed clearly in the solution phase spectrum and in fact the most intense band in the spectrum is seen to shift to 1717 cm^{-1} and is no longer the most intense band in the spectrum. The shift toward a lower value arises most likely as a result of the weakened C=O bond resulting from the interaction with the surface.

For other pH values, the spectra appear more similar between the solution phase and on the surface. However, upon closer inspection, it can be seen that the absorption bands for the surface adsorbed species are broad compared to solution phase. Furthermore, a shoulder peak at 1436 cm^{-1} can be observed in all the spectra.

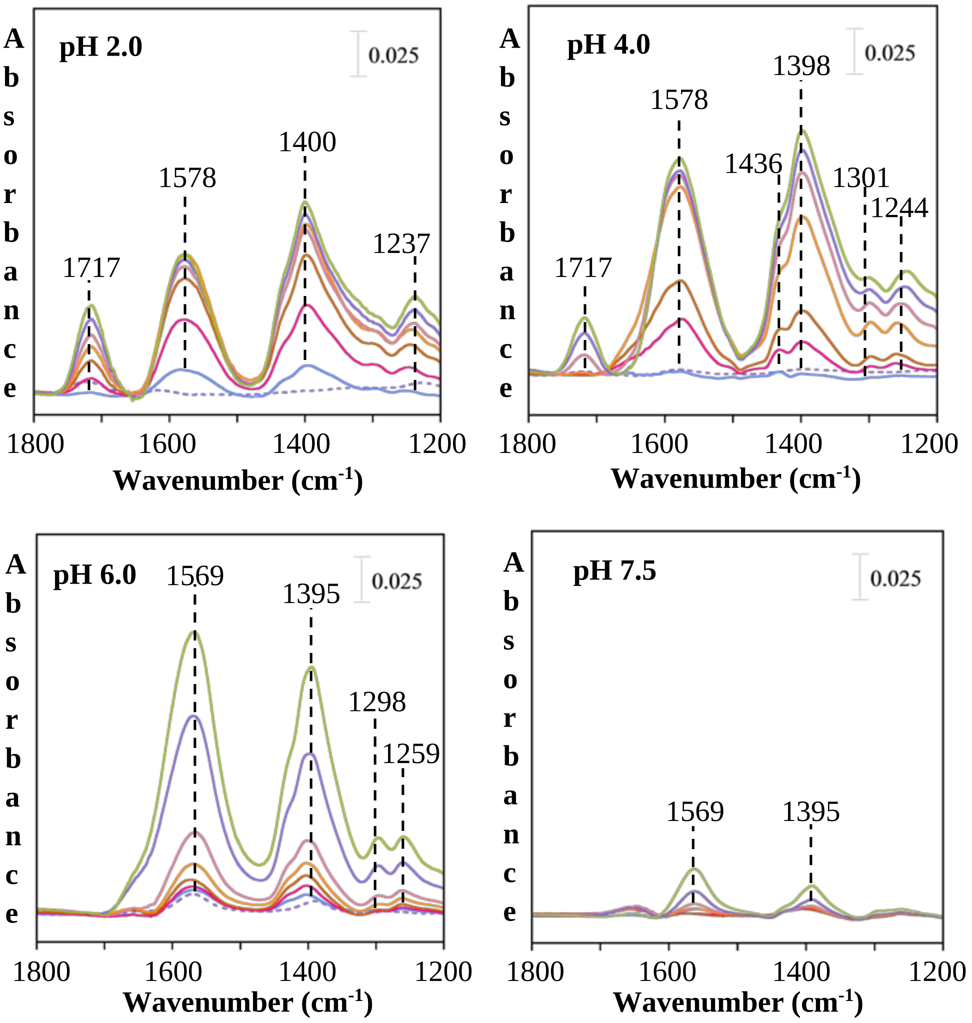

Figure 3.4: ATR-FTIR spectra of adsorbed citric acid as a function of initial concentration (0.1, 0.2, 0.5, 1.0, 2.0, 5.0 and 10 mM) at different pH: 2.0, 4.0, 6.0 and 7.5. (Solid line – adsorbed phase, dotted line – 10 mM CA in solution phase)

In the literature (Table 3.2) for the solution phase spectra, the shoulder at 1436 cm^{-1} is given as -CH$_2$ – bending mode.[146] However, by inspecting Figure 3.4 which gives the surface adsorbed citric acid spectra at pH 4.0, it can clearly be seen that there is a distinct band appearing at 1436 cm^{-1}. This band, as it grows, overlaps with the absorption at 1398

Table 3.2: Vibrational frequencies (cm^{-1}) and assignments of the solution phase and initially observed (t=5 min) adsorbed citric acid species on TiO_2 Nanoparticles at pH 2.0, 4.0, 6.0 and 7.5. (Refs: 9-11, 14, 17-20)

Mode of vibration	**pH 2.0**		**pH 4.0**		**pH 6.0**		**pH 7.5**	
	solution	surface	solution	surface	solution	surface	solution	surface
$\nu(C=O)$	1722	1717	1720	1717	1721	-	-	-
$\nu_{as}(COO^-)$	-	1579	1570	1578	1570	1569	1570	1569
$\nu_s(COO^-)$	-	1400	1391	1398	1391	1395	1391	1395
		1436*		1436*		1436*		1436*
$\nu(C-OH)$					1094		1094	
$\nu(OC-OH)+\delta(OC-OH)$	1226		1226		-		-	
$\delta(CH_2)$	1436		1436		1436		1436	
$\delta(O=C-O^-)$					1280	1298	1280	1298
						1259		1259

cm^{-1}. These changes in spectral features suggest that the absorption bands in the surface spectra are a sum of several overlapping peaks. These observations support the proposed mode of citrate adsorption as an inner sphere complex, that is, inner sphere adsorptions are known to result in broader spectra and a higher splitting of several of the absorption bands.[136]

ATR-FTIR spectroscopy also reveals that the surface spectra are time dependent. Figure 3 shows this explicitly for pH 2.0.

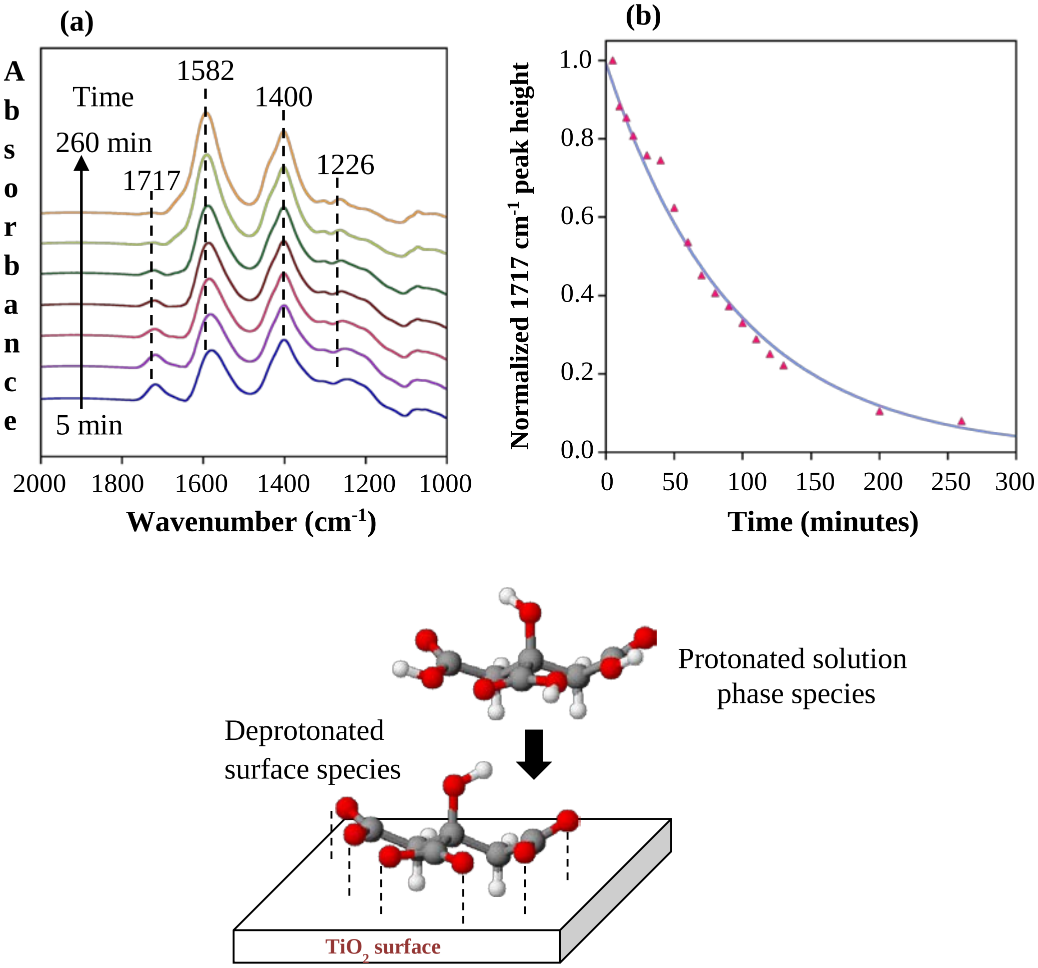

Figure 3.5: Molecular level analysis (a) ATR-FTIR spectra as a function of time show changes in surface speciation following adsorption of 10 mM citric acid at pH 2.0. (b) A plot of the normalized intensity of the ν_s(C=O) at 1717 cm^{-1} as a function of time. (c) Cartoon representation of surface adsorption of citric acid from solution at pH 2.0.

In these experiments, spectra were recorded as a function of time for up to 4 h. It can be seen from the spectra shown in Figure 3.5a that after 4 h the band at 1717 cm^{-1} has disappeared from the spectrum and is no longer present. The intensity of this peak plotted as a function of time (Figure 3.5b) clearly demonstrates this. These data show that, at pH 2.0, the adsorbed species undergo deprotonation on the surface and yields the fully deprotonated citrate ion on the TiO_2 nanoparticle surface (Figure 3.5c). These results suggest that there is an increase in the acidity of citric acid when adsorbed on the surface. In other words, the ability to deprotonate and the apparent pKa's of citric acid have decreased upon surface complexation and are below 2. However, it should be noted that at pH 4.0 and at a concentration of 10 mM similar ATR-FTIR data show that the C=O stretch peak does not decrease with time arising possibly due to differences in the mode of adsorption at different pH values, suggesting that the details of the nature of adsorption sites and coordination mode play a role in surface speciation.

It has been proposed that citrate adsorption on goethite results in the formation of inner-sphere complex with citrate coordination to the surface via at least one carboxylate group.[136] The spectra observed in the goethite study are similar to the spectra collected in this current study. With the observed deprotonation taking place on the surface, it can be proposed that the initial adsorption is via the carbonyl oxygen (C=O), which result in the increased polarization of the C-O-H bonds leading to rapid loss of H^+ (Figure 3.5c). At pH 2.0, all the carboxylic groups of the molecule appears to be bound to the surface as seen by the complete loss of the protonated C=O peak in the spectra collected as a function of time. But at pH 6.0, whether all the carboxylate groups are bound to the surface is less clear as deprotonation does not necessarily indicate surface coordination. However the increased breadths of the peaks are indicative of surface coordination as discussed above.

3.4.5 Light Scattering and Zeta-Potential Measurements of TiO_2 Nanoparticle Suspensions as a f(pH) with and without the Presence of Citric Acid To Investigate Nanoparticle-Nanoparticle Interactions and Aggregation.

The stability of the nanoparticle suspensions was investigated under the same conditions that the quantitative surface adsorption measurements were made. Sedimentation plots as a function of time are shown in Figure 3.6a. These data show that nanoparticles settle out of solution as a function of time for nanoparticle concentrations of 2.0 g/L at pH 4.0, 6.0, and 7.5. Only at pH 2.0 are nanoparticle suspensions stable. Furthermore, the nanoparticle suspensions at pH 2.0 were visually stable for several days. This stabilization of TiO_2 particle suspensions has been previously observed at highly acidic and basic conditions.[147] Complementary DLS measurements gave the largest size distribution of aggregates at pH 6.0 and the smallest at pH 2.0 (Figure 3.6b).

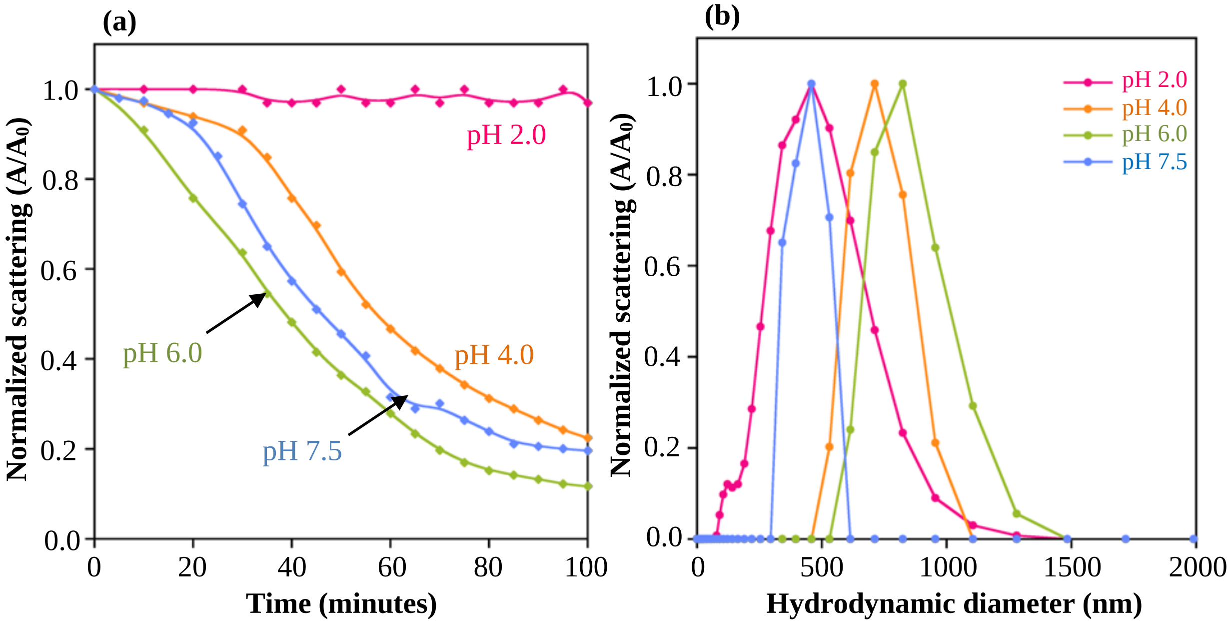

Figure 3.6: Aggregation Measurements (a) Sedimentation plots from UV-vis and (b) Hydrodynamic diameter from DLS measurements for TiO_2 NPs in the absence of citric acid at different pH: 2.0, 4.0, 6.0 and 7.5.

According to Derjaguin, Landau, Verwey, and Overbeek theory (DLVO theory), the stability of a colloidal system is determined by the sum of van der Waals attractive forces and electrical double layer forces that exist between particles as they approach one another due to Brownian motion.[140,141] At pH 2.0, TiO_2 nanoparticles experience higher repulsive forces due to high surface protonation, hence, increased double layer formation. At pH 6.0 (which is in the range of pH_{zpc} for 4 nm TiO_2 nanoparticles), the surface charge is almost neutral and the double layer formation is almost zero. Therefore, the attractive van der Waals forces as the pH increases begin to dominate resulting in increased aggregation.[147]

The aggregation behavior of the TiO_2 and nanoparticle-nanoparticle interactions alters in the presence of citric acid in highly acidic and circumneutral conditions. Sedimentation plots for pH 2.0 and pH 6.0 show that the presence of citric acid reverses the behavior seen in Figure 3.7.

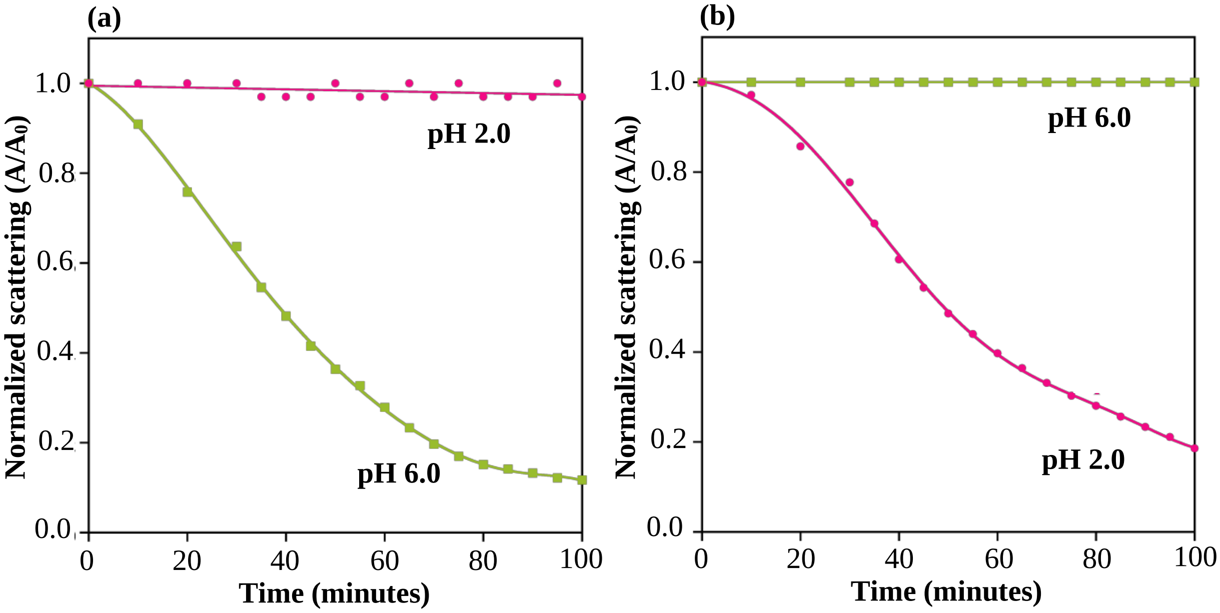

Figure 3.7: Static light scattering studies (a) Sedimentation of TiO_2 NPs in the absence of citric acid compared to (b) sedimentation of TiO_2 NPs in the presence of citric acid (3 mM) at pH 2.0 and pH 6.0.

It is seen that citric acid causes a destabilization of solutions at pH 2.0 and significantly enhances the aggregation, whereas for pH 6.0, citric acid stabilizes nanoparticle suspensions. DLS measurements of nanoparticle suspensions at pH 2.0 and 6.0 as a function of increasing citric acid adsorption shown in Figure 3.8 complement the sedimentation data presented in Figure 3.7. The DLS data collected at nanoparticle suspensions of 0.01 g/L clearly show that at pH 2.0 aggregate size increases with increasing concentration, whereas at pH 6.0, aggregate size decreases with increasing concentration of citric acid.

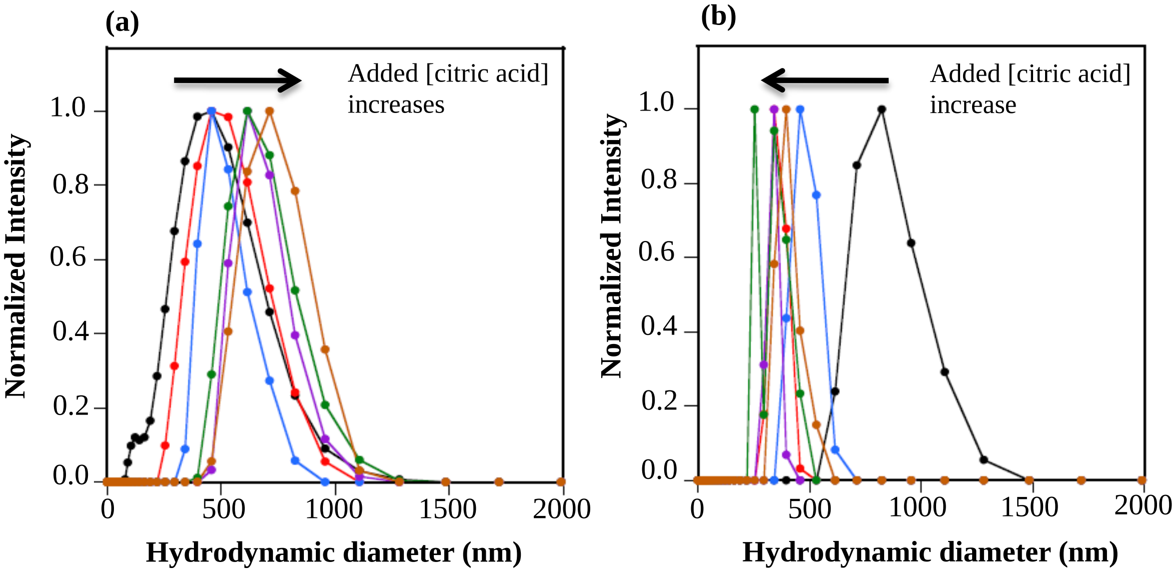

Figure 3.8: Intensity normalized aggregate distribution at (a) pH 2.0 (b) pH 6.0. The DLS experiments were conducted as a function of increasing citric acid concentrations with a suspension of 0.01 g/ L TiO_2 NPs.

Taking the adsorbed speciation and the mode of adsorption suggested by the spectroscopic data, the reversal of the suspension stabilities can be attributed to the surface charge modification by the adsorbed citrate.[84,140,141]Adsorbed citrate is a trianion (Figure 3.5c) and TiO_2 surface is positively charged at pH 2.0. The adsorption of the citrate neutralizes the surface charge to a greater extent and thereby reduces the double layer formation leading to the observed enhanced aggregation at pH 2.0. At pH 6.0, the adsorbed citrate could have created a negative charge on the neutral surface leading to a double layer formation thereby increasing the repulsive forces (charge stabilization).

Zeta potential measurements support the data shown in Figures 3.7 and 3.8. In general, zeta potentials measure the net charge at the diffuse boundary of a particle. It is generally assumed that zeta potentials close to zero result in unstable suspension and nanoparticle aggregation. Figure 3.9a shows differences in the zeta potential for TiO_2 in the presence and absence of citric acid. These data show that at pH 2.0 citric acid shifts the zeta potential for TiO_2 nanoparticle suspensions toward zero (from +60 to +19 mV) and thus decreases the nanoparticle suspension stability as confirmed by the sedimentation plots and DLS aggregate size measurements. However, at pH 6.0, citric acid shifts the zeta potential measurement for TiO_2 nanoparticle suspensions further away from zero (from -33 to -45 mV). Thus, it is clear that the presence of citric acid affects the surface charge under pH conditions and the direction of change supports the molecular measurements that show surface charge alterations upon adsorption; That is, the deprotonated citric acid on the surface lowers the net surface charge toward zero at acidic pH conditions and increases the net negative charge at circumneutral pH conditions. The shift in the surface charge (although not very large) seems to be enough to overcome the activation barrier for aggregation at pH 2.0 while increase the energy barrier for aggregation at pH 6.0. These observations and hypotheses are supported using DLVO theory along with measured zeta potential values at the different pH conditions. According to DLVO, nanoparticle-nanoparticle interactions are determined by the potential energy between two nanoparticles which is a sum of the attractive and repulsive interactions,

$$V_{tot} = V_{att} + V_{rep} \qquad (Eq\colon 3.1)$$

due to van der Waals and electrostatic interactions, respectively. Attractive forces are a function of particle size and the Hamaker constant which accounts for inter-particle interactions. Repulsive forces are due to surface charge and electrostatic interactions as measured by the zeta potential.

(a) Surface charge measurements

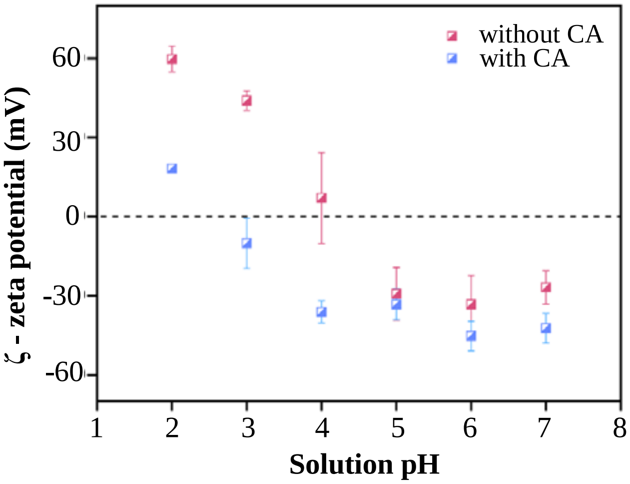

(b) DLVO theory calculation

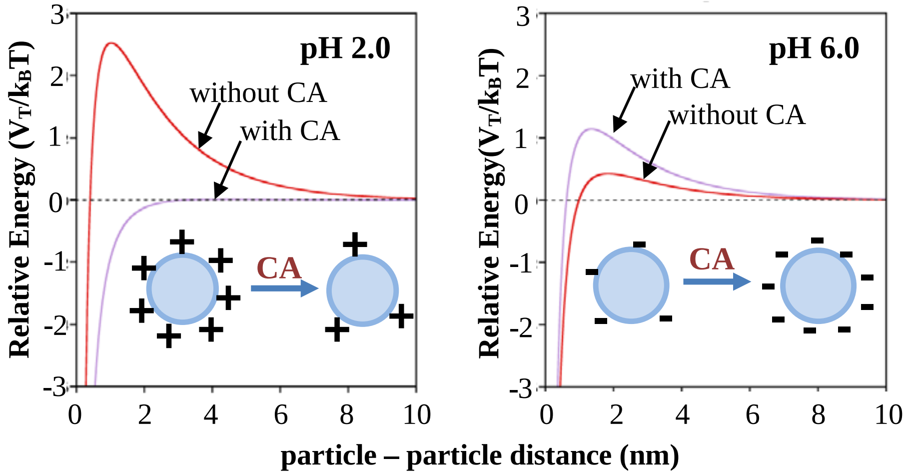

Figure 3.9: Impact of the surface charge (a) Zeta potential measurements of TiO_2 (0.05 g/L) in the absence of and the presence of citric acid (0.1 mM) as a function of pH. (b) DLVO theory calculations for TiO_2 NPs in the absence and presence of citric acid at pH 2.0 and pH 6.0. A cartoon representation of the surface charge alteration with the addition of citric acid is also shown.

According to these calculations, nanoparticle suspensions at pH 2.0 in the absence of citric acid are the most stable with the highest nanoparticle-nanoparticle repulsive barrier of nearly 3 k_BT, whereas in the presence of citric acid, pH 6.0 suspensions are most stable and show the highest nanoparticle-nanoparticle repulsive barrier of 1.5 k_BT (Figure 3.9b).

Similar studies done on TiO_2 nanoparticles in the presence of oxalic acid and Suwannee River Fulvic Acid (SRFA) have shown different trends in aggregation.[84,148] According to Pettibone *et al.*, the presence of oxalic acid at pH 2.0 has shown a similar enhanced aggregation but the aggregation at pH 6.5 had remained unaffected.[148] Analysis of the surface charge in the presence of oxalic acid showed that at pH 2.0 the surface charge is shifted from +25 to +4 mV which is a much similar to the case of citric acid. However, at pH 6.0, the surface charge has shifted from -33 to -23 mV with oxalic acid and the sedimentation behavior remained unaffected. The difference in the aggregation behavior at pH 6.0 for oxalic and citric acid could be a result of increased electrostatic and steric repulsions present in the citric acid-TiO_2 compared to oxalic acid-TiO_2. DLVO theory suggests that the repulsive forces form an energy barrier for the particle aggregation. Only the particles that collide with sufficient energy to overcome this barrier will form aggregates. These repulsive forces can be steric and/or electrostatic. A study by Domingos *et al*. has shown decreased aggregation in the presence of SRFA from highly acidic medium up to pH 6.0 after which there is an increase in the aggregation.[84] SRFA has high steric repulsions resulting in a very high energy barrier for aggregation. Therefore, the observed decrease in aggregation for SRFA is to be expected. Domingos *et al.* suggest that the increase in the aggregation for higher pH conditions was due to a different mechanism involving bridging of nanoparticles by SRFA.

Because aggregation behavior can be altered upon coadsorption of other species, sedimentation studies were also conducted in the presence of both citric acid (3 mM) and oxalic acid (3 mM) at pH 2.0 and 6.0 (Figure 3.10). These data show that the aggregation behavior of TiO_2-citrate prevails even in the presence of oxalic acid and shows that TiO_2 has a greater affinity toward citric acid compared to oxalic acid.

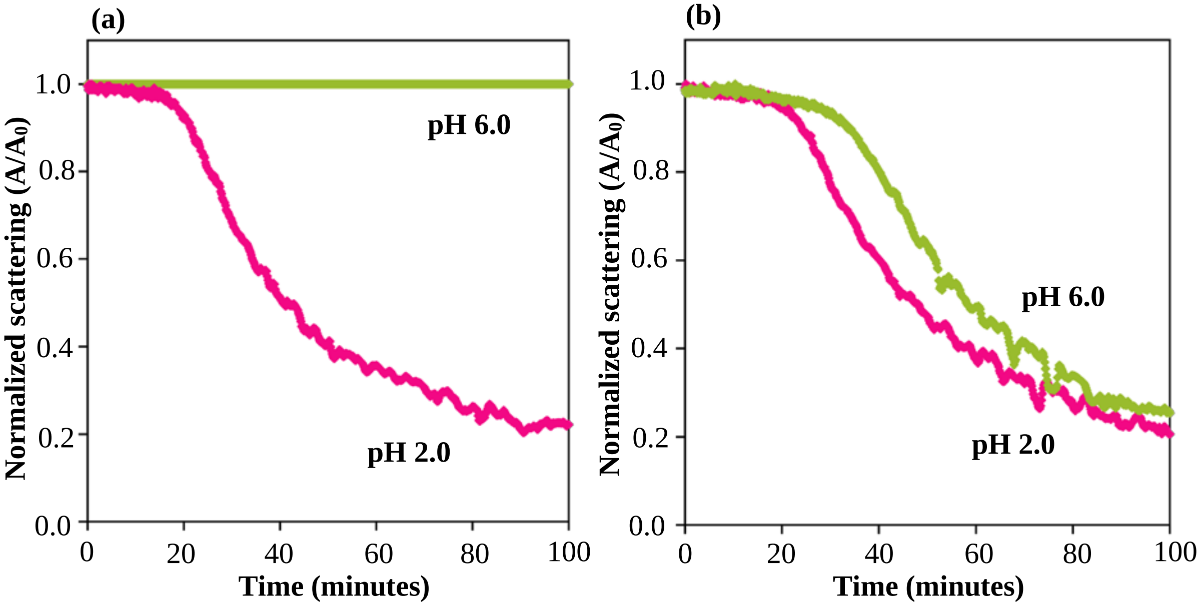

Figure 3.10: Sedimentation plots for TiO_2 in the presence of (a) both citric acid and oxalic acid (b) only oxalic acid. The aggregation behavior shows that citric acid determines the stability of these nanoparticle suspensions even in the presence of oxalic acid.

Aggregation of nanoparticles is of great significance to its environmental fate and transport.[21,23,84,112] The larger aggregates are known to sediment out which will limit their distribution in the environment. Furthermore, recent studies have shown that the ability of nanoparticles to undergo dissolution can be quenched upon aggregation.[102,105] This study shows that at near circumneutral conditions citrate has an inhibiting effect on TiO_2 nanoparticle aggregation leading to potentially high distribution. As citrate is also abundant in human plasma, upon inhalation of these nanoparticles, there is a greater risk of them distributing throughout the body as well. The true extent of these implications is yet to be realized due to lack of quantitative data for nanoparticle levels in the environment and in vivo. Although the behavior of nanomaterials in the environment or in vivo remains uncertain due to the complex nature of the milieu, a summary of the results discussed here with respect to nanoparticle-nanoparticle interactions at different pH and the impact of a citric acid, a common ligand, is presented in Figure 3.11 as a guide to begin to understand this complexity as it relates to the distribution and bioavailability of nanoscale TiO_2.

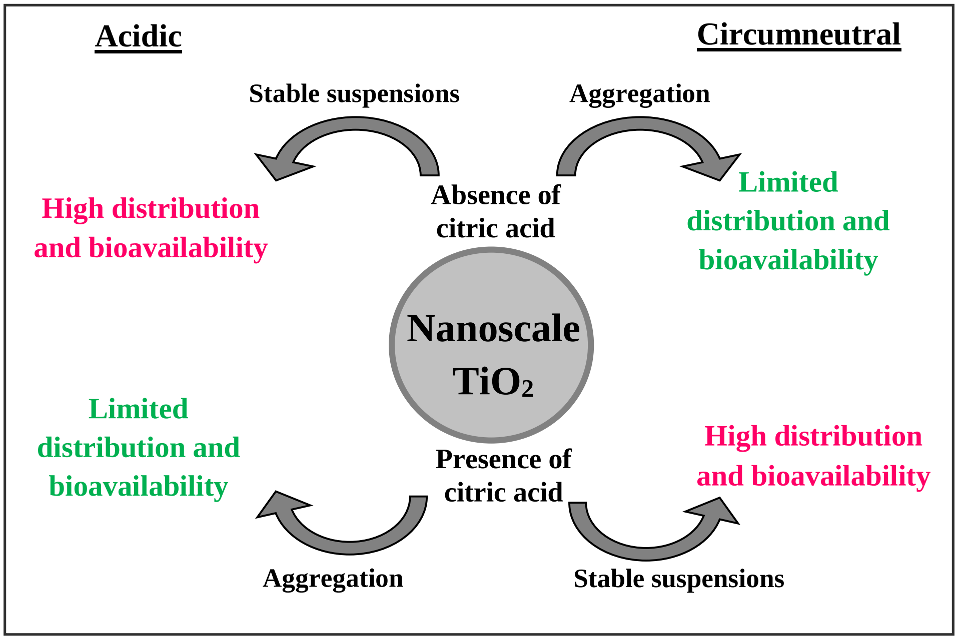

Figure 3.11: A summary of the behavior of nanoscale TiO_2 particles as a function of pH and citric acid at fixed ionic strength (0.03 M).

3.5 Conclusions and Implications

A number of interesting and important conclusions come from the results of these studies of citric acid adsorption as a function pH and its impact on nanoparticle-nanoparticle interactions. First, the adsorption of citric acid onto 4 nm TiO_2 nanoparticles is a pH dependent process with surface coverage decreasing as a function of pH. Second, although citric acid solution speciation is highly pH dependent in the range investigated here (2.0-7.5), surface speciation was found to differ and after equilibration shown to be the completely deprotonated form at highly acidic solution pH, and at pH 2.0, surface adsorption changes from a partially deprotonated form to the fully deprotonated form over time scales of minutes to hours. Thus, surface adsorption increases the acidity of citric acid resulting in a loss of protonated carboxylate groups lower than expectations based on solution pK_a values. Third, the adsorption of citric acid is irreversible at T = 293 K suggesting strong coordination to the surface which is indicative of an inner sphere complex to the surface with one or more carboxylic groups. Fourth, nanoparticle–nanoparticle interactions occur under all pH conditions considered but the degree of aggregation changes as a function of solution pH with the greatest degree of aggregation occurring around pH_{zpc} and the lowest in highly acidic pH. Fifth, the presence of citrate alters the aggregation behavior at both highly acidic and neutral pH conditions by altering the surface charge of the nanoparticles. At pH 2.0, this results in the destabilization of relatively stable suspensions in the presence of citrate with the formation of aggregates. In contrast, at pH 6.0, TiO_2 suspensions are unstable and large aggregates are present; however, in the presence of citrate, aggregation was hindered and suspensions were more stable. These trends observed in aggregation of TiO_2 nanoparticles in the presence of citrate are of environmental and biological significance as aggregation plays a key role in controlling the distribution of these particles in aquatic environments and cellular matrices as well as in the body where citric acid is found in abundance. Thus, the studies discussed here provide important insight into the behavior of some of the smallest TiO_2 particles and their surface chemistry with citric acid.

Furthermore, it is well-known that the development of nanomaterials for use in a wide range of fields including medicine, solar energy conversion, water purification, and catalysis is of great interest.[21,23,124,149,150] [151]Among a large number of these engineered nanomaterials, nanoscale TiO_2 is of great interest due to some of its unique characteristics, including its high refractive index for use in plastics, enamels, artificial fibers, electronic material, and rubber. Its ability to absorb solar light makes it useful in solar panels. It is a self-cleaning disinfectant, an effective photocatalyst, and a good support material for heterogeneous catalysts.[150]

With increasing use, recent studies have in fact shown that TiO_2 is in the environment and indeed have found convincing evidence of its presence both in the atmosphere and hydrosphere. In some cases, there is evidence that it is from anthropogenic sources.[44,45]A study conducted by Kaegi *et al.* shows the emission of engineered TiO_2 nanoparticles from the exterior facades into natural water and the presence of these particles in the urban runoff.[45] Zheng *et al.* has detected Ti-rich inhalable particulates in the atmosphere.[44] An exposure model developed by Mueller *et al.* has suggested annual worldwide production of nanoscale TiO_2 as of 2008 is nearly 5000 tons, hence, increasing the potential of this material getting into the environment.[21] The model simulation predicts 1.5×10^{-3} µg m^{-3}, 0.7 µg L^{-1} and 0.4 µg kg^{-1} of nanoscale TiO_2 in air, water, and soil, respectively. Grassian *et al.* has shown that subacute exposure of 2-5 nm sized TiO_2 nanoparticles results in moderate but statistically significant inflammatory responses among animals at weeks 0, 1, or 2 and resolves after 3 weeks.[139] Furthermore, the studies of Sun *et al.* on higher uptake of As(V) in aquatic animals in the presence of nanoscale TiO_2 highlight the enhanced transport of known contaminants via co-transport.[149] Thus, understanding the behavior of nanomaterials especially in natural water systems is complex due to a number of factors including pH, ionic strength, and the presence of complexing molecules.[84,86,148,152] Furthermore, nanoparticle aggregation adds to the complexity and questions the validity of high concentration-toxicity relationships due to a potential decrease in bioavailability of the aggregated particles.[23] Investigations of the behavior of nanomaterials in these simpler systems such as the ones discussed here offer some insights into their behavior in the more complex matrices found in nature.

Acknowledgment

The research described in this article has been funded in part by the Environmental Protection Agency through grant number EPA RD-83171701-0 to V.H.G. The authors would like to thank Dr. Shaowei Bian for help with DLVO calculations. The results of this work are presented in the publication under authorship of Imali A. Mudunkotuwa and Vicki H. Grassian, *Journal of American Chemical Society*, 2010, 132, 14986 – 14994.

CHAPTER 4

ENVIRONMENTAL IMPLICATIONS OF NANOPARTICLE AGING IN THE PROCESSING AND FATE OF COPPER-BASED-NANOMATERIALS

4.1 Abstract

Copper nanomaterials are being used in a large number of commercial products because these materials exhibit unique optical, magnetic, and electronic properties. Metallic copper nanoparticles, which often have a thin surface oxide layer, can age in the ambient environment and become even more oxidized over time. These aged nanoparticles will then have different properties compared to the original nanoparticles. In this study, we have characterized three different types of copper-based nanoparticle (NP) samples designated as Cu(new) NPs, Cu(aged) NPs, and CuO NPs that differ in the level of oxidation. The solution phase behavior of these three copper-based nanoparticle samples is investigated as a function of pH and in the presence and absence of two common, complexing organic acids, citric and oxalic acid. The behavior of these three copper-based NP types shows interesting differences. In particular, Cu(aged) NPs exhibit unique chemistry including oxide phases that form and surface adsorption properties. Overall, the current study provides some insights into the impacts of nanoparticle aging and how the physicochemical characteristics and reactivity of nanomaterials can change upon aging.

4.2 Introduction

Metal-based nanomaterials can be released accidentally into natural systems during the manufacturing process, transport, or use. Thus, these materials have the potential to increase regional amounts of metals in the environment which will have an effect on local ecosystems.[153] Copper and copper oxide nanomaterials in particular are being used as catalysts, superconductors, and lithium ion electrode materials.[2,154,155] Copper nanoparticles are also attractive candidates as nanofluids because of their high thermal conductivity.[52,156] Nanoscale copper oxide is a p-type semiconductor with applications in photovoltaic, magnetic storage, and electronic materials.[157-160] Additionally, the use of composite materials to create systems that combine the optical, electronic, and magnetic properties of nanoscale copper (or copper oxide) with other materials that increase thermal and mechanical properties is particularly attractive from an engineering perspective.[154,160,161]

In general, the physiochemical properties of materials will drive their fate and transport in the environment. The surface properties of nanomaterials in particular will govern the interactions of these materials with environmental interfaces and biological systems.[162-164] However, one important, but not well-understood consideration is how environmental processing and/or aging results in changes in the surface, composition, morphology, reactivity, and toxicity compared to the pristine or freshly synthesized nanomaterial. For example, Pan et al. have shown the formation of $ZnCO_3$ on ZnO nanostructures under ambient conditions.[165] Additionally, many metals can oxidize under ambient conditions. Therefore interfacial properties will be driven by the oxide layer present on the surface of the metal. Although the oxide layer can act as a protective coating for the metal core, conditions favoring dissolution can expose the underlying metal. Further modification can occur with the adsorption of ligands, such as organic acids, onto the surface of the nanomaterial.

Organic acids in natural aquatic systems can either inhibit or enhance dissolution and aggregation. These processes, dissolution and aggregation, directly affect the mobility and uptake of nanomaterials.[141] Plants release organic acids, such as oxalic acid and citric acid, to complex metals to increase uptake or employ defensive action against phytotoxicity.[141,166-168] These acids are also introduced into natural systems from industrial processes or purposefully introduced for mobilization and extraction of heavy metals.[169-171] Citric acid has been examined for the separation of metals from industrial sludge, chemical– mechanical polishing of copper, and extraction of metals from harbor sediments, and plays a role in metal and mineral processing.[169,172,173] The dissolution of metals can be promoted in some cases by these acids as a result of their chelating ability by polarizing the surface and weakening the surface metal–oxygen or metal–metal bonds. In the absence of dissolution, surface adsorption of organic acids can alter the surface charge and therefore subsequent interactions with environmental interfaces and biological systems.[141,168,174]

Copper and copper oxide nanoparticles have shown toxicological responses particularly in aquatic species and animal studies.[36,37,39,164] Because of this, we have undertaken a study of three different types of copper nanoparticles that differ in their level of oxidation. These are designated as Cu(new) NPs, Cu(aged) NPs, and CuO NPs. Here we investigate and compare the propensity for these copper-based NPs to become more mobile through dissolution and deaggregation in the presence and absence of citric acid and oxalic acid as a function of pH. A comparison of the aqueous behavior between newly purchased commercially manufactured Cu nanoparticles (Cu-(new) NPs), to nanoparticles that were allowed to sit in the laboratory environment for several years under ambient conditions (Cu(aged) NPs), is particularly interesting as it probes potential effects of aging on environmental processing and the fate and transport of these materials.

4.3 Experimental Methods

4.3.1 Nanoparticle Characterization

The bulk crystalline phases of these nanoparticles were examined using X-ray diffraction (Rigaku Miniflex II Diffractometer with a Co source). Nanoparticle size was determined by considering hundreds of randomly chosen particles using a JEOL JEM-1230 TEM. Surface areas were determined using a multipoint BET analyzer (Quantachrome). Samples were heated to 100 °C under vacuum for 18 h prior to analysis with triplicate measurements made on each sample. Surface composition was investigated using a custom-designed Kratos Axis Ultra X-ray photoelectron spectroscopy (XPS). This system and the analysis procedures used have been described previously.[175] The XPS binding energies were internally referenced to adventitious C peak at 286.4 eV.

4.3.2 Aqueous Phase Measurements.

Nanoparticle suspensions at a mass loading of 1 g/L were prepared at pH 3, 7, and 11 containing different concentrations of organic acid: 0, 0.1, 1, and 10 mM. Immediately after mixing these nanoparticles suspensions, samples were covered in aluminum foil to inhibit possible light-induced effects and placed on a circular rotator (Cole-Palmer) for 24 h. Aliquots of 1.5 mL were then drawn out, filtered with a 0.2-μm syringe-driven filter (Xpertec), and centrifuged for 30 min at 22 000 rpm. The remaining solution was analyzed using a Varian inductively coupled plasma optical emission spectrophotometer (ICP-OES) for soluble copper. The centrifuged samples (1 mL) were diluted to 7 mL with 1 M HCl solutions prior to analysis to solubilize any un-dissolved nanoparticles left in the supernatant during the filtration process.

Compositional changes of the powder that occurred during the processing were investigated by XRD analysis of the processed samples. Nanoparticles were treated with 10 mM organic acid at different pH as noted above, and the solid phase was collected after centrifuging and dried under vacuum overnight. Dried samples were immediately placed in airtight vials and analyzed using X-ray diffraction (Rigaku Miniflex II Diffractometer with a Co source).

4.3.3 ATR-FTIR Spectroscopic Measurements of Surface Adsorption.

Organic acid adsorption onto the surface of the nanoparticles was probed using a Thermo Nicolet FTIR spectrophotometer equipped with a MCT/A detector and a horizontal flow cell (AMTIR crystal, Pike Technologies, Inc.). A thin even coating of nanoparticles was formed by placing an aqueous solid suspension (1.5 mg/mL) on the crystal and allowing it to dry overnight. The deposited film was slowly flushed with a stream of water to eliminate any loosely bound particles followed by addition of the organic acid (10 mM) solution. Spectra were collected at 10-min time intervals for a period of 1 h. The contribution of the solution phase organic acids to these spectra was minimal at the concentrations used.

4.3.4 Sources of Nanomaterials and Chemicals.

Two different batches of copper nanoparticle samples were purchased from Nanostructure and Amorphous Materials, Inc. (Houston, TX) at different times. Both batches were in powder form and were stored in glass containers at 20 °C under atmospheric pressure (ambient conditions). One batch was newly purchased and used immediately to conduct experiments (Cu(new) NPs) and the other batch was purchased in 2006 and allowed to sit in the laboratory under ambient conditions (Cu(aged) NPs). Copper oxide nanoparticles were purchased from Sigma-Aldrich. Solution pH was adjusted using sodium hydroxide (NaOH; Fisher Scientific; certified ACS plus) and hydrochloric acid (HCl; Fisher Scientific; certified ACS plus). The aqueous solutions of citric acid/oxalic acid (Sigma Aldrich, 99.5% certified ACS plus) and all reactors were prepared using Optima water (Fisher Scientific).

4.4 Results and Discussions

4.4.1 Nanoparticle Characterization.

Powder XRD of the three nanoparticle samples − Cu(new) NPs, Cu(aged) NPs, and CuO NPs − shows the presence of different phases (Figure 4.1). The XRD pattern for Cu(new) NPs consists of three phases: a set of intense Bragg diffraction peaks which correspond to the *fcc* structure of metallic Cu along with weaker diffraction peaks due to

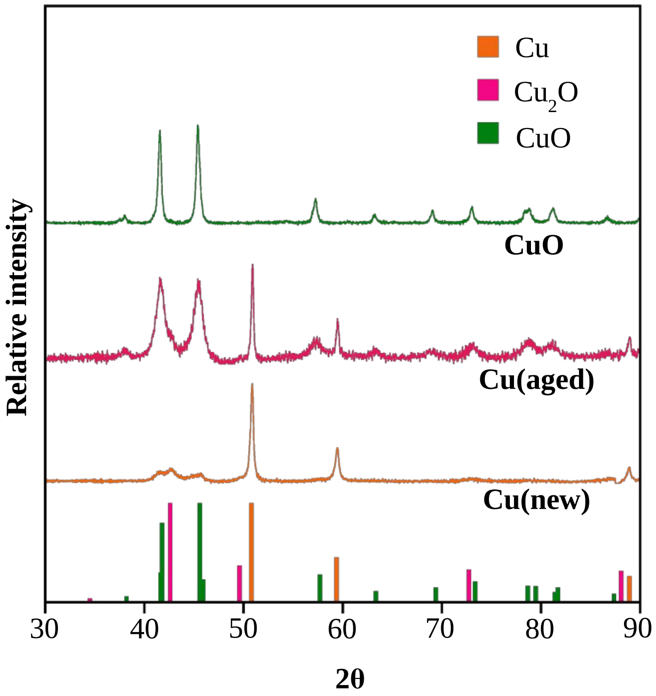

Figure 4.1: Characterization of Cu-based nanoparticles by X-ray diffraction

the presence of Cu_2O (cuprite) and CuO (tenorite). Cu(aged) NPs show the presence of only two phases – Cu (fcc metal) and CuO (tenorite) – with peaks of nearly equal intensity for the two. Cu_2O was not observed in the XRD patterns of Cu(aged) NPs even though Cu_2O was observed for these nanoparticles before aging.[26] CuO NPs show only one phase – the tenorite crystalline phase.

Although bulk compositions of these three samples differ significantly, surface analysis by XPS yields similar surface composition as revealed by the Cu *2p* binding energy region shown in Figure 4.2. Peaks at 933.4 and 953.5 eV in XPS correspond to the Cu $2p_{3/2}$ and Cu $2p_{1/2}$ photoelectrons in CuO, respectively,[39,176] with shakeup satellite peaks at higher binding energies (941.2, 942.9, and 961.7 eV). XPS data in the O *1s* binding

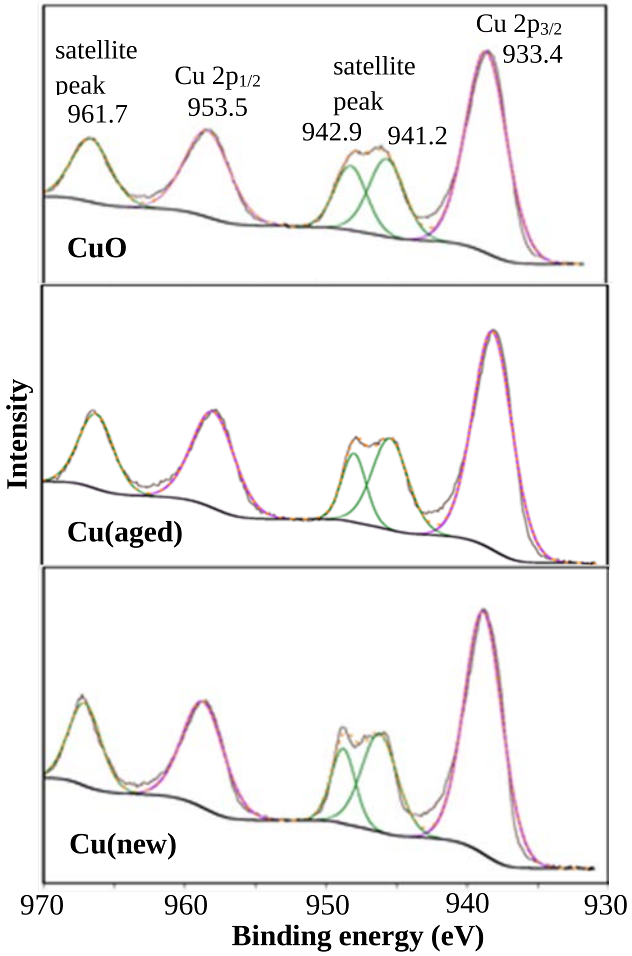

Figure 4.2: Surface analysis of Cu-based nanoparticles by X-ray photoelectron spectroscopy.

energy region show the presence of – OH functional groups on the surface of all three samples as well as some CO_3^{2-} as evidenced by the C *1s* binding energy region (Figure 4.3a).[177,178] In addition to carbonates, there are two other peaks with lower binding energy in the carbon region (Figure 4.3b). One is due to so-called adventitious carbon and the other may be due to carboxylate carbon of organic precursors that may have been used in the synthesis of the nanoparticles.[178]

TEM images and the size distribution of all three samples are given in Figure 4.4. Cu(new) NPs are heavily aggregated and, upon careful inspection, show an average primary particle size of 10 ± 5 nm. Cu(aged) NPs have an even wider size distribution with the TEM image showing small particles as well as much larger particles and an

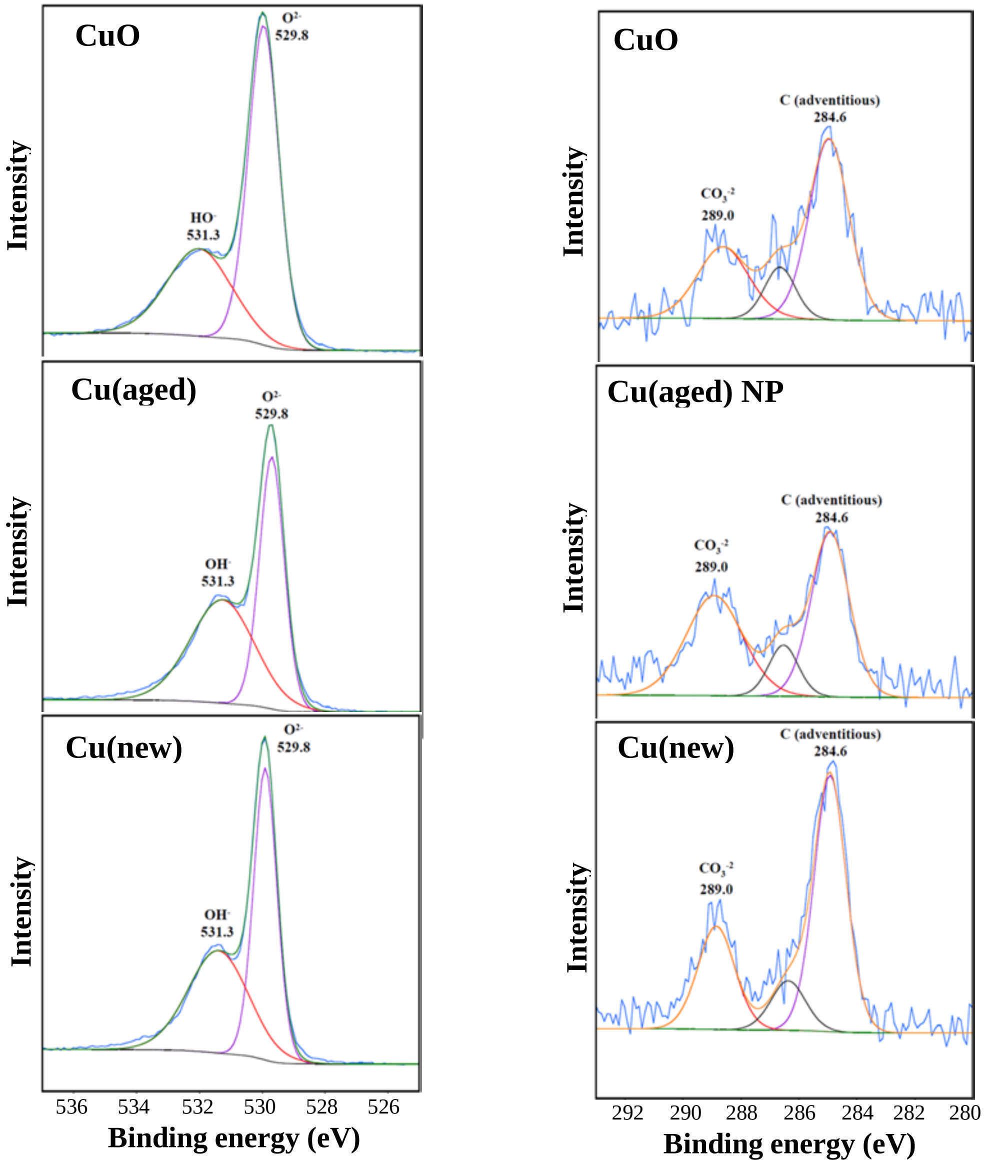

Figure 4.3: XPS spectra in the (a) O *1s* and (b) C *1s* region for the nanoparticles.

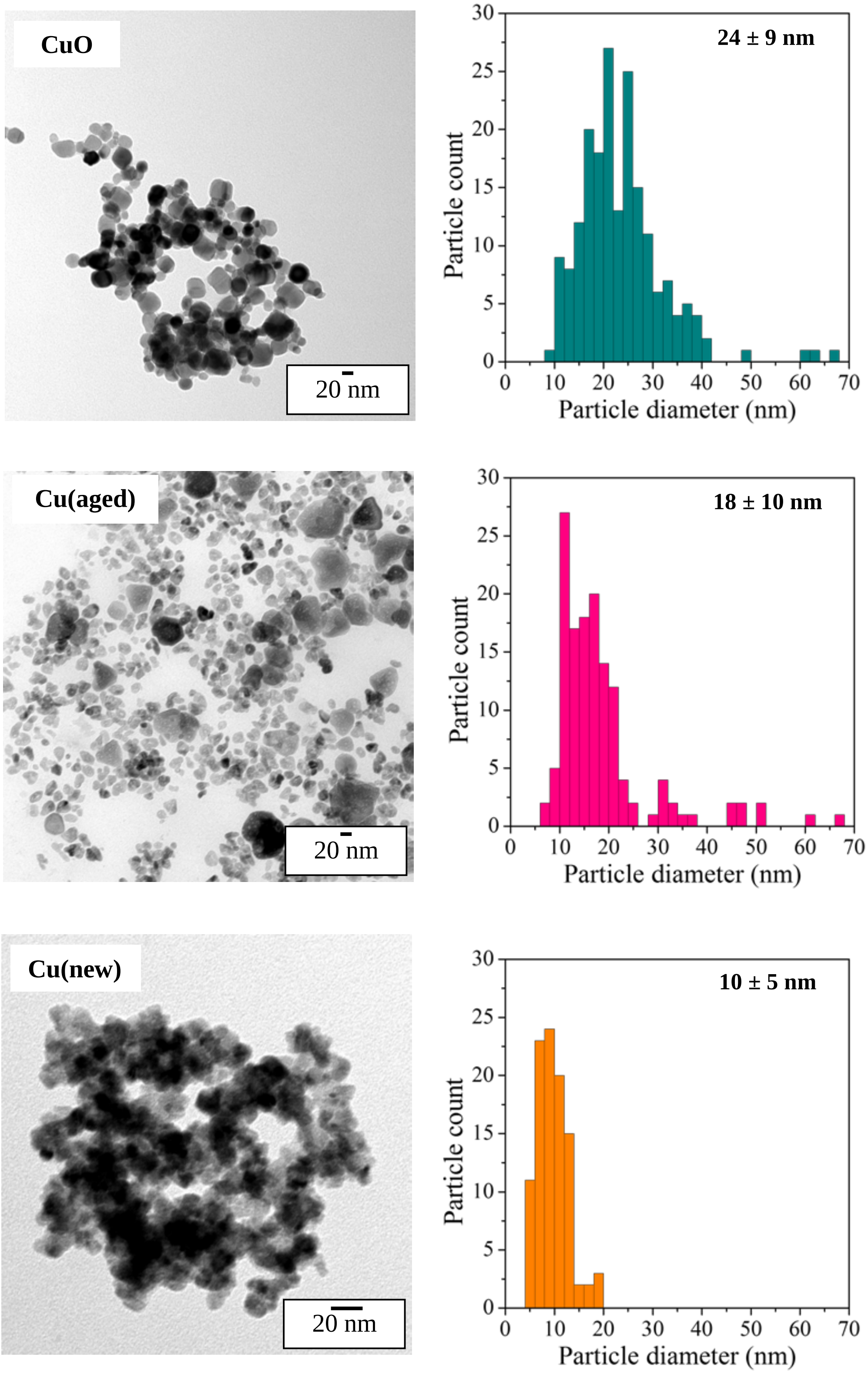

Figure 4.4: Transmission electron microscopy (TEM) images and respective size distribution of Cu(new) NPs, Cu(aged) NPs and CuO NPs.

overall average primary particle size of 18 ± 10 nm. Prior to aging, the Cu(aged) NPs sample showed an XRD pattern similar to the Cu(new) NPs and a narrower size distribution of 12 ± 1 nm.[39] Current analysis shows an increase in the average up to 18 ± 10 nm which was greater than the expected size increase (15 nm) assuming a size increase due oxidation. One plausible explanation consistent with the observed size increase is the coalescence of these nanoparticles. Magdassi *et al*. observed coalescence of Ag nanoparticles at room temperature when they were supported on a solid substrate and in contact with an oppositely charged polyelectrolyte.[179] Grouchko *et al.* showed with in situ HRTEM that close contact between Ag nanoparticles led to formation of larger particles with the original crystal structure.[180] Similar behavior can occur for Cu NPs as well and the images in Figure 4.4 clearly show several particles with diameters >30 nm, consistent with coalescence. CuO NPs are larger in size than both Cu NP samples with a mean diameter of 24 ± 9 nm. It should be noted that all of these TEM images were obtained after ultrasonication of a NP – methanol suspension for 5 min. This treatment did not break up the Cu(new) NP aggregates suggesting they are “tightly formed aggregates”. This is consistent with the BET surface area reported for Cu(new) NPs of 9 ± 1 m^2/g which is much lower than the calculated surface area of 67 m^2/g assuming a perfect sphere with diameter of 10 nm indicating the measured surface area is controlled by aggregation. Cu(aged) NPs give a BET surface area of 28±4 m^2/g below a calculated surface area of 37 m^2/g. The fact that the BET and calculated values are closer for the aged materials suggest that upon oxidation there is a weakening of particle‒particle interaction. In fact Cu(aged) NPs de-aggregate upon ultrasonication more readily indicating that these aggregates are not as tightly bound as Cu(new) NPs. BET surface area of CuO NPs was also affected by aggregation and gave a lower measured value (22 ± 0.4 m^2/g) than calculated (40 ± 15 m^2/g). The characterization data for all three different nanoparticles investigated (Cu(new) NPs, Cu(aged) NPs, and CuO NPs) are summarized in Table 4.1.

Table 4.1: Summary of physicochemical characterization data of Copper based nanoparticles

	Cu (new)	**Cu (aged)**	**CuO**
Phase	Cu, Cu_2O, CuO	Cu, CuO	CuO
Primary Particle Size	10 ± 5 nm	18 ± 10 nm	24 ± 9 nm
Measured Surface Area	9 ± 1 m^2 g^{-1}	28 ± 4 m^2 g^{-1}	22 ± 0.4 m^2 g^{-1}
Calculated Surface Area	67 ± 34 m^2 g^{-1}	37 ± 20 m^2 g^{-1}	40 ± 15 m^2 g^{-1}
Surface Functionalization	O, O-H and CO_3^{2-}	O, O-H and CO_3^{2-}	O, O-H and CO_3^{2-}

4.4.2 Aqueous Phase Behavior in the Presence and Absence of Organic Acids.

Nanoparticle dissolution has remained a point of discussion with respect to both environmental and health impacts as it is often debated whether impacts are due to the ions or the nanoparticles for the particles that do dissolve. However, an often overlooked fact when conducting dissolution studies is both dissolved ions and smaller suspended nanoparticles have higher mobility and bioavailability compared to the aggregates. Therefore, suspended nanoparticles are often removed from the medium by ultrafiltration. But if true environmental conditions are to be considered, both dissolved and some amounts of suspended smaller particles will inevitably be present. Furthermore, from a nanotoxicology perspective these suspended particles maybe of greater importance as these nanoparticles can be internalized and trigger reactive oxygen species generation or dissolve intracellularly.[164] Therefore, in this current study, we have measured the "total mobilized concentration (TMC)" of Cu(new) NPs, Cu(aged) NPs, and CuO NPs under acidic, neutral, and basic conditions with varying concentrations of organic acids. This fraction consists of dissolved Cu ions and the suspended smaller particles after 0.2-μm filtration to remove larger aggregates (>200 nm) and centrifugation at 22000 rpm (30 min) to remove some additional smaller aggregates (<200 nm). The supernatant changed from initially colorless to blue confirming the presence of Cu^{2+} in the solution from nanoparticle dissolution. TEM analysis of the supernatant confirmed the presence of some remaining nanoparticles as well (Figure 4.5). Upon dilution with 1 M HCl, any remaining nanoparticles completely dissolve into ions. The objective of using 1 M HCl for the dilution is to dissolve all the suspended nanoparticles such that the ICP-OES analysis can accurately quantify the “total mobile Cu concentration”.

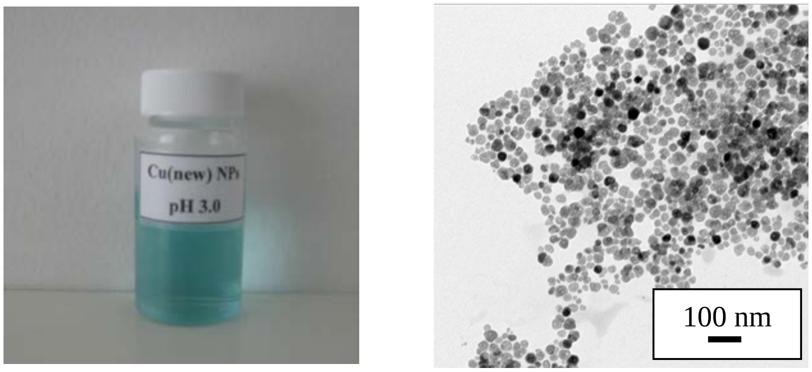

Figure 4.5: The color change of the supernatant of Cu(new) NPs after 24 hours confirming the release of Cu^{2+} by dissolution of the particles and the presence of smaller nanoparticles in the TEM images of the supernatant after filtration and centrifugation.

The results of these solution phase experiments are shown in Figure 4.6. In the absence of organic acid, all three NPs, Cu(new), Cu(aged) NPs, and CuO NPs, behave similarly and showed the highest total mobilized concentration (TMC) under acidic conditions (Cu(new) NP: 21±1 mg/L, Cu(aged) NP: 15±1 mg/L, CuO NP: 25±1 mg/L). This concentration enhanced significantly (~10 fold) in the presence of citric acid for the Cu(new) NPs irrespective of the solution pH and, at a concentration of 10 mM, ranged between 192 ± 34 and 230 ± 30 mg/L. As citric acid is a good chelating complex its

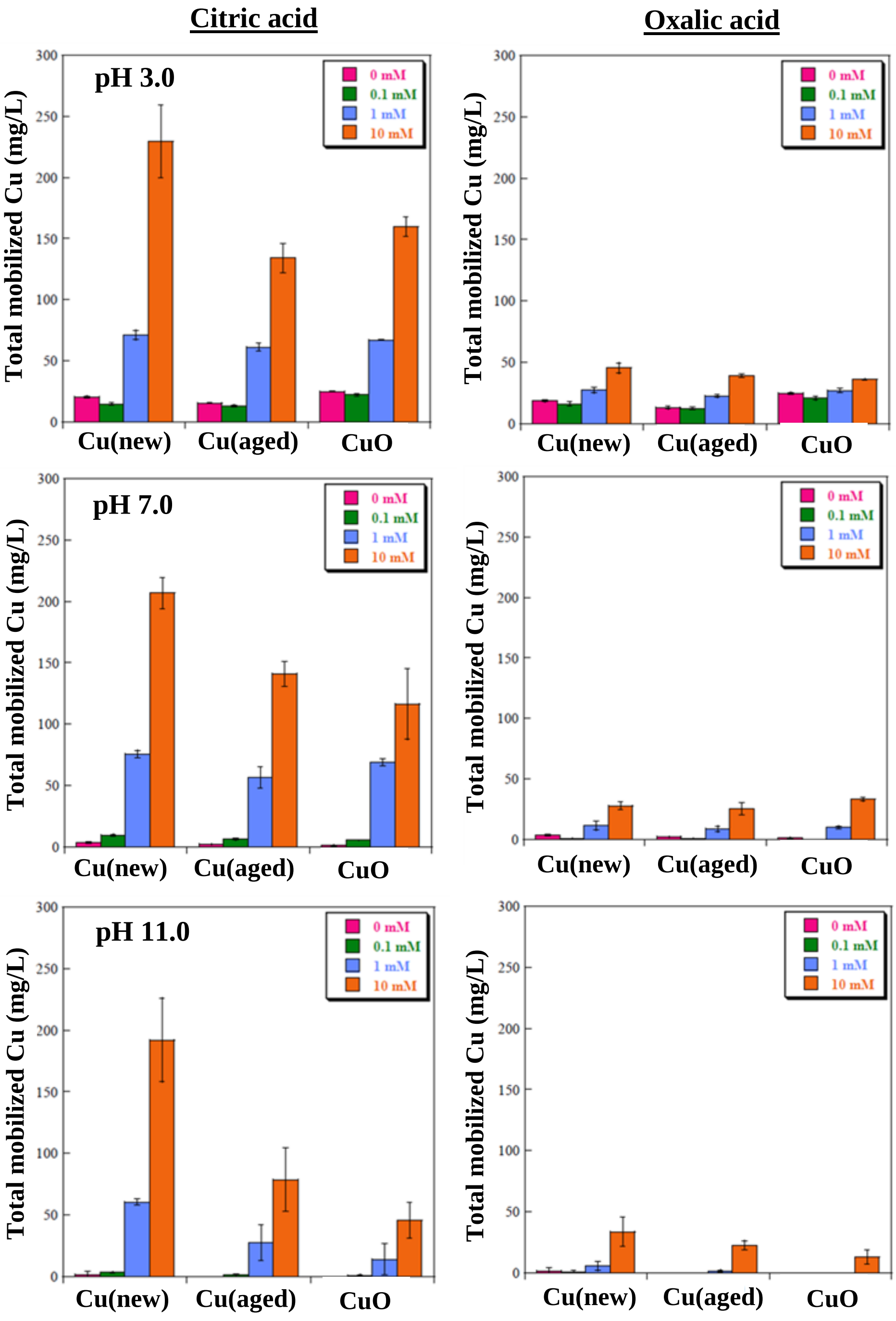

Figure 4.6: Total mobilized concentration (TMC) of Cu(new) NPs, Cu(aged) NPs and CuO NPs (1 g/L) as a function of organic acid concentration under varying pH conditions. TMC = dissolved Cu ions + suspended Cu nanoparticles (see text for further details)

presence can result in enhanced dissolution exposing the core of Cu(new) NPs because of its thin oxide layer. Cu(aged) NPs and CuO NPs also showed an enhancement in TMC which decreased with increasing pH. This enhancement was significantly less than that found for Cu(new) NPs. Cu(aged) NPs behave more similarly to CuO NPs than Cu(new) NPs as a result of the thick oxide coating.

Oxalic acid has a less pronounced effect compared to citric acid. There were no appreciable differences among the three copper NPs. Because oxalic acid does not promote dissolution as much as citric acid it may not dissolve the surface oxide layer completely. Thus the different cores remain unexposed leading to similar solution-phase behavior. The highest total mobilized concentration was found in the presence of highest concentration of oxalic acid and remained below 50 mg/L even at acidic pH for all the samples. As the solution pH increased, for lower concentrations of oxalic acid very small amounts of dissolved or suspended particles were detected for Cu(aged) NPs and CuO NPs. However, Cu(new) NPs showed a relatively higher TMC with oxalic acid compared to Cu(aged) NPs and CuO NPs at alkaline pH.

XRD patterns of the organic acid processed Cu(new), Cu(aged), and CuO NPs shown in Figure 4.7 reveal very interesting differences. Low pH solutions favor the formation of Cu2O from Cu NPs. For Cu(new) NPs, there is 100% conversion to Cu2O upon drying from both citric and oxalic acid solutions. For Cu(aged) NPs, some of the CuO phase remains with citric acid and with oxalic acid both CuO and Cu core has been retained. The thick oxide coating of the Cu(aged) NPs acts as a barrier for the oxidation of the metal core. The difference in behavior in the presence of citric and oxalic acid for the Cu(aged) NPs can be attributed to the extent of dissolution of the oxide coating. The greater dissolution with citric acid exposes the metal core whereas limited dissolution with oxalic acid retains some of the metal core. However, the presence of CuO in Cu(aged) NPs after processing which is not observed with Cu(new) NPs indicates that the thickness of the oxide coating is not uniform around the particle. At neutral pH Cu(new)

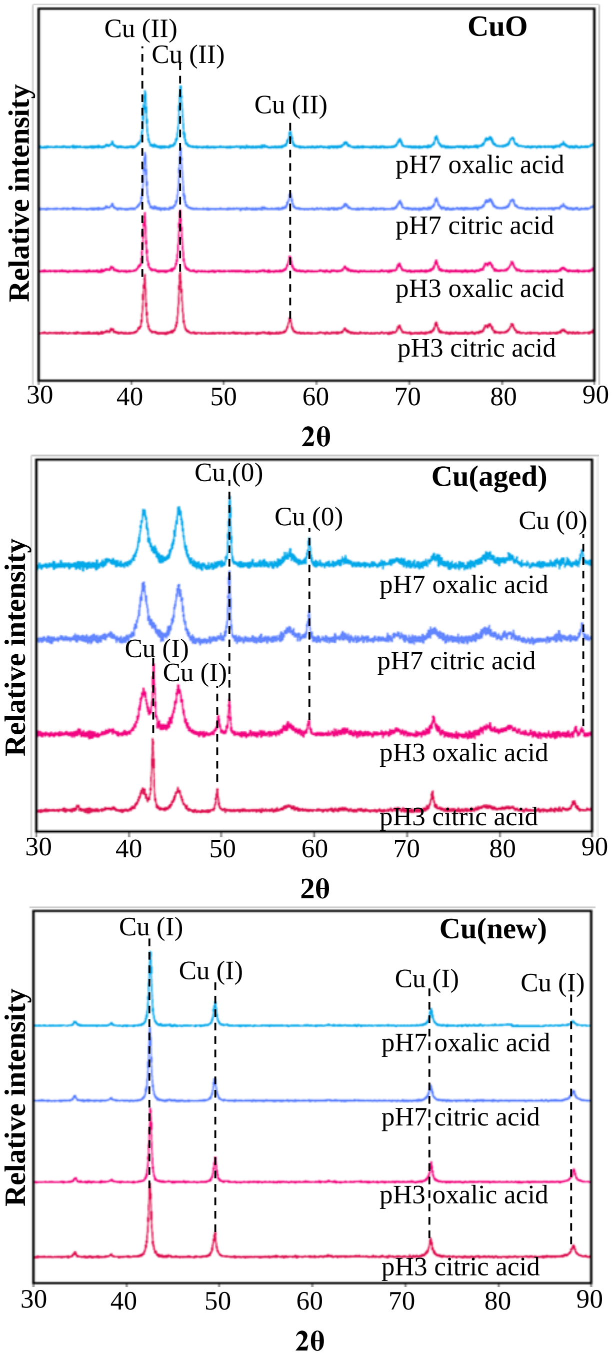

Figure 4.7: XRD patterns of organic acid processed Cu(new) NPS, Cu(aged) NPs and CuO NPs after drying.

NPs converted quantitatively to Cu_2O while Cu(aged) NPs did not undergo any phase transformation and showed composition similar to the unprocessed samples. This confirms that under neutral pH, the dissolution of the thicker oxide coating is insufficient to expose the Cu core for oxidation. CuO samples did not show any phase transformations under any of the conditions investigated and remained CuO under all conditions.

4.4.3 Surface Adsorption Measurements.

ATR-FTIR spectroscopy can provide molecular level insights into the adsorption of these environmentally important organic acids on nanoparticle surfaces. In these spectroscopic measurements, only oxalic acid was investigated as the extent of dissolution was too great in the presence of citric acid. Additionally because of their light absorption properties in the infrared region, Cu(new) NPs are not amenable to these measurements. Therefore, surface adsorption measurements shown here are for Cu(aged) and CuO NPs.

Figure 4.8 shows solution phase and adsorbed oxalic acid spectra on Cu(aged) and CuO NP at pH 3.0 and 7.0. Note that the solution-phase reference spectra are at a concentration ten times greater than the concentrations used to investigate surface adsorption. For solution-phase oxalic acid (with $pK_{a1} = 1.3$ and $pK_{a2} = 4.3$), several peaks are observed at pH 3.0. The carbonyl group stretch (C=O) can be seen at 1722 cm^{-1} for the protonated carboxylic group of oxalic acid and the peaks at 1576 cm^{-1} and 1308 cm^{-1} correspond to the asymmetric and symmetric stretch of the deprotonated carboxylate group.[181,182] The bands at 1243 cm^{-1} and 1406 cm^{-1} are assigned to ν_s(CO)+ δ(O−C=O) and ν_s(C−O)+ν_s(C−C) vibrations, respectively.[183] The shoulders observed at 1700, 1613, and 1440 cm^{-1} are a result of the presence of oxalic acid dimers in solution.[182,183]At pH 7.0 ($>pK_{a2}$), completely deprotonated species are present and only peaks for the symmetric and asymmetric stretching of the carboxylate groups are observed.

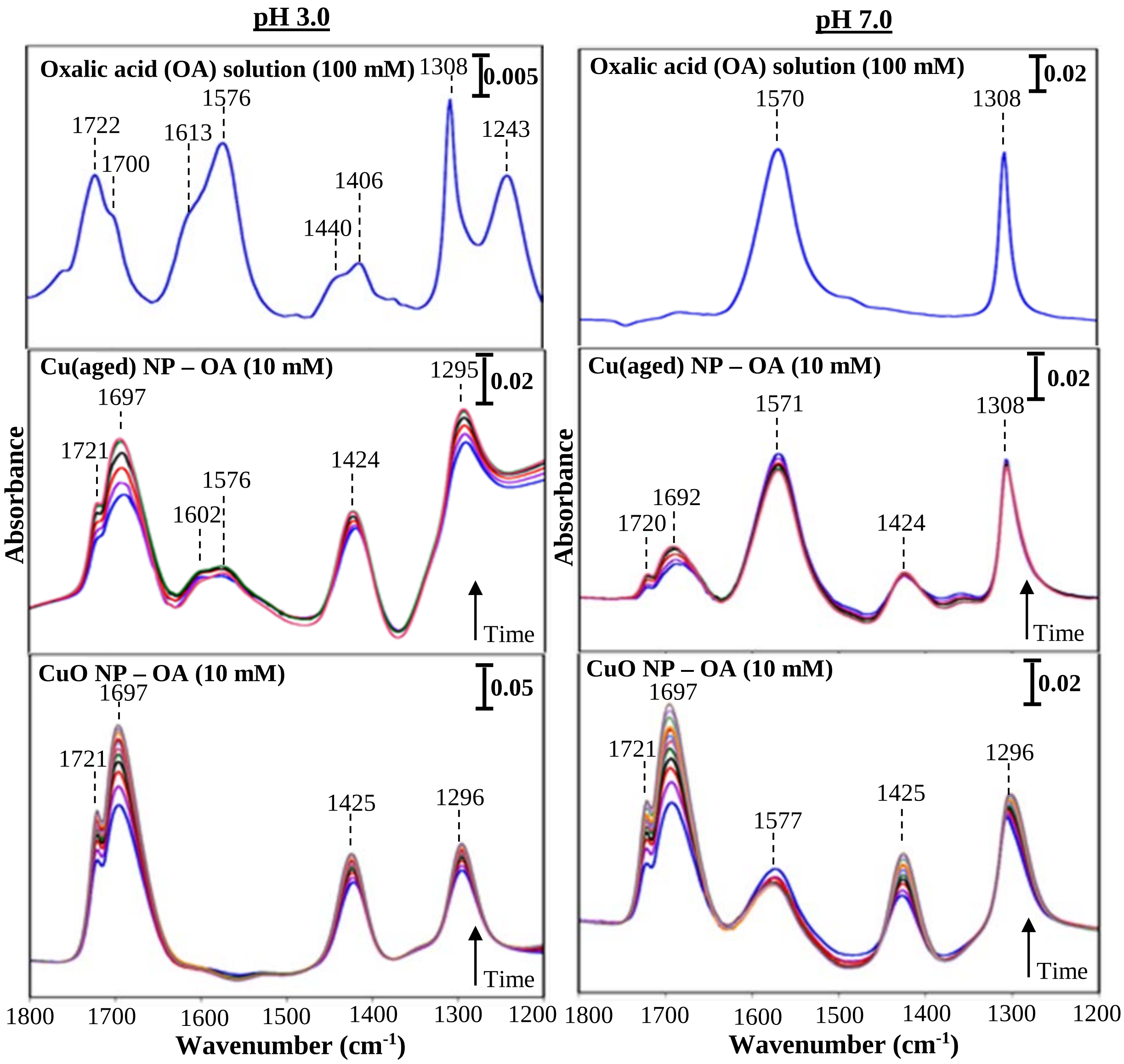

Figure 4.8: ATR-FTIR spectra of solution phase (100 mM) and adsorbed oxalic acid (10 mM) on Cu(aged) NPs and CuO NPs at pH 3.0 and pH 7.0.

Surface-adsorbed oxalic acid shows differences from the solution-phase species (Table 4.2). At pH 3.0, both Cu(aged) and CuO NP spectra show intense peaks at 1721, 1697, 1424, and 1295 cm^{-1}. Due to vibrational coupling of the two C=O stretching motions, there are absorptions at 1721 and 1697 cm^{-1}.[142] The bands at 1425 and 1295 cm^{-1}

Table 4.2: ATR-FTIR peak assignment for the adsorption of oxalic acid (10 mM) on Cu(aged) and CuO NPs.

Mode of vibration	**Wavenumbers (cm^{-1})**	
	solution	**adsorbed**
ν_s(C=O)	1722	-
ν_s[(C=O)+ ν_s(C=O)]	-	1721
ν_{as}[(C=O)+ ν_s(C=O)]	-	1692-1697
ν_{as}(COO^-)	1570-1576	1570-1577
ν_s[(C-O)+ ν_s(C-C)]	1406	1425
ν_s[(C=O)+ ν_s(C=O)]		1295
ν_s(COO^-)	1308	1308
ν_s(C-O)+δ(O-C=O)	1243	-

correspond to the symmetric and asymmetric combination of C−O and C−C vibrations, respectively.[142] These spectral features suggest a bidentate bridging surface complex where the single-bonded oxygen of the carboxyl groups (O=C−O^-) coordinates with a Cu metal centers on the surface. In addition to these absorptions, Cu(aged) NP spectra show low intensity peaks at 1602 and 1576 cm^{-1} as well as a shoulder at 1308 cm^{-1} which is not observed for CuO NPs. Compared to the solution-phase spectrum, these can be attributed to weakly bonded oxalic acid species on Cu(aged) NPs. Thus these data suggest that for CuO NPs only monolayer adsorption occurs, whereas for Cu(aged) NPs there may be additional binding sites or multilayer adsorption. It is interesting to note that both samples have the same surface composition yet Cu(aged) NPs behave differently toward the same ligand. This observation is seen to an even a greater extent at pH 7.0 where the intensity of peaks at 1571 and 1308 cm^{-1} dominate over the peaks at 1720, 1692 and 1424 cm^{-1} for

Cu(aged) NPs. Because at this pH both carboxylate groups are deprotonated, these peaks can also be attributed to bidentate-chelating coordination of one of the carboxylate groups to the surface.[142] CuO NPs also show similar peaks but their intensities are much lower suggesting that at pH 7.0 oxalic acid adsorption modes may differ from those of Cu(aged) NPs. As the net interaction between nanoparticles and oxalic acid is controlled in part by the surface charge under the given experimental conditions, this suggests that although aging of Cu NPs result in similar surface composition, CuO, the surface charge may be affected by the underlying Cu core.

4.5 Conclusions and Implications

The aging of Cu NPs has profound effects on its size, size distribution, bulk composition, and surface properties. Aged nanoparticles show an increase in the average particle size and a shift in the size distribution as a result of coalescence and coarsening under ambient conditions of temperature and relative humidity. The resulting particles are intermediate but also differ in composition when compared to Cu(new) NPs and CuO NPs. For example, no Cu(I) phases are present in the aged particles compared to Cu(new) NPs and the distribution of the CuO layer may be non-uniform. Because these physicochemical characteristics govern the nanoparticle properties, aged nanomaterials can be expected to give rise to unique chemical behavior as evidenced here. Thus, nanoparticle aging is an important aspect to be considered in the environmental and health implications of nanomaterials. The oxidation of Cu occurs readily in ambient conditions and Cu(I) and Cu(II) present on the oxidized surface can be released into the solution. For the HCl acidified samples in the current study, the following reactions can occur.

$$Cu_2O_{(s)} + 2HCl_{(aq)} \rightarrow 2CuCl_{(s)} + H_2O_{(l)} \qquad (Eq: 4.1)$$

$$CuO_{(s)} + 2HCl_{(aq)} \rightarrow 2CuCl_{(s)} + H_2O_{(l)} \qquad (Eq: 4.2)$$

Previous studies show these reactions to lead to the formation of paratacamite (γ-$Cu_2(OH)_3Cl$) in the presence of concentrated HCl.[184] In the current study presence of organic acids inhibited this formation and resulted in converting the Cu metal into Cu_2O for both Cu(new and aged) NPs. A detailed mechanism for atmospheric corrosion of copper in the presence of organic acid (L) under high relative humidity (85−95%) has been proposed by Harveth *et al.*[185] According to that mechanism, the organic acid (L) initially forms a surface complex with Cu^0 which reacts with dissolved O_2 to form Cu_2O and CuL_2. CuL can then reform and the process repeats itself converting all Cu^0 to Cu_2O.

$$4CuL + 1/2\, O_2 \rightarrow Cu_2O + 2CuL_2 \qquad (Eq: 4.3)$$

$$CuL_2 + Cu^0 \rightarrow 2CuL \qquad (Eq: 4.4)$$

The formation of Cu_2O occurs only with the adsorption of the organic acid on Cu^0 centers. This mechanism agrees well with the XRD patterns obtained for the processed samples (Figure 4.7). Cu(new) NPs showed the formation of Cu_2O because it has a thin oxide coating that dissolves away rapidly. For Cu(aged) NPs, Cu_2O formation occurs only at pH 3.0 when the Cu core becomes exposed following dissolution of the thick oxide coating. At pH 7.0, no Cu_2O is formed from Cu(aged) NPs as the dissolution is limited and thus does not expose the underlying metallic Cu core. It is interesting to note that Cu_2O formation by Cu(aged) NPs relate well with the type of organic acid which enhances dissolution of the oxide coating to a greater extent. Once Cu_2O forms on the surface there are two possible pathways. The surface can continue to dissolve away exposing more Cu^0 for organic acid adsorption or given that Cu_2O is a p-type semiconductor with negatively charged vacancies mass transport of Cu^+ ions and electrons can occur in a direction normal to the surface via the vacancies.[186] In the current study, both these pathways are in fact plausible. Because CuO NPs did not contain any metallic Cu, no formation of Cu_2O occurred. These results also show the unique nature of Cu(aged) NPs in solution.

Ligand-promoted dissolution of Cu and CuO nanoparticles in the presence of organic acid increases their mobility in natural environments by the formation of ions and smaller nanoparticles. Enhancement in dissolution and mobility depends on the nature of the organic acid and pH. Citric acid causes the greatest dissolution and mobility. Citric and oxalic acid interact weakly or strongly by forming outer-sphere or inner-sphere complexes, respectively. The strength of the interaction is sensitive to the pH as it determines the solution speciation of the acid as well as the surface charge (Figure 4.9).

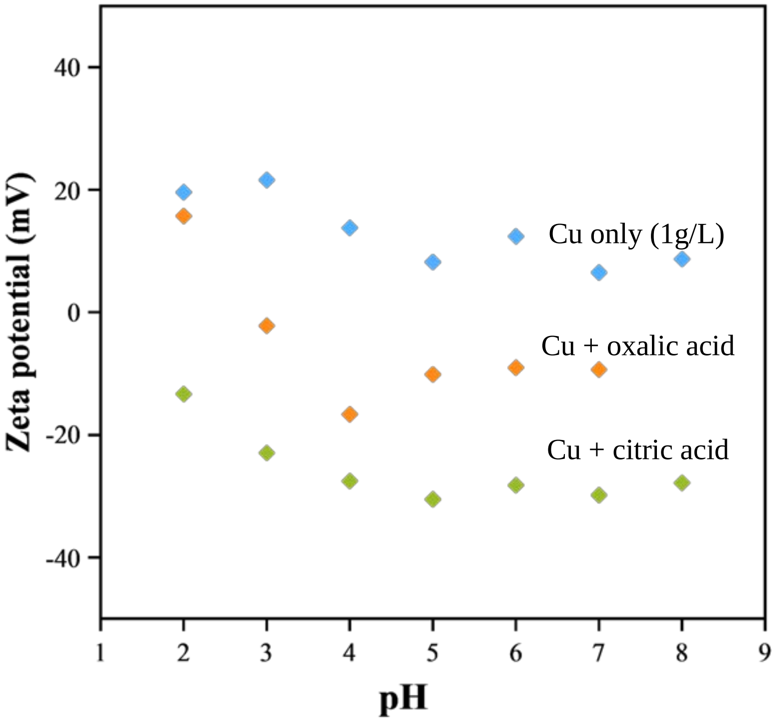

Figure 4.9: Zeta potential of the Cu(aged) NPs as a function of pH in the presence and absence of organic acids. Data indicates the generation of a negative charge on the surface of the nanoparticles. Citric acid (green) shifted the charge to more negative values as compared to the oxalic acid (orange).

Smaller suspended nanoparticles can potentially be taken up by plant roots and aquatic species resulting in bioaccumulation and biomagnification. Therefore "total mobilized concentration" can potentially give a more accurate measure of bioavailability from an environmental perspective. However it is important to note that because dissolved Cu ions have a greater affinity toward humic-like organic substances and form insoluble complexes which get incorporated into the organic fraction in the soil system, the mobilization can in fact be inhibited although the dissolution is enhanced.[169] Thus, it is important to study and understand competing processes that occur in natural environments.

Furthermore, the possibility of threshold coverage has been observed for strongly bonded organic acids. Axe and Persson studied the dissolution caused by different surface speciation of oxalate on the boehmite (γ-AlOOH) surface and showed evidence of a critical concentration needed to induce dissolution.[187] The critical surface concentration was correlated to the inner-sphere complex concentration present on the surface; therefore, less than or equal concentrations of the inner-sphere complexing of oxalate on the surface created a semi-protected, stable surface. In the current study a similar decrease in dissolution was consistently observed at all pH with lower oxalic acid concentration. Therefore, at appropriate concentrations, oxalic acid can be considered as a dissolution inhibitor rather than a promoter. Solution-phase chemistry will also play an important role in the dynamic processing of copper nanoparticles because the type of solution-phase complexes that are formed between Cu^{n+} (where n = 1 or 2) and organic acids are dependent on the relative ratios of the metal and ligand.[188] When no or limited dissolution occurs, the adsorption of organic acids changes the surface charge of these nanoparticles (Figure 4.9) and affects their aggregation behavior (Figure 4.10).

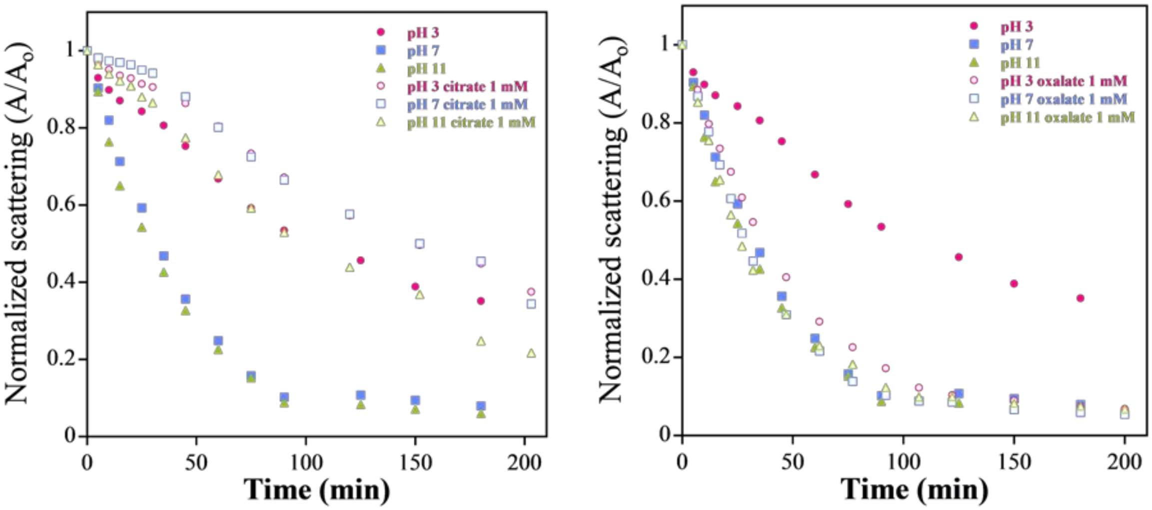

Figure 4.10: Sedimentation plots of Cu(aged) NPs in the presence (open points) and absence (solid points) of organic acids (1 mM) at pH 3, 7 and 11. All data is normalized to the initial absorbance.

In acidic environments and especially at pH < 5, the interactions with the organic acid strongly influence the termination of the surface. Electrostatic and Lewis acid−base reactions are the driving force for surface interactions and complexation of organic acid on copper nanoparticle surfaces. Sedimentation studies conducted for aged Cu-NP with and without organic acids at $\lambda = 512$ nm (Figure 4.10) show that the presence of citric acid decreases the aggregation as a result of increasing negative charge on the surface. Oxalic acid on the other hand increases aggregation by shifting the surface charge toward more neutral values. A study on α-Al_2O_3 showed that electrokinetic properties of surfaces are more greatly affected by citrate complexes than maleate or oxalate.[168] This is in good agreement with our findings where the surface charge was shifted to more negative values in presence of citric acid when compared to that of oxalic acid.

The effects caused by the adsorption of organic acid and consequent dissolution of copper in natural environments lead to increased metal ion concentrations, smaller particles that are more soluble and stable making them less easily separated in wastewater systems, and possibly increasing the bioavailability to both plants and animals. Traditionally, bioavailability is linked with solubility, but because of their size nanoparticles are in fact also bioavailable as nanoscale solid particles.[189,190] Further considerations are needed to account for the possibility of both soluble metal and solid metal nanoparticles being bioavailable. Soluble metal particles as well as nanoscale particles have been shown to increase the inflammatory response. Smaller particles may induce responses which may have different mechanistic pathways for inflammation compared to the dissolved ions.[191] For example, copper-containing nanoparticles showed that soluble copper induced an inflammatory response that was mechanistically different in zebrafish to the inflammatory response of 80 nm copper particles inferring that increased amount of soluble copper was not the sole cause of response.[36] Copper nanoparticles have shown to produce reactive oxygen species which can cause cytotoxicity.[192] There are also deleterious effects for increased concentrations of copper on microbial species.[193] However, the role of soluble ions versus the nanoparticles in toxicological responses has been reported with conflicting results for different transition metals. Therefore, a thorough understanding of possible environmental processes that can occur for Cu nanoparticles is a key requirement in elucidating the toxicological responses. This current study attempts to lay out some interesting differences in the solution phase behavior of different copper-based nanomaterials

Acknowledgment

The research described in this article has been funded in part by the Environmental Protection Agency through grant number EPA RD-83171701-0 to V.H.G. The authors would like to thank Dr. Jonas Baltrusaitis for XPS measurements. The results of this work are presented in the publication under authorship of Imali A. Mudunkotuwa, John M. Pettibone and Vicki H. Grassian, *Environmental Science and Technology*, 2012, 46, 7001-7010.

CHAPTER 5

DISSOLUTION OF ZnO NANOPARTICLES AT CIRCUMNEUTRAL pH: A STUDY OF SIZE EFFECTS IN THE ABSENCE AND THE PRESENCE OF LIGANDS

5.1 Abstract

Understanding size-dependent processes, including dissolution, of engineered nanoparticles is essential in addressing the potential environmental and health impacts of these materials as well as their long-term stability. In this study, experimental measurements of size-dependent dissolution of well-characterized zinc oxide (ZnO) nanoparticles with particle diameters in the range of 4 to 130 nm have been measured at circumneutral pH (pH 7.5) and compared. Dissolution was found to be enhanced with smaller ZnO nanoparticles compared to larger-sized particles, even though the nanoparticles were present in solution as aggregates with hydrodynamic diameters on the order of 1 – 3 μm in size. Although these results are found to be in qualitative agreement with theoretical predictions, a linearized form of the Kelvin equation to calculate a surface free energy yielded quantities inconsistent with expected values from the literature. Reasons for this inconsistency are discussed and include potential deviations of solubility behavior from classical thermodynamics as a result of a lack of detailed knowledge of surface structure and surface properties, including the presence of different surface crystal facets, and the aggregation state. The effect of environmental and biological ligands on this size dependent behavior was probed using citric acid and bovine serum albumin (BSA). The presence of citric acid, significantly enhanced the extent of ZnO dissolution for all sizes, and the greatest enhancement was observed for the 4 nm particles. However bovine serum album (BSA) did not promote solubility and therefore the size dependent dissolution was in fact preserved in its presence.

5.2 Introduction

Although materials with nanoscale dimensions have been present for some time, nanomaterials have attracted even more attention recently because they now can be synthesized with great control, and they show distinct size-dependent properties.[16,194] As a result, a large number of materials having nanoscale dimensions are being used in different applications because of their unique electronic, thermal, optical, and photoactive properties in the fields of information technology, electronics, catalysis, medicine, and energy.[49,105,115,195,196]

One key aspect of nanoscience is the ability to tune the properties of matter via the control of size and shape.[48,51,116,117,197] For example, it has been clearly demonstrated in a number of studies that electronic properties exhibit size-dependent behavior.[48,51] Additionally, magnetic properties of transition metals have shown significant variations with size when materials are in the nanoscale size regime.[48] Theoretical calculations have shown that the surface charge density of nanomaterials are highly size dependent whereby a considerable increase in surface charge density is predicted for particles smaller than 10 nm.[116] Chemical reactivity and catalytic activity of nanomaterials also depend on size where smaller nanomaterials are often more active and show enhanced selectivity compared to their larger counterparts.[48,74] Interestingly, in some cases, there are specific nanoparticle sizes that are highly selective and more active relative to other sizes (larger or small).[198,199]

Size-dependent dissolution of nanomaterials is an area of great interest due to the importance of dissolution in industries such as pharmaceuticals, cosmetics, agrochemical, paints and coating.[200,201] Significant increases in solubility with decreasing particle size have been observed in the literature.[74,105,200,202] Pharmaceutical drugs composed of nanoscale particles are considered an important formulation route for oral administration of drugs with poor dissolution properties.[200] Dissolution of materials has been long studied where an enhanced rate of dissolution of finely divided solids compared to large crystals has been observed.[54,203] Increased surface area is one important reason for increased kinetic rates of dissolution. Furthermore, it is now becoming clear that the dissolution of engineered nanomaterials is extremely important in terms of stability of these materials as well as the environmental and health impacts that these particles may have if released into the environment.[24]

Dissolution of nanoparticles in aqueous systems, especially for metal-based nanomaterials, is a concern because these metals can give rise to toxic effects.[87] Since the properties of nanoscale materials differ markedly from the bulk, variations in toxicity effects may be related to the dissolution properties of nanomaterials relative to micrometer-sized particles of these materials.[85] For small particles, several theoretical models and approaches have been put forth to describe the size-dependent dissolution of materials beyond surface area effects.[201,204] However, large discrepancies exist among these theoretical studies and experimental measurements in addition to only a limited number of investigations being available on well-characterized nanomaterials to describe this phenomenon. [106-108]

ZnO is of particular interest as it is widely used in a number of consumer products such as sunscreens, cosmetics, dye-sensitized cells, plastic additives, and electronics due to their distinct thermal, electronic, and optical properties.[61,194,195,205-208] Thus occupational, incidental, and direct exposure via consumption can be given as the most likely routes of exposure to ZnO nanomaterials. Despite the general conviction of ZnO as a biologically safe material, recent research continues to highlight potential biological toxicities of nanoscale ZnO.[27,209] A study by Brayner *et al.* on biocidal effects and cellular internalization of nanoscale ZnO in Escherichia coli bacteria has shown membrane disorganization resulting in increased permeability and consequent accumulation of ZnO nanoparticles in the bacterial membrane.[194] A comparison study of TiO_2, SiO_2 and ZnO toxicity toward *Bacillus subtilis* and *E. coli* by Adams *et al.* has determined ZnO to be the most toxic.[210] Often a criticism of these studies is the lack of differentiation between the effects of dissolved Zn^{2+} ions and the actual nanoparticles, as it is thought that the mechanisms of toxicity are most likely different in each case. Thus Lin *et al*. attempted to distinguish between such effects with *Lolium perenne* (ryegrass), which showed significant reduction in its biomass even below the toxicity threshold of Zn^{2+}, suggesting potential ZnO nanoparticle toxicity.[70] In addition, Heinlaan *et al.* showed that ZnO nanoparticles with LC_{50} (mg L^{-1}) values of 1.9, 3.2, and 0.18 differed from $ZnSO_4$. $7H_2O$ LC_{50} (mg L^{-1}) values of 1.1, 6.1, and 0.98 for *Vibrio fischeri*, *Daphnia magna*, and *Thamnocephalus platyurus*, respectively.[38] Xia *et al.* studied the cellular response of macrophage and epithelial cell lines toward ZnO nanoparticles, which indicated particle dissolution and release of Zn^{2+} playing a key role in inducing toxic effects.[33] Furthermore they observed a size reduction in ZnO agglomerates from 413 to 36 nm when transferred from the water to cell culture medium facilitating nanoparticle uptake and subsequent intracellular dissolution. By contrast, Raghupathi *et al*. observed size-dependent growth inhibition in various microorganisms including *E. coli* and *Staphylococcus aureus* with ZnO nanoparticle suspensions, which was not observed when the suspension supernatant was used.[97] According to this study, toxic effects arise from ZnO nanoparticles and not the dissolved Zn^{2+} ions. Poynton *et al*. used gene expression profiling of *Daphnia magna* to show distinct modes of toxicity between ZnO nanoparticles and $ZnSO_4$.[211] Li *et al*. highlighted the effect of water chemistry in dictating the toxicity profile of ZnO nanoparticles.[212]

Although many controversies still exist on the origin of these toxicities, the generation of reactive oxygen species (ROS), creation of protein corona encapsulating the nanoparticles (depending on size, curvature, shape and surface features) leading to protein unfolding, fibrillation, thiol cross-linking, and loss of enzymatic activity are all considered to trigger the actual "effects".[33] The debate in the scientific community continues in determining exact mechanisms that give rise to the toxicity of nanoscale ZnO. Therefore, a fundamental understanding on size-dependent dissolution of nanoscale ZnO becomes crucial from environmental and toxicological perspectives. In the current study, the size-dependent dissolution of ZnO has been investigated using well-characterized nanoparticles in the presence and absence of citric acid and bovine serum albumin, abundant coordinating ligands of environmental and biological significance, to better understand the dissolution of ZnO on the nanoscale.

5.3 Experimental Methods

5.3.1 Nanoparticle Characterization

Nanoparticles were characterized with different techniques including transmission electron microscopy (TEM), powder X-ray diffraction (XRD), Brunauer EmmettTeller (BET) surface area analysis, and attenuated total reflectance Fourier transform infrared (ATR-FTIR) spectroscopy. Diffraction patterns were collected using a Rigaku Miniflex II diffractometer with a Co source. TEM images of the samples were collected using TEM, JEM JEOL-1220. The specific surface area of the particles was measured using seven-point N_2 BET adsorption isotherm measurements using a Quantachrome Nova 4200e surface area analyzer. Numerical values are reported as the average of triplicate measurements. ATR-FTIR spectroscopy measurements were obtained to investigate the surface functional groups present on ZnO nanoparticles. Measurements were obtained using an AMTIR crystal element in a horizontal ATR cell (Pike Technology, Inc.). A thin film of ZnO was prepared by depositing a ZnO suspension (1.5 mg in 1.0 mL of ethanol) onto the AMTIR crystal and drying overnight. ATR-FTIR spectra of the thin films of nanoparticles were recorded.

5.3.2 Quantitative Dissolution Measurements.

Dissolution studies were conducted using a Varian inductively coupled plasma optical emission spectrophotometer (ICP-OES) at room temperature (~25 C) at pH 7.5. The experiments were conducted according to the following protocol. The dissolution of

ZnO at pH 7.5 was studied using seven samples of sizes 4, 7, 15, 17, 24, 47, and 130 nm with a ZnO solid loading of 0.5 g/L. ZnO and HEPES buffer (pH 7.5, 10 mL) were mixed, covered with aluminum foil to inhibit any photoinduced dissolution, and placed on a Cole-Parmer circular rotator for 24 h. After completion of mixing the suspension pH was measured. Previous methods that were used to separate TiO_2 nanoparticles (4 nm) from solution by filtration (0.2 μm, Xpertec filters) and centrifugation (22000 rpm for 30 min) was not suitable for ZnO nanoparticles, as they dissolve to form even smaller particles that get through the filters as seen by the TEM images of the supernatant. Therefore a different method was employed whereby dissolved Zn^{2+} was separated from the ZnO nanoparticles in the solution using Amicon Ultra-4 centrifugal filter units with pore diameters of 1.2 nm (Amicon Ultracel 3K, Millipore, USA). Aliquots (~2 mL each 3) were transferred into filter units and centrifuged at 7500 rpm for 30 min. The filtrate collected was analyzed using ICP-OES to quantify the dissolved zinc. To confirm the absence of smaller ZnO nanoparticles, filtered solutions were imaged using TEM, and UV/visible (UV/vis) absorbance spectra (in the range of 250 – 400 nm[45]) were collected. No particles were observed in the micrographs, and no distinct peaks observed in the UV/vis spectra. These centrifuged samples were diluted to 5 mL with 1 M HCl prior to analysis, and the calibration was conducted with 5.0, 10.0, 25.0, and 50.0 ppm Zn^{2+} standards prepared in 1 M HCl. The average and standard deviation of triplicate measures are reported for all dissolution measurements.

Dissolution rates of ZnO nanoparticles of different sizes were investigated in a kinetic study using 4, 7, and 15 nm ZnO samples. The above procedure was followed with aliquots of the sample being drawn at time intervals of 15 min for the first 4 h and then 1 h intervals for 24 h. These data showed that the dissolution of ZnO nanoparticles at this pH had reached steady state in 24 h.

5.3.3 Aggregation Measurements.

Because of the propensity of nanoparticles to aggregate and the impact that aggregation may have on dissolution, the aggregation behavior of ZnO particle suspensions was examined. Size distributions of the aggregates were obtained using a dynamic light scattering (DLS) instrument (Delsa Nano C particle analyzer) equipped with a green laser at 532 nm. Suspensions were prepared at 0.5 g/L solid loading of ZnO at filtered pH 7.5 buffer and allowed to sit overnight to ensure steady state aggregation.

5.3.4 Sources of Nanomaterials and Chemicals.

Six laboratory-synthesized samples and a commercially manufactured sample of ZnO nanoparticles were used in this study. The detailed synthesis of ZnO powdered materials can be found in the work of Bian *et al*. for the 4 nm diameter ZnO and in that of Wu *et al.* for 7, 17, 24, 47, and 130 nm diameter ZnO samples (see Table 1).[74,213] The commercial sample of 15 nm diameter was purchased from Alfa Aesar. Solutions at pH 7.5 were prepared with 4-(2-hydroxyehtyl)-piparazeneethanesulfonic acid (HEPES; Sigma Aldrich; ≥ 99%). To adjust the pH of the solution to 7.50 ± 0.01, sodium hydroxide (NaOH; Fisher Scientific; certified ACS plus) was used, and solutions were prepared using optima water (Fisher Scientific).

5.4 Results and Discussions

5.4.1 Nanoparticle Characterization.

A summary of the characterization data for ZnO nanoparticles used in this study is given in Table 5.1. These data include average particle diameters determined with TEM along with a standard deviation for these diameters as measured from the analysis of over 100 particles along with calculated and measured BET surface areas (average value of triplicate measurements and standard deviation reported). For smaller nanoparticles (≤15 nm), the measured surface area was significantly lower than the expected calculated value.

Table 5.1: Single particle diameter (d) and BET surface area of ZnO Nanoparticles[a].

Diameter (d) nm	**Calculated surface area[b]** m^2/g	**BET surface area – measured** m^2/g
4 ± 2	268 ± 134	105 ± 13
7 ± 2	153 ± 44	75 ± 4
15 ± 4	71 ± 19	47 ± 1
17 ± 3	63 ± 11	50 ± 3
24 ± 3	45 ± 6	40 ± 2
47 ± 7	23 ± 3	26 ± 1
130 ± 21	8 ± 1	11 ± 1

[a] All ZnO nanoparticles were synthesized from zinc acetate except for the 15 nm sample, which was a commercially purchased sample. [b] Calculated surface area = $6/(d.\rho)$ where d = diameter and ρ = density.

This difference can be attributed to aggregation of nanoparticles that has the potential to inhibit surface adsorption leading to an overall lower surface area. TEM images of the ZnO nanoparticles and the XRD data are shown in Figure 5.1. XRD data show that these samples are crystalline and confirm the expected wurtzite crystal structure for these ZnO nanoparticles. XRD peaks also showed the expected line broadening for smaller nanocrystallite size. Figure 5.2 illustrates the surface functional groups for these different samples determined from ATR-FTIR spectroscopy. The spectra for 7 nm sample is representative to that of 17, 24, 47 and 130 nm ZnO nanoparticles since they are all synthesized using the same precursor medium. Surface adsorbed acetate groups, which originate from the zinc acetate precursor used in the synthesis, can be seen in the surface spectra of 4 and 7 nm ZnO nanoparticles. Absorption bands present at 1400 and

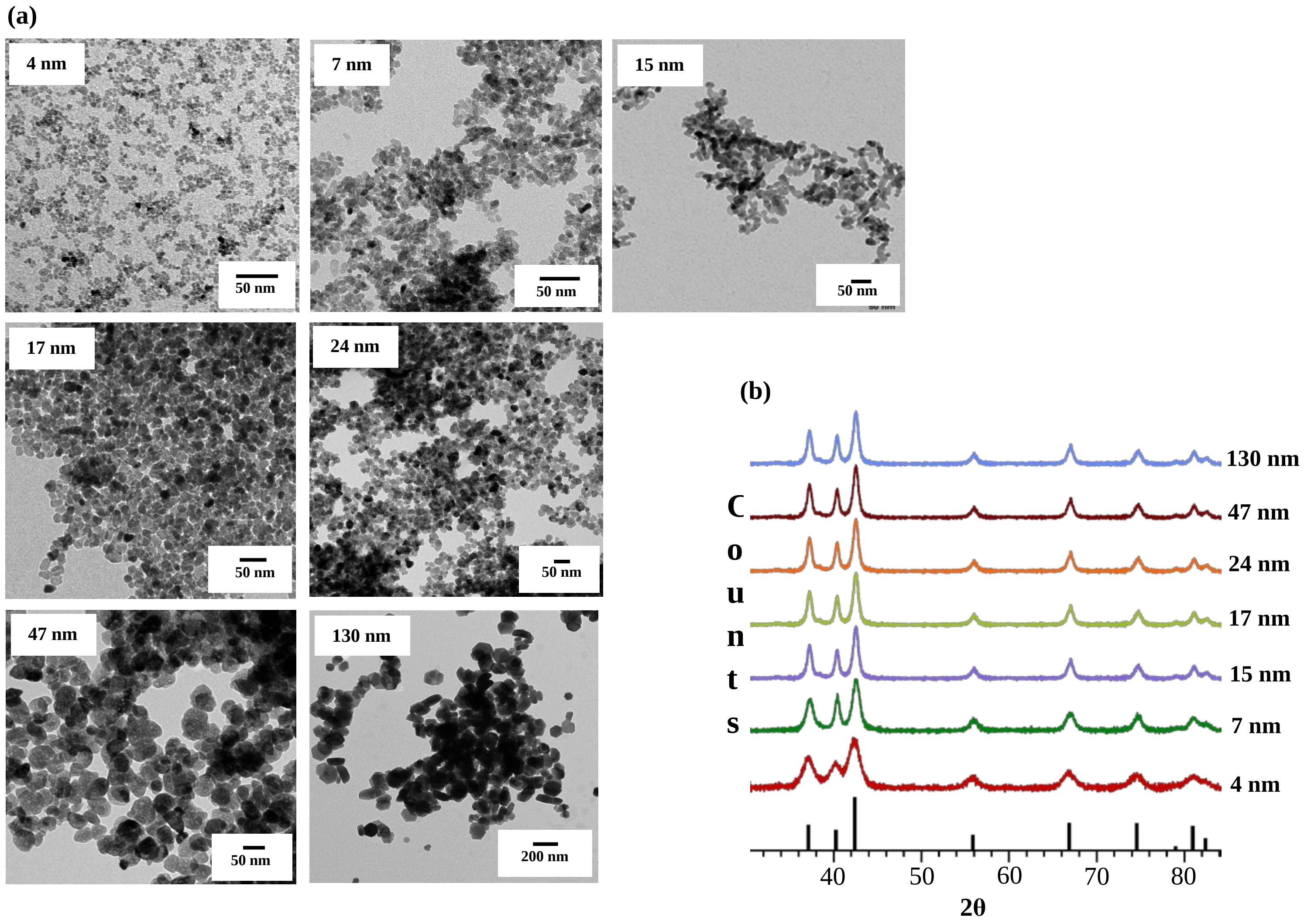

Figure 5.1: Nanoparticle characterization (a) TEM images of ZnO nanoparticles with diameters. The scale bar is the same 50 nm in each image except for the last image (200 nm). (b) Corresponding XRD patterns of the ZnO nanoparticles.

1565 cm^{-1} in the 4 nm ZnO spectrum can be assigned to the symmetric and asymmetric stretching modes of the carboxylate group, COO$^-$.[144] Two peaks appear in the 7 nm spectrum at 1400 and 1574 cm^{-1}, which are also assigned to the symmetric and asymmetric stretching modes of COO$^-$, respectively. In comparison, the spectrum of the 15 nm ZnO sample (commercial sample) has absorptions that are centered near 1389 and 1500 cm^{-1}. The frequencies of these vibrational bands are more closely associated with adsorbed carbonate groups.[214] During the dissolution process, these adsorbed acetate and carbonate groups will be removed from the surface.

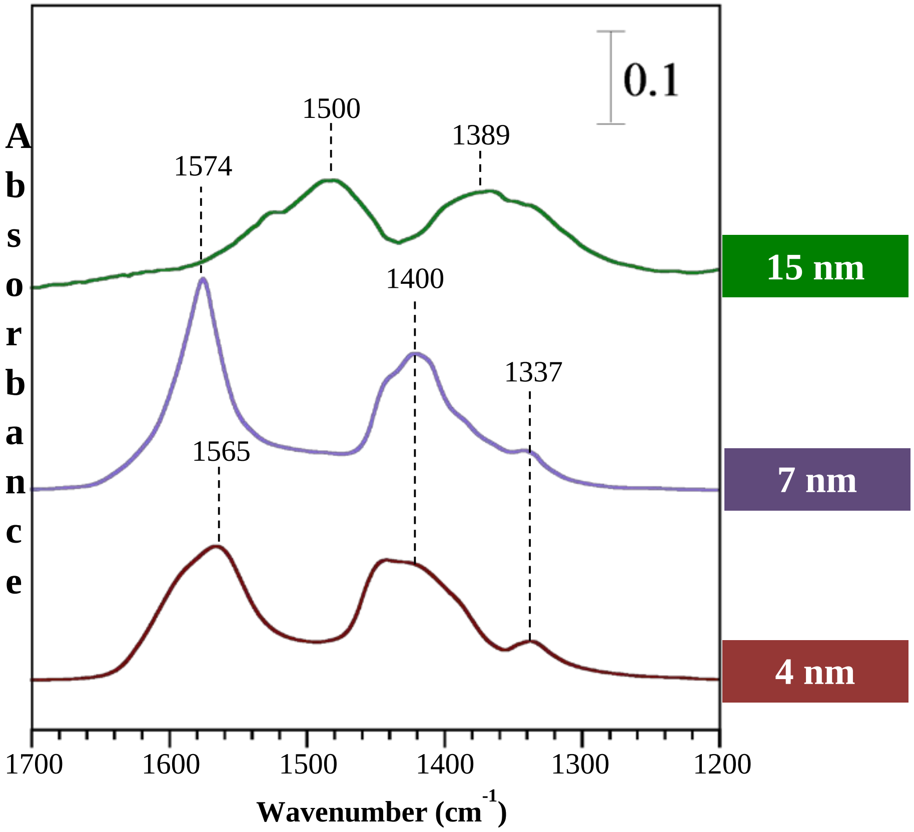

Figure 5.2: ATR-FTIR spectra for 4, 7 and 15 nm ZnO nanoparticles. The 4 and 7 nm samples were laboratory synthesized from zinc acetate precursor, whereas the 15 nm sample was purchased from Alfa Aesar.

Hydrodynamic diameters of ZnO aggregates were measured in solution at pH 7.5 with DLS. The results from these measurements are given in Table 5.2. As can be seen, the hydrodynamic diameters for all of the ZnO samples are considerably larger than their primary particle sizes as measured with TEM. Aggregates present in the solution are in the range of 2 – 3μm.

Table 5.2: Hydrodynamic diameters of ZnO nanoparticle aggregates at pH 7.5 after 24 hour equilibration.

Single particle diameter (d) (nm)	**Hydrodynamic diameter (μm)**
4 ± 2	3 ± 0.3
7 ± 2	2 ± 0.1
15 ± 4	3 ± 0.1
17 ± 3	2 ± 0.1
24 ± 3	2 ±0.1
47 ± 7	3 ± 0.4
130 ± 21	2 ± 0.3

5.4.2 Aqueous Phase Behavior in the Presence and Absence of Organic Acids.

Dissolution of ZnO nanoparticles was measured for six laboratory synthesized ZnO samples and one commercial sample at pH 7.5. Dissolution measurements were done after 24 h. From the results of kinetic measurements, the amount of dissolved Zn^{2+} reaches steady state within a ca. 6 h time period, so the 24 h measurement insures equilibrium in these systems. The final pH values of the solutions were increased slightly and raised to values ranging from 7.7 to 7.8. The data for measurements of Zn^{2+} concentrations show the greatest extent of dissolution for 4 nm nanoparticles, as shown in Table 5.3 and Figure 5.3. The overall trend shows a decrease in the extent of dissolution with increasing particle size. When normalized to the surface area of the nanoparticles, the dissolution ranged from 2.0 x 10^{14} to 6.0 x 10^{14} Zn^{2+} cm^{-2} for all samples corresponding to the dissolution of the surface monolayer. The highest value of 6.0 x 10^{14} was reported for 130 nm ZnO nanoparticles with the lowest surface area.

Table 5.3: Quantitative measurements of [Zn^{2+}] and pH along with calculated solubility products (K_{sp}) for ZnO nanoparticles.

Diameter (nm)	[Zn^{2+}] (mg/L)	pH	K_{sp} (mol/L)^3
4 ± 2	14.9 ± 0.3	7.7 ± 0.01	$(6.0 \pm 2.0)x10^{-17}$
7 ± 2	7.6 ± 0.1	7.7 ± 0.01	$(3.4 \pm 0.4)x10^{-17}$
15 ± 4	4.9 ± 0.1	7.8 ± 0.01	$(2.5 \pm 0.3)x10^{-17}$
17 ± 3	5.6 ± 0.1	7.7 ± 0.01	$(2.5 \pm 0.2)x10^{-17}$
24 ± 3	4.8 ± 0.1	7.8 ± 0.02	$(2.6 \pm 0.4)x10^{-17}$
47 ± 7	4.4 ± 0.1	7.8 ± 0.02	$(2.2 \pm 0.2)x10^{-17}$
130 ± 21	3.4 ± 0.1	7.8 ± 0.01	$(1.9 \pm 0.9)x10^{-17}$

Thus, size-dependent dissolution was clearly observed even in the presence of aggregation for ZnO nanoparticles at circumneutral pH in this relatively simple matrix. The

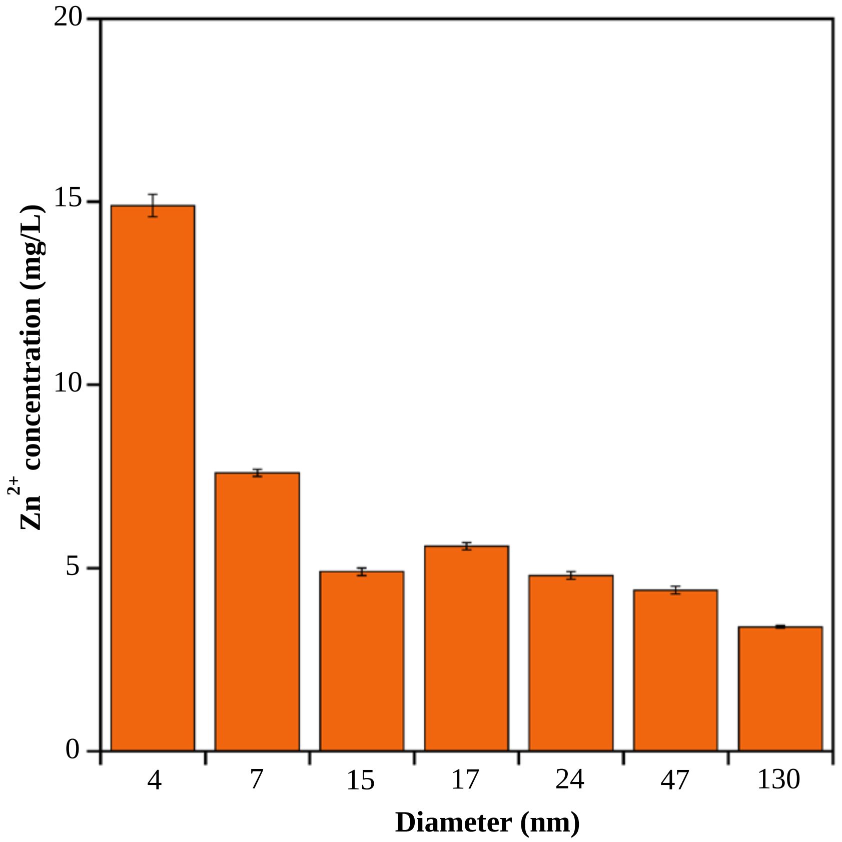

Figure 5.3: Measured Zn^{2+} concentrations after 24 h from aqueous suspensions of ZnO nanoparticles (0.5 g/L) of different size at an initial pH of 7.5.

dissolution process increases substantially upon addition of citric acid with 4 nm ZnO nanoparticles showing even a greater extent (Figure 5.4a). The enhanced dissolution of 4 nm particles results from the large surface area, and, when normalized to the BET surface area, all the samples showed similar dissolution in the range of 1.3×10^{15} to 8.0×10^{15} Zn^{2+} cm^{-2} corresponding to the dissolution of first two surface layers. Citric acid with its three carboxylate groups is an excellent complexing ligand.[168] It forms very stable bidentate complexes with Zn^{2+} ions in the solution that has a stability constant of log K= 4.9 at circumneutral pH.[215] The following reactions show the initial hydroxylation of the ZnO nanoparticle surface (Eq: 5.1), the surface adsorption of aqueous citric acid via ligand exchange mechanism (Eq: 5.2), followed by the subsequent dissolution of the surface as a result of polarized and weakened metal oxygen bonds (Eq: 5.3).

$$\equiv ZnO_{(s)} + H_2O_{(l)} \rightleftharpoons \ \equiv Zn(OH)_{2\,(s)} \qquad (Eq{:}\,5.1)$$

$$\equiv Zn(OH)_{2\,(s)} + citrate^{3-}{}_{(aq)} \rightleftharpoons \ \equiv Zn(citrate)^{-}{}_{(ads)} + 2OH^{-}{}_{(aq)} \qquad (Eq{:}\,5.2)$$

$$\equiv Zn(citrate)^{-}{}_{(ads)} \rightleftharpoons \ \equiv Zn(citrate)^{-}{}_{(ads)} \qquad (Eq{:}\,5.3)$$

The presence of citric acid clearly affected the dissolution process as can be seen by the increasing dissolution as a function of citric acid concentration (Figure 5.4b). Using 50 mM concentration to ensure that dissolution is not limited by available citric acid, the dissolution experiments of ZnO were conducted for 4, 7, 15, 17, 24, 47, and 130 nm samples, which showed no dependence on size when normalized to the BET surface area.

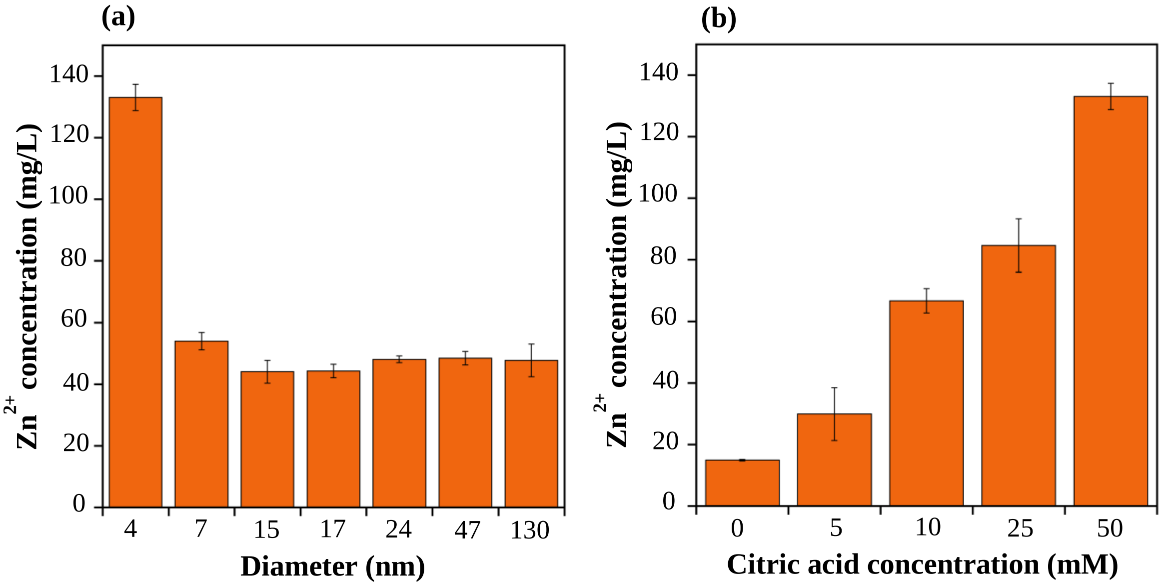

Figure 5.4: Dissolution of ZnO in the presence of citric acid after 24 h. (a) ZnO dissolution as a function of size at 50 mM citric acid concentration. (b) ZnO dissolution as a function of citric acid concentration for 4 nm ZnO.

This contradicting observation obtained from the matrices with different complexities highlight several important points. First, size-dependent dissolution is evident for ZnO nanoparticles, as shown in Figure 5.3. As the size of the particles decrease surface area and the number of edges, kinks and defect site density increase creating “hot spots” of dissolution. Thus, enhanced dissolution properties are observed for smaller particles. Second, when complexing ligands are present in the medium, these can adsorb on to the majority of flat terraces as well polarizing and weakening the metal-oxygen bonds of the lattice surface.[168] Thus in the presence of such ligands, additional dissolution hot spots are created on the terraces other than the edges and kinks, leading to the same extent of dissolution for both nanoscale and bulk materials, potentially explaining the decrease in the lack of size dependent behavior (Figure 5.4a). Additionally, other products form in solution that can control the reaction chemistry. Bovine serum albumin (BSA) on the other hand only slightly increased the dissolution at the very small scale. (Figure 5.5).

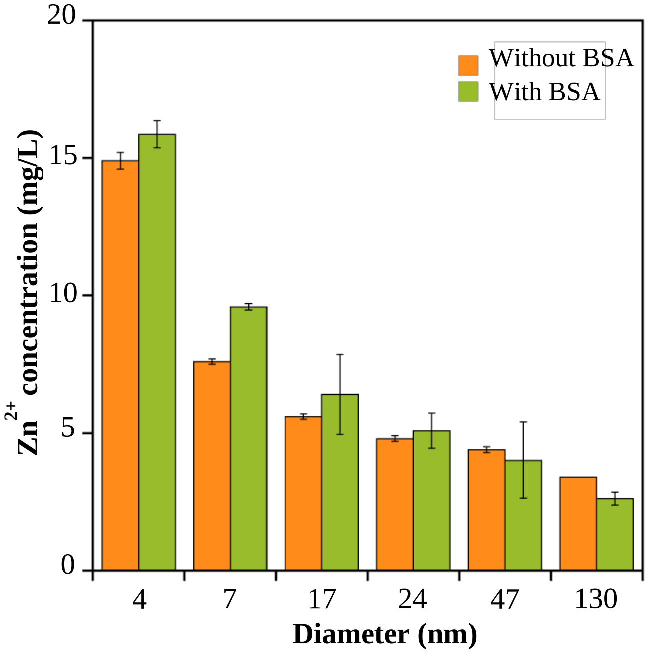

Figure 5.5: Dissolution of 4 nm ZnO in the presence of bovine serum albumin (1 g/L) after 24 h.

BSA being a plasma protein can potentially form proton coronas which can encapsulate the nanoparticles and prevent dissolution. The objective of using these ligands in the current study was to investigate the effect that environmentally and biologically relevant, common, complexing ligands have on size-dependent dissolution.

5.4.3 Surface Energy of ZnO Nanoparticles in Solution.

Zinc oxide dissolution is well-known and occurs over a wide range of pHs.[74] At circumneutral pH of 7.5, the dissolution of zinc oxide is limited, and thus this is a good pH to investigate size-dependent behavior due to the fact that there is minimal interference from products that can form and a change in pH that occurs when large quantities dissolve. For ZnO, the following reactions are important in water at pH 7.5:[216,217]

$$ZnO_{(s)} + H_2O_{(l)} \rightleftharpoons Zn(OH)_{2\,(s)} \qquad (Eq: 5.4)$$

$$Zn(OH)_{2\,(s)} \rightleftharpoons Zn(OH)^{+}{}_{(aq)} + OH^{-}{}_{(aq)} \qquad (Eq: 5.5)$$

$$Zn(OH)^{+}{}_{(aq)} \rightleftharpoons Zn^{2+}{}_{(aq)} + OH^{-}{}_{(aq)} \qquad (Eq: 5.6)$$

Overall, the net reaction for the dissolution of ZnO is as follows:

$$ZnO_{(s)} + H_2O_{(l)} \rightleftharpoons Zn^{2+}{}_{(aq)} + 2OH^{-}{}_{(aq)} \qquad (Eq: 5.7)$$

In the current study, the solubility product constant, K_{sp}, for the samples was calculated using the Zn^{2+} concentration obtained from ICP-OES analysis and the OH concentrations obtained via measuring the solution pH both after 24 h. The solubility, S, of ZnO is then related to K_{sp} according to eq 8:

$$S = \left[\frac{K_{sp}}{4}\right]^{1/3} \qquad (Eq: 5.8)$$

Measured Zn^{2+} concentrations, equilibrium solution pH, and calculated K_{sp} for all seven ZnO samples are given in Table 5.3. Measured Zn^{2+} concentrations show that ZnO nanoparticles dissolve at pH 7.5 and the extent of dissolution increases with decreasing particle size. The data presented in Figure 5.3 indicate larger concentrations of Zn^{2+} and thus enhanced dissolution for the smaller ZnO nanoparticles compared to larger particles.

The above observations can be attributed to the higher surface free energy and activity of nanoparticles due to their small size in addition to the increased surface area. The relationship between particle size and solubility can be described using a modified Kelvin equation, which is typically used to describe the change in vapor pressure due to a curved liquid-vapor interface, and is also known as the Ostwald-Friedrich equation (eq 9).[105,201,204]Accordingly, the solubility is expected to increase exponentially with decreasing particle size as follows:

$$\frac{S}{S_{bulk}} = exp\left[\frac{4\gamma V}{RTd}\right] \qquad (Eq: 5.9)$$

where S is the solubility (in mol/kg) of a spherical particle with diameter d (m), S_{bulk} is the solubility of the bulk, γ is the surface free energy (in mJ/m^2), V is the molar volume (in m^3/mol), R is the gas constant (in mJ/mol K), and T is the temperature (in K). As size decreases, the surface energy of the particles is expected to increase, which results in enhanced dissolution.[105] This equation can be related to the solubility product constant and linearized to give

$$\ln K_{sp} = \ln K_{sp}^{bulk} + \frac{12\gamma V}{RTD} \qquad (Eq: 5.10)$$

As can be seen from eq 10, assuming a constant V and γ with varying size, a plot of $\ln K_{sp}$ versus d^{-1} can be used to deduce both the surface energy and the bulk solubility product constant of the ZnO nanoparticles. Using the solubility product constant values determined (see Table 5.3), ln K_{sp} versus d^{-1} for all seven ZnO samples in buffered solution is plotted, and the experimental results showed a linear trend in agreement with the theoretical prediction depicted by the linearized Kelvin equation (eq 10). The bulk solubility product constant ($1.9x10^{17}$ mol^3 /L^3) obtained from the intercept of the graph is comparable to the $1.7x10^{17}$ mol^3 /L^3) at 25°C stated in the literature.[53] Furthermore, the surface energy calculated using the slope of ln K_{sp} versus d^{-1} plot is determined to be 0.06±0.01 J/m^2.

Figure 5.6 compares the variation of ln$[K_{sp}/K_{sp}^{bulk}]$ versus d^{-1} with three different surface energies: γ = 1.31 J m^{-2} for hydrated gas-solid interface,[61] γ = 0.1- 0.5 J m^{-2} for metal oxides in solution,[207] and γ = 0.06 J m^{-2} from the best fit of data. The experimental data is quite lower than that predicted from specific values reported for the surface energy of ZnO nanoparticles (γ = 1.31 J m^{-2}) in particular.

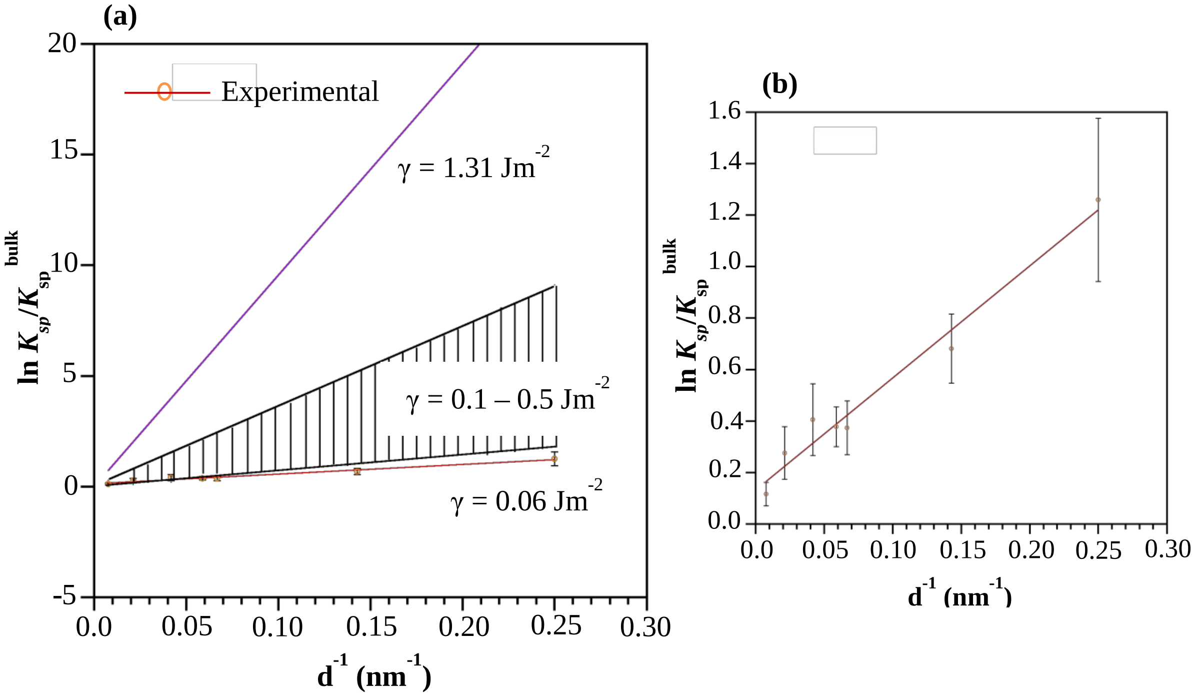

Figure 5.6: Surface energy of ZnO nanoparticles. (a) ln$[K_{sp}/K_{sp}^{bulk}]$ is plotted as a function of the inverse of particle diameter (d^{-1}). (b) The experimental data plotted on an expanded scale.

Zhang *et al.* have reported values of 1.31 and 2.55 J/m^2 for hydrous and anhydrous surfaces, respectively,[61] at the gas-solid interface, indicating the significant reduction of surface energy by surface adsorbed water. Therefore once in solution, adsorption of ions and solvent molecules reduce the surface energy to fall within the range of 0.1 - 0.5 J m^{-2}. However, in the current study, the experimental data of smaller nanoparticles (d< 10 nm) was clearly outside the range predicted, accounting for the reduction in surface energy by surface adsorbed species, indicating contribution from additional factors. A key factor can result from aggregation of nanoparticles in the solution, as can be seen by the large hydrodynamic diameters observed (Table 5.2). Additionally, the presence of surface adsorbed acetate groups for most of the nanoparticles investigated (Figure 5.2) could potentially contribute toward lowering the surface energy. It should also be noted that the calculated surface energy in this study, $\gamma = 0.06 \pm 0.01$ J m^{-2}, is an average of the surface crystal faces for a range of sizes. This average value may or may not be representative of all the planes that could result from the differences in prominent crystal faces for each size. Park *et al*. has shown that for three-dimensional assemblies of TiO_2, the average surface energy is closer to that of simple TiO_2 nanoparticle structures with (101) dominant surface planes, whereas ZnO tetrapods showed larger deviations in the average surface energy from the simple spherical nanoparticles.[62]

Apart from the differences in the actual experimental conditions and differences between the samples and synthesis procedures from those in literature, the theoretical model itself has some limitations that could result in an under- or overestimation of the surface energy. Although it has been assumed in the modified Kelvin equation that the nanoparticles are spherical, it is important to note that nanoparticles are not spheres and have distinct shapes and facets.[201,204]In addition, aggregation leads to the formation of several irregularly shaped structures such that the actual size of particles is uncertain. Aggregation has been shown to decrease the rate of dissolution and even completely quench the process in some cases.[102,105] It is postulated that effective, reactive surface area of the nanoparticles exposed to the solution is reduced due to aggregation, and the solution properties within the aggregates are different from the bulk. Although aggregation plays a significant role in nanoparticle dissolution, it is not accounted for in the modified Kelvin equation.[103,105] Furthermore, different surface energies have been successfully correlated with different morphologies of nanomaterials, which clearly indicates the dependence of surface energy on the exposed crystal planes.[61,62] ZnO nanoparticles with different sizes do not have the same number of edge and corner atoms.[108] Therefore, the surface-to-volume ratios can be different as well as the surface free energies. Additionally, most stable crystal planes of nanoparticles vary with size. The modified Kelvin equation does not account for these potential size dependencies of γ and also for its dependence on surface properties such as defects and different surface crystal facets.[105] It has been revealed from several research studies that one of the major problems associated with the modified Kelvin equation is the uncertainty as to whether the value of γ is constant for very small particles.[204,218]

On other studies of ZnO dissolution, Meulenkamp discussed size selective etching of ZnO nanoparticles by anhydrous acetic acid in ethanolic solution and showed that for a mixture of 3.15 and 4.30 nm ZnO nanoparticles, the former etches at a much faster rate.[202] However, based on particle size evolution during the etching process, it was clearly shown that particle size decrease is much smaller than predicted using a simple model of cube root dependence where all the surface particles detach at the same rate. However, the experimental particle size evolution was successfully simulated in a Monte Carlo process where size dependence and polydispersity had been accounted for. Dissolution measurements of single-crystal ZnO (0001) surfaces by in situ atomic force microscopy (AFM) imaging showed that for pH 5.5 - 3.8, the dissolution proceeds only along the pre-existing edges and not along the terraces.[219] This was successfully correlated to the positively charged surface at this pH for the (0001) terraces inhibiting the proton promoted dissolution in contrast to the other crystallographic planes (1120 or 1010) present at the edges. In another study on the dissolution of PbS nanocrystals, greater dissolution for (110) and (111) edges was exhibited over(100) primary terraces, as shown by the high-resolution TEM (HRTEM) images.[103] Furthermore, comparison of the dissolution rates of 14.4 nm PbS nanocrystals vs 3.1 μm nanocrystals gave 10 times greater rate for the former than the latter.[105] Little size dependence was observed by Peng *et al.* for ZnO nanoparticles in a more complex matrix (marine water) and with nanoparticles all greater than 6 nm in size.[206] All these studies highlight distinct dissolution behavior that depends on the size and topographical features at the nanoscale.

5.5 Conclusions and Implications

This current study has focused on understanding the size dependent dissolution of ZnO nanoparticles in the range of 4 – 130 nm at pH 7.5. A number of interesting and important conclusions about the dissolution of nanoparticles can be derived from this study of well-characterized particles. First, smaller nanoparticles show a greater extent of dissolution compared to larger particles as expected from classical theoretical predictions depicted by the modified Kelvin equation and size. Second, there are quantitative deviations from the modified Kelvin equation that can arise from the presence of surface functional groups: dependence of γ on exposed crystal planes and aggregation. Third, the theoretical model itself lacks detailed surface topographic parameters to achieve accurate quantitative predictions. Fourth, aggregation, which plays a significant role in the dissolution of nanoparticles can play a role in the dissolution process, and here it is shown that ZnO nanoparticles aggregated to larger micrometer particles under the conditions of these studies. However, aggregation did not completely mask the size dependent dissolution of ZnO. Finally, the particle size dependence of ZnO was not as prevalent in the presence of citric acid, which was attributed to ligand-promoted dissolution. Overall, this study provides a link between theoretical predictions and actual experimental observations of size-dependent dissolution of nanoparticles where only a few such studies are available in the literature.

Acknowledgment

The research described in this article has been funded wholly or in part by the Environmental Protection Agency through grant number EPA R83389101-0 to V.H.G. It has not been subjected to the Agency's required peer and policy review and therefore does not necessarily reflect the views of the Agency and no official endorsement should be inferred. The authors would like to thank Dr. Shaowei Bian and Chia-Ming Wu for synthesizing the ZnO nanoparticles. The results of this work are presented in the publication under authorship of Imali A. Mudunkotuwa, Thilini Rupasinghe, Chia-Ming Wu and Vicki H. Grassian, *Langmuir*, 2012, 28, 396-403.

CHAPTER 6

HISTIDINE ADSORPTION ON TiO_2 NANOPARTICLES: AN INTEGRATED SPECTROSCOPIC, THERMODYNAMIC AND MOLECULAR-BASED APPROACH TOWARDS UNDERSTANDING NANO-BIO INTERACTIONS

5.1 Abstract

Nanoparticles in biological media form dynamic entities as a result of competitive adsorption of proteins on nanoparticle surfaces called a protein corona. The protein affinity towards nanoparticle surfaces potentially depends on the constituent amino acid side chains which are on the protein exterior and thus exposed to the solution. Therefore, studying the adsorption of individual amino acids on nanoparticle surfaces can provide valuable insights into the overall evolution of nanoparticles in solution and the protein corona that forms. In the current study, the surface adsorption of L-histidine on TiO_2 nanoparticles with a diameter of 4 nm at pH 7.4 (physiological pH) is studied from both macroscopic and molecular perspectives. Quantitative adsorption measurements of histidine on 4 nm TiO_2 particles yield a maximum adsorption coverage of $6.2 \pm 0.3 \times 10^{13}$ molecules cm^{-2} at T=293K and pH 7.4. These quantitative adsorption measurements also yield values for the equilibrium constant and free energy of adsorption of $K = 4.3 \pm 0.5 \times 10^{2}$ L mol^{-1} and $\Delta G = -14.8 \pm 0.3$ kJ mol^{-1}, respectively. Detailed analysis of the adsorption between histidine and 4 nm TiO_2 nanoparticle surfaces with ATR-FTIR spectroscopy indicates both the imidazole side chain and the carboxylate group interacting with the nanoparticle surface. The adsorption results in no change in surface charge and thereby does not change nanoparticle-nanoparticle interactions or aggregation behavior of these 4 nm TiO_2 nanoparticles in aqueous solution.

6.2 Introduction

The field of nanoscience and nanotechnology continues to grow with superior materials being fabricated for a broad range of applications in industry, energy and health.[18,93,153,220] The inherent size-dependent chemical, mechanical, optical, electrical, magnetic, electro-optical and magneto-optical properties, that can be entirely different from their bulk counterparts, render these materials to be of great interest from many scientific and application-based perspectives.[51] The superior nature arises in part from the large contribution of the surface free energy to the total free energy as a result of the high surface-to-volume ratio of the constituent atoms in nanomaterials.[57] From a medical and diagnostic perspective, these materials are attractive candidates in reaching inaccessible targets (e.g. the brain) and interacting with cellular machinery.[89] Therefore with increased usage from both intentional and unintentional exposure to nanomaterials is inevitable.[13] Consequently, it is of vital importance that design of safer nanomaterials and safety assessment of existing materials are conducted in parallel to the development of applications.[221] Understanding the interactions at the nano-bio interface plays a key role in this process and in the long run towards the sustainable development of nanoscience and nanotechnology.[88]

The formation of a “protein corona” is well established in the literature for nanoparticles in biological media which result from the competitive adsorption of proteins on nanoparticle surfaces.[92,222] This results in potential changes of interfacial properties and of aggregation state while altering the biological identity of the nanoparticles that affect their fate within the cells and tissues.[223,224] The protein corona is a dynamic entity where at the initial stage high abundance low affinity proteins bind to the primary nanoparticle surface which exchange over time with the low abundance high affinity proteins.[90,223,225] Both thermodynamic and kinetics of the protein adsorption at the surface contributes towards determining the final constituents of the corona. Therefore irrespective of the several thousand of proteins present in biological fluid, the protein corona is enriched with a significantly lower number, about 10-50 proteins, with the highest affinity proteins binding to nanoparticles at equilibrium.[80,223,226] In order to follow the evolution of the protein corona and to better understand the final state reached at equilibrium, an important focus that needs further attention is the interaction of individual amino acids at the nanoparticle surface. Protein affinities towards nanomaterials are dependent on the number of domains present that have attractive interactions with the nanoparticle surface.[227] These "domains" are specific portions of the protein that are rich in particular amino acids. For example, high molecular weight kininogen adsorbs onto iron oxide nanoparticles via domain 5 which is rich in histidine. Another aspect of importance is the hydrophobicity/hydrophilicity of the nanoparticle surface which is determined by the presence of polar functional groups (e.g., surface hydroxyl groups on oxide surfaces).[88] Based on this, surface interactions with biomolecules can vary significantly. Furthermore, amino acid side chains are responsible for stabilizing higher order secondary structures of proteins.[88] When specific domains interact with nanoparticles with high curvature, this can cause an unfolding or distortion of the protein secondary structure.[92,228,229] This can lead to the new catalytic sites that become exposed and/or the deformation of existing catalytic sites that may trigger undesirable biological responses. Since conformational changes in the proteins are typically irreversible even under conditions where the adsorption may be a reversible process, protein adsorption can affect physiological function of the protein even once it is desorbed or displaced back into solution.[230,231] Therefore, in order to better understand the adsorption of proteins and the impact that surface adsorption can have on protein structure, a comprehensive understanding of amino acid – nanoparticle interactions is required.[232,233]

TiO_2 nanoparticles are used heavily in cosmetics, construction materials, medical applications and energy storage devices.[15,151,153,234] In year 2010 the nanoscale TiO_2 production was estimated to be 5000 *t* and is expected to further increase.[234] Some of the above applications lead to direct exposure while engineered TiO_2 nanoparticles have been observed in urban run-off as well as in the atmosphere by Kaegi *et al.* and Zheng *et al.* respectively, which can result in indirect exposure.[44,45] Histidine on the other hand is an essential amino acid with a side chain pK_a which is close to the physiological pH, pK_{a2} 6.04. This enables ready exchange of protons with respect to small changes in the medium pH that affect the charged state of the side chain. Additionally the neutral imidazole ring of histidine can undergo tautomerization with ring flips (rotamerization) to interconvert between protonated and deprotonated forms with negligible changes in the space occupied by the ring which is generally important for protein function.[235] Furthermore, histidine is known to complex effectively with transition metal ions in the solution. These structural and chemical properties of histidine are utilized by biological systems and as a result it is found in a large number of metalloproteins, ion channels and enzyme active sites. It is also a precursor of histamine, a biogenic amine that triggers local immune responses.[236-238] As a result of this abundance, the potential of histidine and TiO_2 NPs interacting with each other in vivo can be significant. Although a large number of toxicological studies have been conducted to assess the safety of TiO_2 nanoparticles, fundamental information on how nanoscale TiO_2 interacts with biological molecules remains sparse especially under aqueous conditions. This knowledge is an absolute requirement in order to understand structure-function relationships which aid in improving their applications and safe design. Therefore, to obtain a comprehensive understanding of the adsorption processes at the nano-bio interface spectroscopic analysis was conducted using ATR-FTIR spectroscopy along with quantitative adsorption measurements to obtain the thermodynamic parameters on the histidine – TiO_2 NP model system. Additionally, nanoparticle aggregation was measured using dynamic light scattering techniques to analyze the impact of histidine adsorption on particle mobility. The findings of the current study are expected to contribute towards bridging the gap between protein corona evolution and interactions at the nano-bio interface in aqueous matrices. Furthermore, this information is also useful in biocompatible nanomaterial synthesis where amino acids are used to control size and morphology as well as stabilizing agents.[94,239,240]

6.3 Experimental Methods

6.3.1 ATR-FTIR Analysis of Solution Phase Adsorption.

Molecular level insights of histidine adsorption on TiO_2 nanoparticles were investigated using Attenuated Total Reflection-Fourier Transform Infrared Spectroscopy (ATR-FTIR). The following protocol was used to carry out the experiments. A suspension of TiO_2 NPs (1 mL of 1.5 mg/mL) was directly deposited on the horizontal AMTIR crystal and dried overnight. Once dried, the surface was covered with a flow cell (1 mL) connected to a peristaltic pump, flushed water (pH 7.4, ~1 mL/min) over to eliminate loosely bound particles and the background spectrum was collected. A solution of histidine (0.5 mM at pH 7.4) was then introduced in the flow system and single beam ATR-FTIR spectra were collected as a function of time at 4 cm^{-1} resolution for 30 hours. Each single beam spectrum was referenced to the background water spectrum to obtain the absorbance. At these histidine concentrations no solution phase histidine contributes towards the spectral intensity for the adsorbed species. The side chain contributions of histidine in solution phase are identified by comparing with the spectra of glycine. In order to distinguish between the different vibrational modes solution phase spectra was collected as a function of pH. Furthermore, to identify possible formation of peptide bonds adsorption of his-gly peptide on TiO_2 NPs was investigated as well. The extent of reversible adsorption was investigated by running water (pH 7.4) for 1 hour after the adsorption experiments. All experiments were conducted in triplicate.

6.3.2 HPLC Analysis of Solution Phase Adsorption.

Quantitative adsorption studies of histidine on TiO_2 nanoparticles were conducted according to Pettibone *et al.* with slight modifications.[148] Briefly, TiO_2 nanoparticles (2 mg/mL) were added to a series of histidine solutions (0.01 – 8.0 mM) and mixed for 24 hours to achieve the adsorption equilibrium. From the supernatant aliquots (1 mL) were withdrawn, filtered (Xpertec, 2 μm pore), centrifuged at 22000 rpm for 30 minutes to remove any unfiltered particles and was analyzed for remaining histidine using HPLC (Dionex Ultimate 3000) equipped with a uv-vis detector (λ = 210 nm). The mobile phase consisted of 40 mM Na_2SO_4 (pH 2.65 adjusted with methane sulfonic acid). The adsorbed histidine was calculated by difference between the initial and final solution phase concentrations. Experiments were conducted as a function of temperature (293, 298, 303, 310 and 320 (±0.5) K) to get additional thermodynamic data. In order to investigate the role of ionic strength, quantitative histidine adsorption measurements were also conducted as a function of ionic strength at 1 mM histidine. All experiments were conducted in triplicates.

6.3.3 Dynamic Light Scattering Aggregation Measurements.

The aggregation behavior of TiO_2 nanoparticles in the presence of histidine was investigated using a Beckman Coulter Delsa Nano submicron Particle Analyzer. The hydrodynamic diameter and the zeta potential of TiO_2 NPs (0.01 g/L) at pH 7.4 were measured in the presence of increasing concentrations of histidine (0, 0.01, 0.1, 1.0 and 5.0 mM). TiO_2 NPs stock solution (1 g/L) was sonicated (40% amplitude, 30 sec) to form uniform suspensions and aliquots (50 μL) were added to the histidine solutions (5 mL)

6.3.4 Sources of Nanomaterials and Chemicals.

All experiments conducted used TiO_2 nanoparticles purchased from Nanostructured and Amorphous Materials Inc. (Houston, TX). These were extensively characterized previously and gave a particle size distribution of 4 nm, BET surface area of 219±3 m^2/g and consisted of 100% anatase phase. L-Histidine (Sigma Aldrich 99.5% certified ACS plus) solutions were prepared using Optima water (Fisher Scientific). The pH was adjusted using NaOH (0.08 M, Fisher Scientific ACS plus) solution. The ionic strength studies were conducted in NaCl solutions (Sigma Aldrich 99.5% certified ACS plus).

6.4 Results and Discussions

6.4.1 Analysis of Solution Phase Histidine ATR-FTIR Spectra under Physiological pH.

Histidine consists of an imidazole ring, amine (NH_2) and a carboxylic group (COOH). The increased structural complexity of the side chain (consisting of an imidazole ring) results in the broad spectral bands when compared to simple amino acids such as glycine. Figure 6.1 compares the ATR-FTIR spectra of solution phase amino acids glycine and histidine at pH 7.4 which give a clear illustration of this fact.

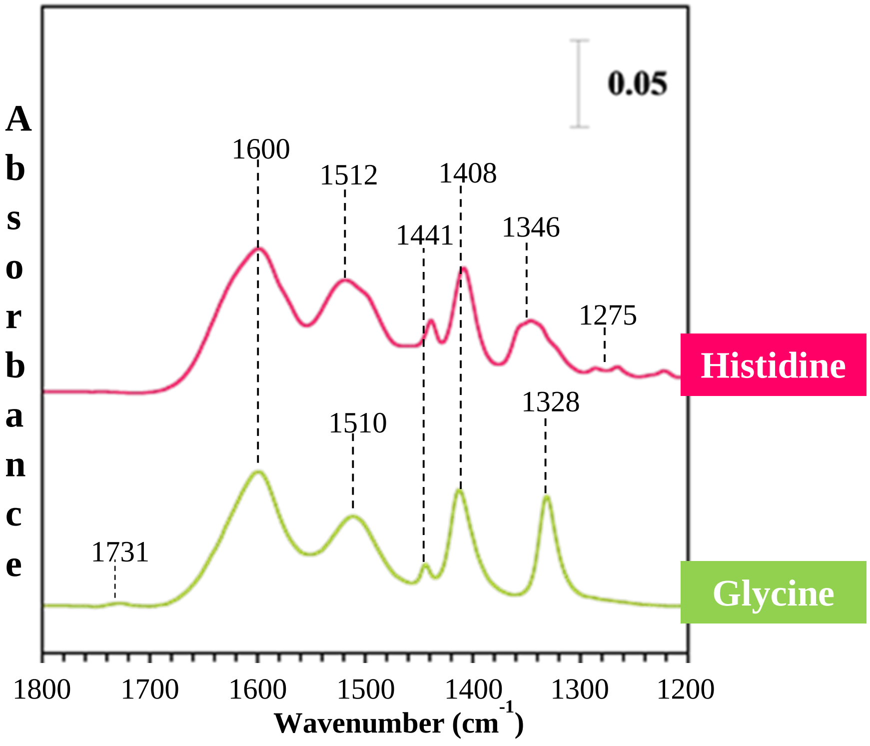

Figure 6.1: ATR-FTIR spectra of solution phase histidine and glycine at pH 7.4

For glycine the peaks at 1600, 1510, 1441, 1408 and 1328 cm^{-1} correspond to $\nu_{as}(COO^-)$, $\delta(NH_3^+)$, $\delta_{sc}(CH_2)$, $\nu_s(COO^-)$ and $\gamma(CH_2)$.[241,242] Thus this comparison allows identifying that the broad bands in histidine spectra around 1600, 1512, 1346 and 1275 cm^{-1} are due to the side chain CH_2 group and imidazole vibrations.[241] Furthermore, as shown in Figure 6.2, in histidine all three functional groups' protonation state is sensitive to solution pH.

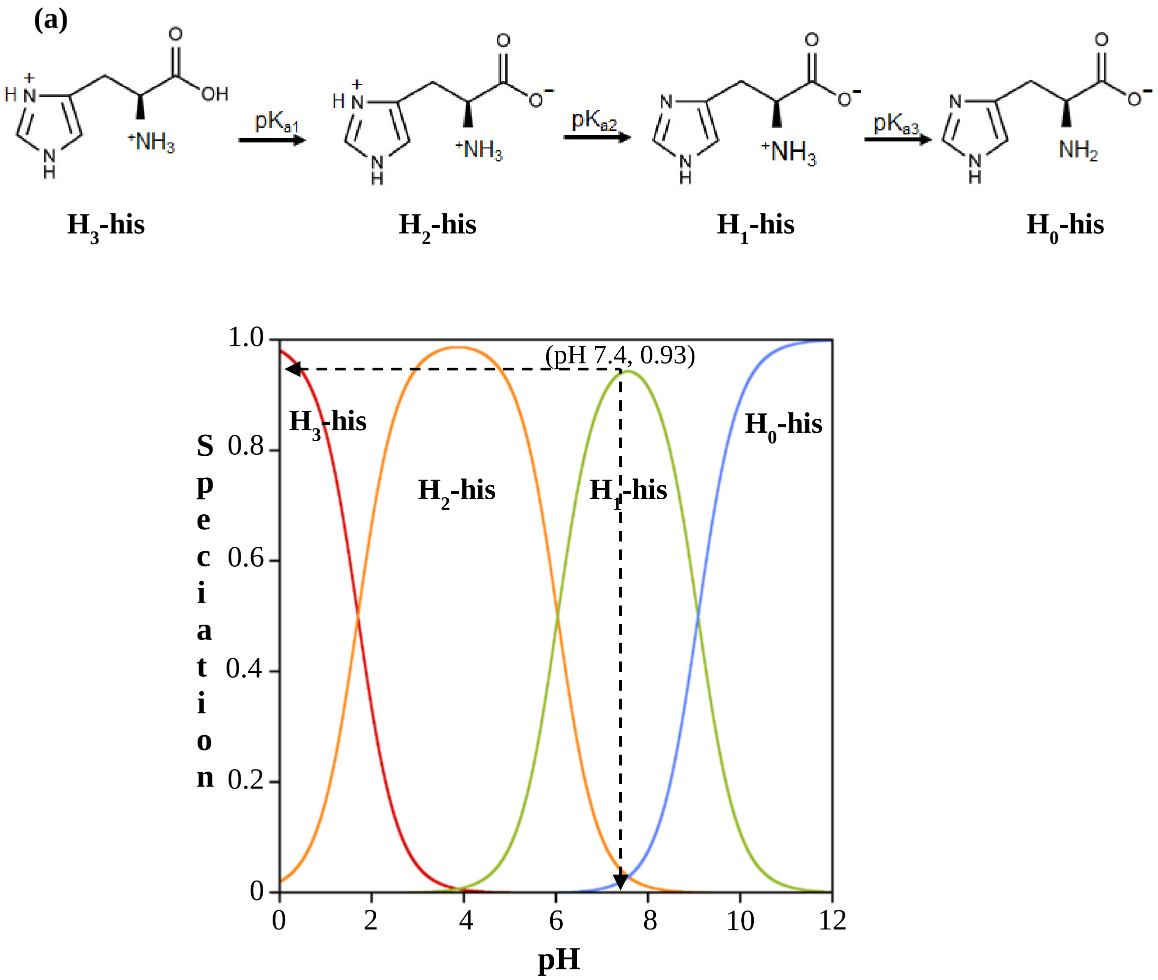

Figure 6.2: Solution phase speciation of histidine as a function of solution pH. (a) Molecular representation of the deprotonation of histidine where $pK_{a1} = 1.70$, $pK_{a2} = 6.04$ and $pK_{a3} = 9.09$. (b) Quantitative calculation of histidine speciation using Henderson-Hasselbalch equation.

These changes in the protonation state is reflected in the ATR-FTIR spectra collected as a function of pH (Figure 6.3) which are thereby used to further resolve the broad bands observed in the solution phase histidine IR spectra.

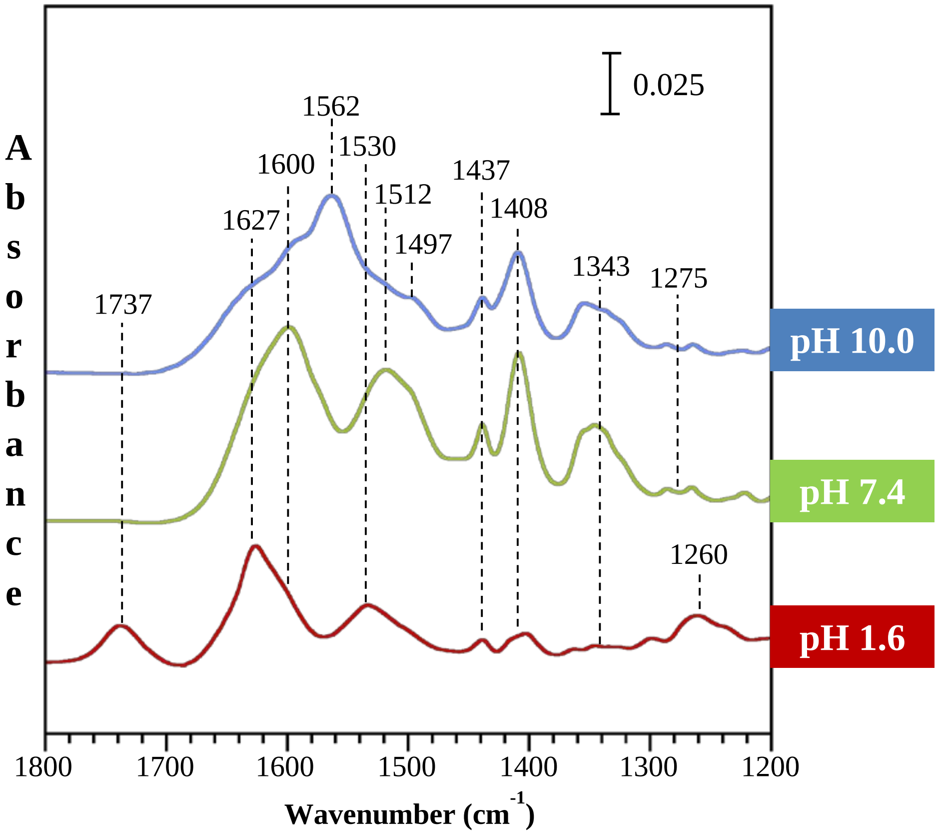

Figure 6.3: ATR-FTIR spectra of solution phase histidine as a function of pH (acidic pH 1.6, neutral pH 7.4, and basic pH 10.0).

At pH 1.6 approximately 57% of the histidine molecules are completely protonated (H_3-his) while in the remaining histidine (43%) the carboxylate group is deprotonated (H_2-his). The prominent peaks at 1737 cm^{-1} and 1627 cm^{-1} results from the carbonyl stretch

[ν_s(C=O)] and the ring breathing [ν_s(C=C)] modes respectively.[241,243,244] Some contribution from the asymmetric carboxylate [ν_{as}(COO$^-$)] stretch vibration can be observed from the shoulder at 1600 cm^{-1}. As the pH increase to pH 7.4 approximately 93% is in the H_1-his form where no protonated carboxylic functionality exists (Figure 6.2). Correspondingly ν_s(C=O) at 1737 cm^{-1} diminish and [ν_s(C=C)] maxima at 1627 cm^{-1} shifts to 1600 cm^{-1} as the asymmetric carboxylate [ν_{as}(COO$^-$)] stretch vibration grows in and overlaps with the ring breathing [ν_s(C=C)] mode. According to literature the broad band in the region of 1485 – 1550 cm^{-1} results from the overlap of ring breathing [ν_s(C=N)+ δ(CH)] and amine group bending δ_s(NH_3^+).[241,243] Changing the solution condition from pH 1.6 to pH 7.4 the peak maxima shifts from 1530 cm^{-1} to 1512 cm^{-1} corresponding to the deprotonation of the imidazole group (Figure 6.2). The IR spectra changes further under basic conditions. At pH 10.0 the peak at 1600 cm^{-1} split into 3 main components. According to literature at pH 7.4 the peak corresponds to overlap of 3 vibrational modes, ν_s(C=C)+δ_{as}(NH_3^+)+ν_{as}(COO$^-$).[241,243] With the deprotonation of the amine group at pH 10.0, the δ_{as}(NH_3^+) mode can potentially redshift and thereby in this study the peak at 1562 cm^{-1} is concluded to correspond to the δ_{as}(NH_2). Thus the shoulder at 1497 cm^{-1} is attributed to the amine group symmetric bending [δ_s(NH_2)]. The peaks at 1437 and 1408 cm^{-1} corresponds to the δ(CH_2) and ν_s(COO$^-$) respectively. Further the broad bands around 1343 and 1260 cm^{-1} also result from the overlaps of the side chain CH_2 groups, imidazole ring and the carboxylic/carboxylate groups. Figure 6.3 illustrates the curve fits for the pH 7.4 solution phase according to the above analysis using Gaussian- Lorentzian (GL30) line shape and these vibrational mode assignments are summarized in Table 6.1. At pH 7.4 the overlapping bands around 1600 and 1512 cm^{-1} cannot be resolved. Thus appear as single broad bands.

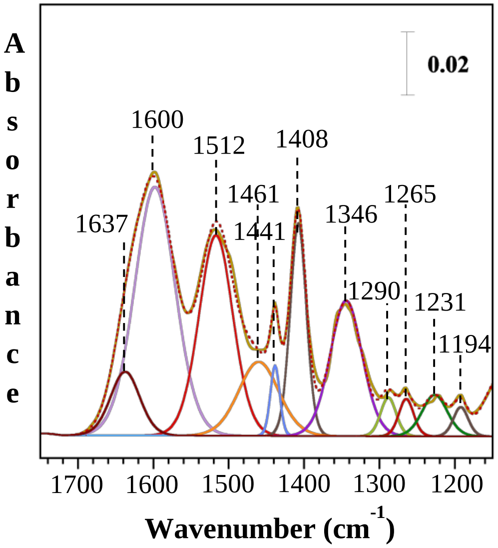

Figure 6.4: ATR-FTIR spectra of Solution phase histidine (250 mM) at pH 7.4 curve fitted using Gaussian – Lorentzian (GL30) line shape. The small component at 1637 cm^{-1} corresponds to the δ(H_2O) arising due to incomplete subtraction of water.

Table 6.1: ATR-FTIR spectroscopic data for solution phase histidine at pH 7.4

Mode of vibration	**Vibrational frequency (cm^{-1})**	
	Experimental values (this study)	**Literature values** (refs: 36, 37, 38)
$\nu_s(C{=}C)_{ring} + \delta_{as}(NH_3^+) + \nu_{as}(COO^-)$	1600	1575 – 1600
$[\nu_s(C{=}N) + \delta(CH)]_{ring} + \delta_s(NH_3^+)$	1461,1512	1485 – 1550
$\delta(CH_2)$	1441	1425 – 1475
$\nu_s(COO^-)$	1408	1390 – 1425
$[\nu_s(C{=}N) + \nu_s(C\text{-}N)]_{ring} + \delta(CH)$	1346	1343 – 1345
$[\nu_s(C\text{-}N) + \nu_s(C\text{-}C)]_{ring} + \gamma(CH_2)$	1265, 1290	1268 – 1270
$\nu(C\text{-}N)_{ring} + \delta(C\text{-}H)$	1194, 1231	1010 – 1265

$\nu_{s/as}$ – Symmetric/asymmetric stretching vibration
$\delta_{s/as}$ – Symmetric/asymmetric deformation/bending
γ – Twisting vibration
δ – Bending vibration

6.4.2 ATR-FTIR Spectroscopy of Histidine Adsorption on TiO_2 Nanoparticle Surfaces.

The vibrational spectra of histidine adsorbed on TiO_2 nanoparticle surface is shown in Figure 6.5. The adsorbed phase spectra were collected over 30 hours to allow saturation. As observed, at the low concentration used, 0.5 mM, there is no significant contribution to the adsorbate vibrational spectrum from solution-phase histidine. There are several significant differences between the solution (Figure 6.4) and adsorbate spectra (Figure 6.5). For example, the relative intensity between $\nu_{as}(COO^-)$ and the other vibrational modes show a significant reduction with the most prominent being that of the band at 1512 cm^{-1}. This suggests there is a change in the absorption coefficient which can

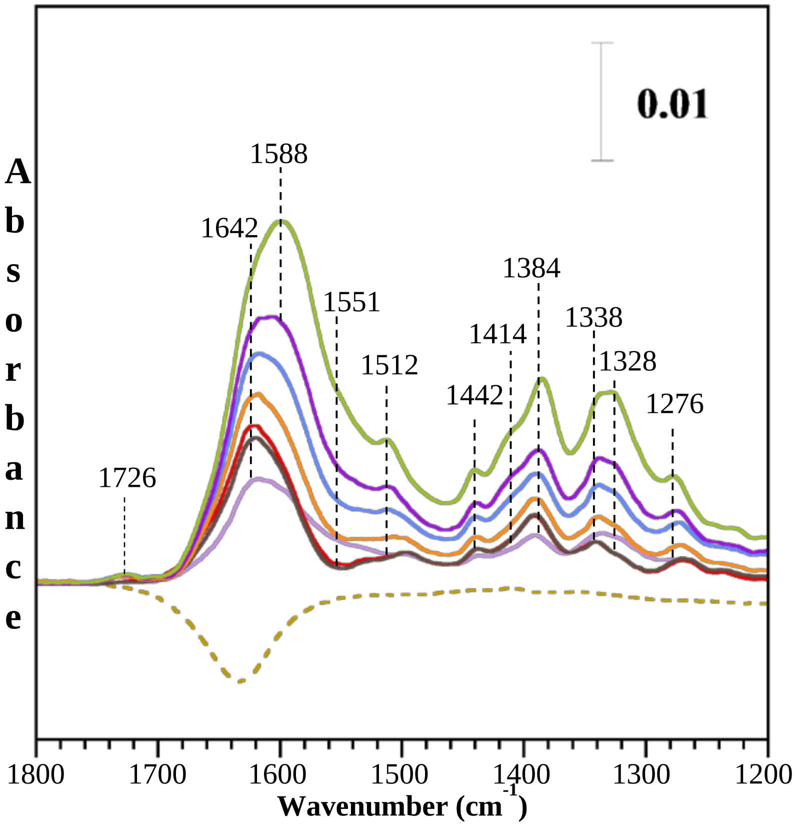

Figure 6.5: ATR-FTIR spectra of adsorbed histidine (0.5 mM) at pH 7.4 as a function of time. Spectra in solid lines are collected at 3, 30 min, 1, 6, 10, 15 and 30 hrs. The dotted line corresponds to the 0.5 mM histidine in solution.

result due to interactions of the functional group with the surface and changes in bond angles, bond distances and symmetry upon adsorption. As already noted, imidazole ring and $\delta_s(NH_3^+)$ vibrations contribute towards bands observed within this spectral range. Furthermore comparing the adsorbed phase to the solution it is clearly observed that $\nu_s(COO^-)$ mode at 1408 cm^{-1} is split into 2 peaks at 1414 and 1384 cm^{-1}. Temporal variations are also observed given by the shifting and broadening of the initial peak maxima at 1642 cm^{-1} to 1588 cm^{-1} over time and a new peak appearing at 1726 cm^{-1} at higher coverage.

In order to resolve the overlapping bands in the adsorbed phase and temporal variations, spectra collected at 3 min, 1 hr, 6 hr and 30 hrs are curve fit using Gaussian Lorentzian (GL30) line shapes which is shown in Figure 6.6 and the corresponding peak assignments are summarized in Table 6.2. The curve fits show that the broad band around 1600 cm^{-1} consists of three main components. The component at 1642 cm^{-1} can be attributed to $\delta(H_2O)$ that result from the incomplete subtraction of water. However, it can also be argued that this component also consist of contributions from the surface complexed imidazole ring vibrations as this component grows consistently with time. The two peaks at 1617 and 1588 cm^{-1} are due to the $\nu_{as}(COO^-)$ of carboxylate groups complexed to the surface in different adsorption modes (bridging/bidentate). Correspondingly the $\nu_s(COO^-)$ shows 2 peaks at 1414 and 1384 cm^{-1}. According to the IR analysis of the solution phase spectra (Figure 6.3) the imidazole group has vibrations in the 1485 – 1550 cm^{-1} region. Therefore the components at 1551 and 1472 cm^{-1} may arise from surface complexed imidazole groups. However, as shown in Figure 6.6c starting at 6 hr a low intense new peak was observed at 1726 cm^{-1} which was observed even after 24 hrs (Figure 6.6d). Since no carbonyl groups can exist at pH 7.4 the origin of this peak indicate the possibility of amide bond formation between the adsorbed histidine molecules. Furthermore the reduction in the relative intensity of the band at 1512 cm^{-1} also suggests the possibility of NH_2 group undergoing reaction.

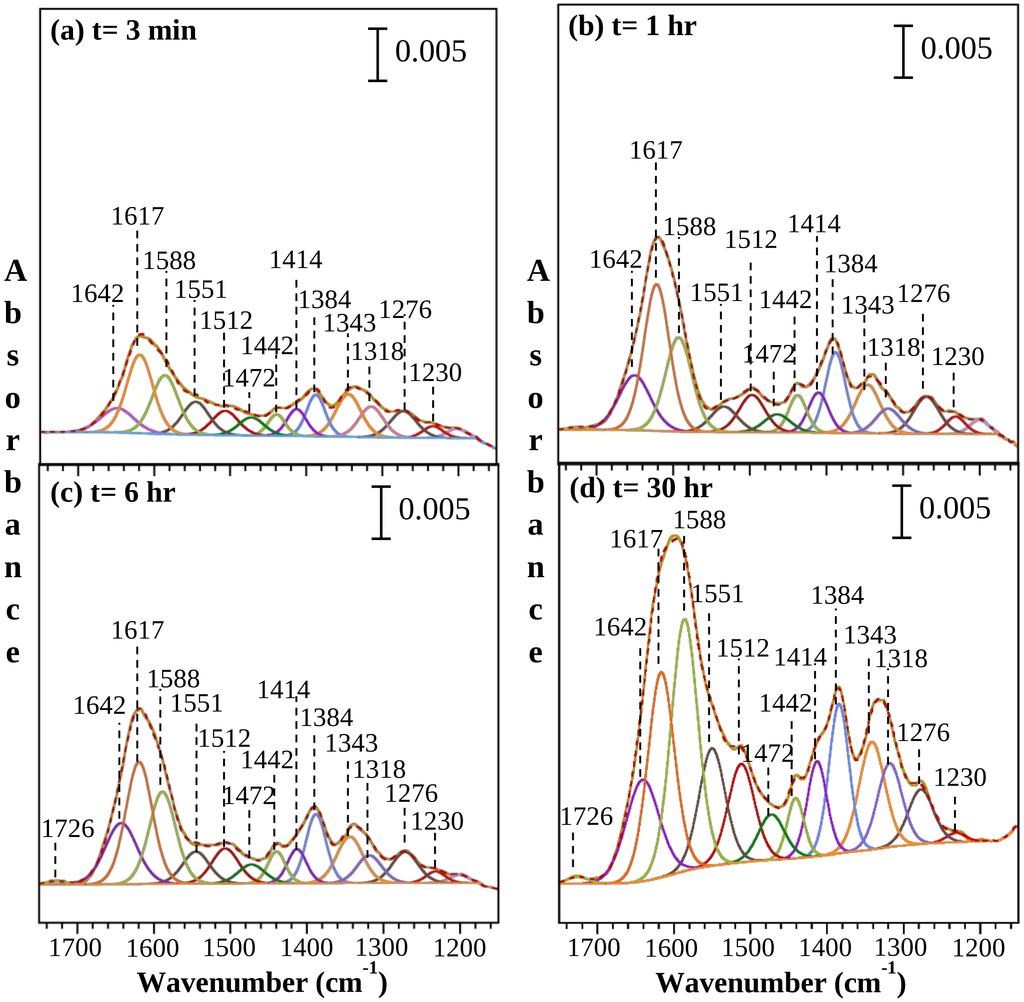

Figure 6.6: ATR-FTIR spectra of histidine (0.5 mM) at pH 7.4 adsorbed on TiO_2 NPs at (a) t = 3 min (b) t = 1 hr (c) t = 6 hrs and (d) t = 30 hrs. Spectra are curve fitted using Gaussian – Lorentzian (GL30) line shape.

Table 6.2: Peak assignments for the curve fit components. Here the FWHM is fixed for the components corresponding to the same functional group with different modes of adsorption.

Wavenumber (cm^{-1})	**Mode of vibration**
1726	ν_s(-Ti-O-C=O)
1642	$\delta(H_2O)+\nu_s(C=C)_{ring}$
1617	$\nu_{as}(COO^-)_{bridged}$
1588	$\nu_{as}(COO^-)_{bidentate}$
1551	$[\nu_s(C=N)+\delta(CH)]_{ring}$
1512,1472	$[\nu_s(C=N)+\delta(CH)]_{ring}+\delta(NH_3^+)$
1442	$\delta(CH_2)$
1414	$\nu_{as}(COO^-)_{bidentate}$
1384	$\nu_{as}(COO^-)_{bridged}$
1343,1318	$[\nu_s(C=N)+\nu_s(C-N)]_{ring}+\delta(CH)$
1230	$\nu(C-N)_{ring}+\delta(C-H)$

Although amide bond formation between a carboxylic acid and an amine is an unfavorable process which requires activating the carboxylic group, the surface can provide a lower energy pathway with these high surface energy materials and therefore the possibility cannot be ignored. If peptide bond formation is occurring on the surface of these nanoparticles it can have many important biological implications. In this case the peak observed at 1726 and 1551 cm^{-1} may result from the amide I and amide II vibrational modes. Thus adsorption of his-gly peptide on TiO_2 NPs was studied under the same conditions for comparison (Figure 6.7).

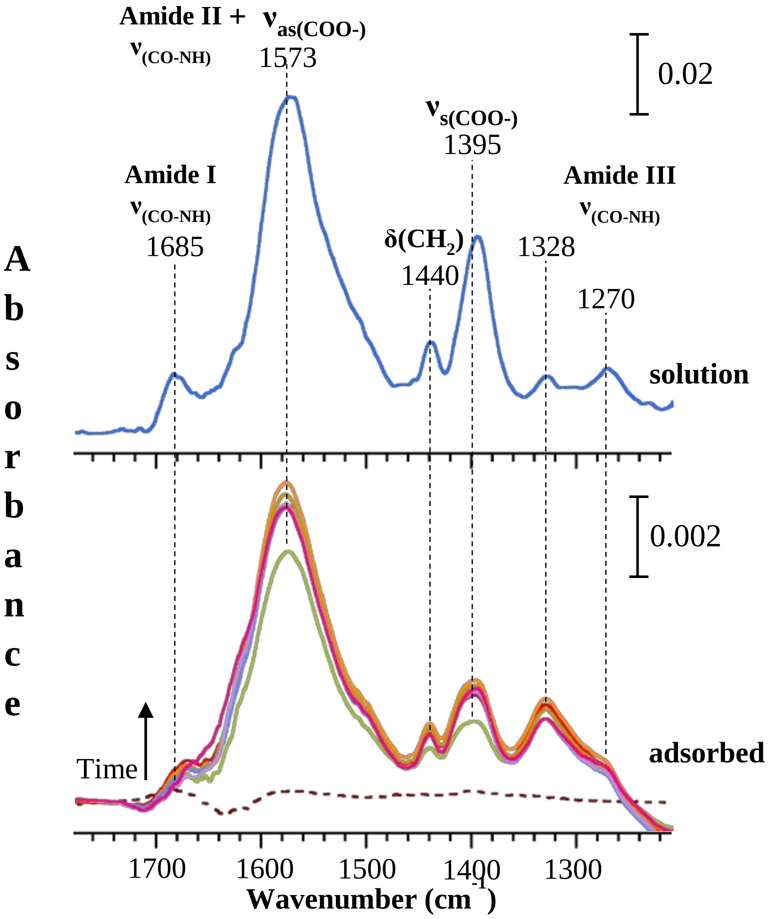

Figure 6.7: ATR-FTIR spectra collected for his-gly peptide adsorbed (0.5 mM) on TiO_2 NPs over 60 minutes compared to his-gly solution (10 mM). The dotted line corresponds to the 0.5 mM his-gly in solution.

The reason for selecting this peptide was to have less complexity in the spectra and ease of identifying the amide bond peak. Figure 6.7 shows the spectra for solution phase and the adsorbed phase peptide respectively. There is no solution phase contribution at 0.5 mM as can be seen in Figure 6.7 and no difference is observed between solution phase and adsorbed phase. In general, amide I and amide II peaks are observed at 1650 and 1545 cm^{-1} respectively in proteins. But in this dipeptide the overlap of the $\nu_{as}(COO^-)$ of the terminal carboxylate group with the amide II peak has resulted in a single broad band centered around 1574 cm^{-1} which does resemble the broad peak at 1588 cm^{-1} in adsorbed histidine. But the amide I peak for his-gly is at 1685 cm^{-1} which is significantly different from adsorbed histidine and confirmed that the peak at 1726 cm^{-1} is not due to amide bond formation. Furthermore the amide III region was not observed in adsorbed histidine spectra. Thus it was concluded the peaks at 1551 and 1472 cm^{-1} are a result of surface complexed imidazole group and this complexation causes a change in the relative intensities in the adsorbed phase spectra. Thus the peak at 1726 cm^{-1} may arise from the carboxylate (COO^-) coordination with Ti-atoms in corners and edges of the nanoparticle surface planes that can disrupt the carboxylate resonance at higher coverages.

In the curve fit spectra $\delta(CH_2)$ mode at 1442 cm^{-1} shows no shifts but there are changes in the region 1150-1380 cm^{-1} corresponding to the imidazole ring breathing modes. In a study by Tsud *et al.,* histidine adsorption on CeO_2 was investigated by synchrotron radiation photoemission, resonant photoemission and NEXAFS, histidine binding to the ceria surface was deduced to be via the anionic carboxylate and all three nitrogen atoms with the imidazole ring parallel to the surface.[245] The N-atoms of the imidazole ring was found to interact strongly via the π-orbitals while the amine N-atom interacts with the oxide via its H-atoms. Based on the IR analysis of this study it can be concluded that histidine adsorption on TiO_2 nanoparticles occur in a very similar mode of adsorption. The proposed modes of histidine adsorption on TiO_2 nanoparticle surfaces as suggested by the spectroscopic data are illustrated in Figure 6.8.

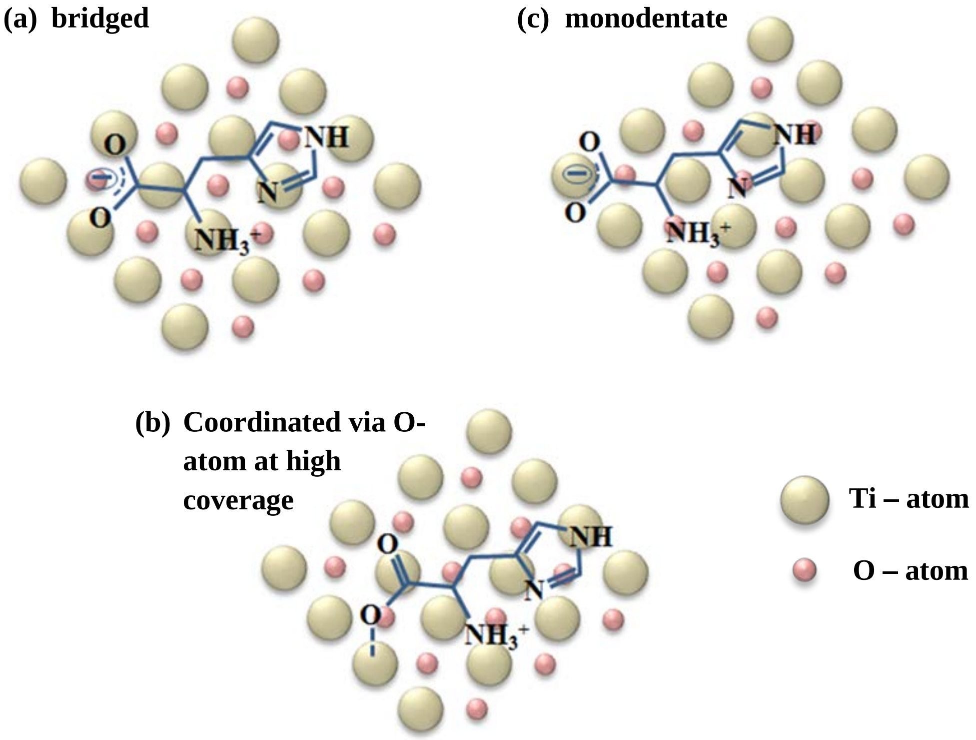

Figure 6.8: A cartoon representation of different adsorption modes of histidine on TiO_2 nanoparticle surfaces. The imidazole ring interacts with the surface Ti-atoms via the π-orbitals and the amine group can form H-bonds with the surface O-atoms. The main difference is between the interactions via the carboxylic group. In both (a) and (b) structures the imidazole ring is considered to be oriented parallel to the surface. At higher coverage it can potentially orient upwards.

Reversibility of this adsorption was investigated by flushing the histidine adsorbed TiO_2 film with pH 7.4 water (Figure 6.9). All spectral features decreased in intensity except the peaks at 1726, 1588, 1442 and 1384 cm^{-1}. Strong conclusions cannot be drawn from the peaks around 1726 and 1588 cm^{-1} because of the contributions from the $\delta(H_2O)$ in this region. Nevertheless it can be stated that they potentially result from the relatively strongly bound species on this nanoparticle surface. However their concentration is relatively low compared to those desorbed.

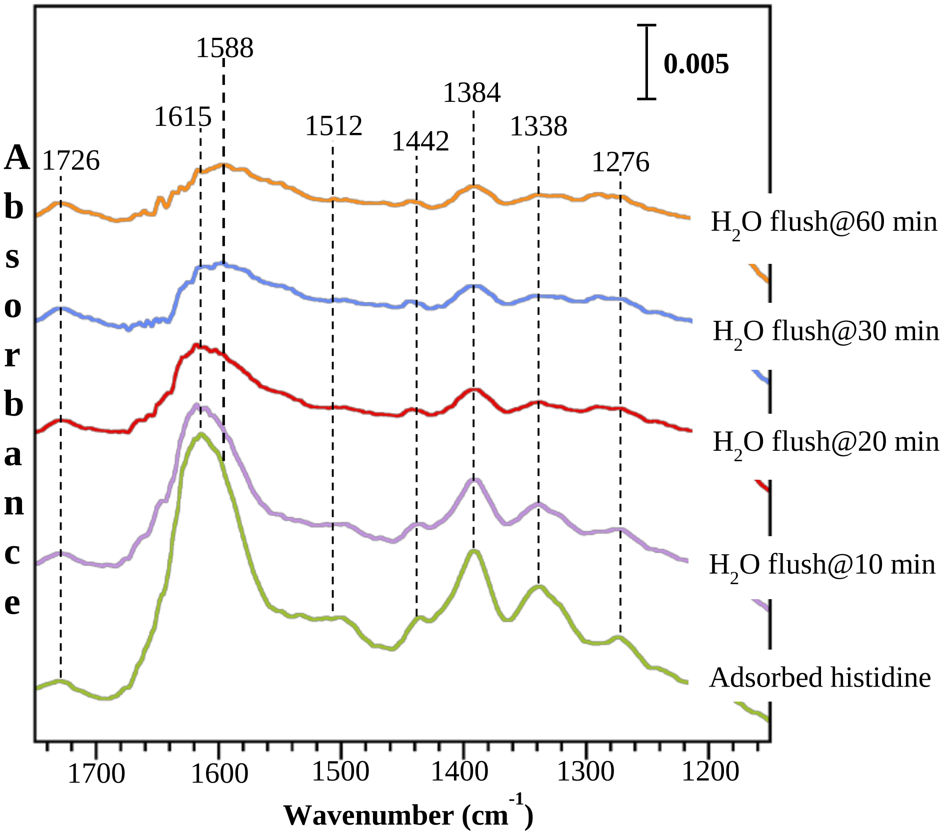

Figure 6.9: ATR-FTIR spectra collected as a function of time by flushing the histidine adsorbed TiO_2 nanoparticle film with pH 7.4 water.

6.4.3 Adsorption Isotherms and Binding Affinity (K) for Histidine on 4 nm TiO_2

The quantitative adsorption studies of histidine on TiO_2 at pH 7.4 showed a Langmuir-like behavior with an initial uptake being linearly proportional to concentration and then leveling off at higher concentrations (Figure 6.10). Although there may be multiple binding sites and interactions between adsorbates, these structures may be similar in energy. Therefore, assuming monolayer adsorption of histidine on TiO_2 nanoparticles surface at pH 7.4 and reversible at 24 hours, the experimental data can be fit using the Langmuir model, according to Eq: 6.1.

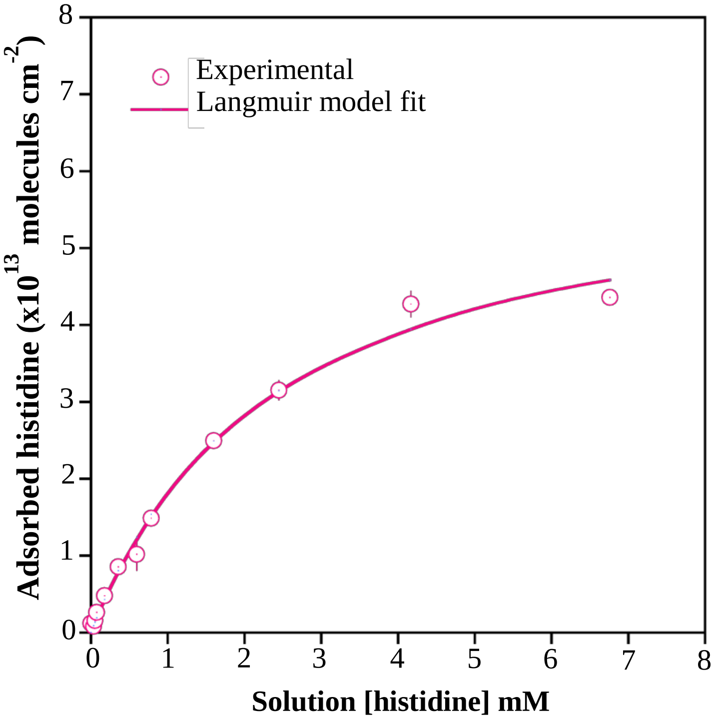

Figure 6.10: Adsorption isotherm for histidine adsorbed on 4 nm TiO_2 NPs at pH 7.4 and at a temperature of 293 K. According to the Langmuir adsorption model $K_{ads} = 4.2 \pm 0.5 \times 10^2$ L mol^{-1} and $C_{max} = 6.2 \pm 0.3 \times 10^{13}$ molecules cm^{-2}.

According to the Langmuir model,

$$C_{ads} = \frac{KC_{ads}^{max}[C_{eq}]}{1 + K[C_{eq}])} \qquad (Eq: 6.1)$$

where C_{ads} – adsorbed [histidine], C_{eq} – unbound [histidine] at the equilibrium, C_{max} – saturation [histidine] and *K*– equilibrium binding constant. From this analysis, the saturation concentration (C_{max}) and the equilibrium binding constant (*K*) of histidine were calculated to be $6.2 \pm 0.3 \times 10^{13}$ molecules/cm^2 and $4.2 \pm 0.5 \times 10^2$ L mol^{-1} respectively. Additionally, the free energy (ΔG) of histidine adsorption on 4 nm TiO_2 particles can be calculated by

$$\Delta G = -RT \ln K \qquad (Eq: 6.2)$$

to be -14.7 ± 0.3 kJ mol^{-1} at 293 K. This value of the free energy is in accordance with the literature to be described more as a physisorption process. Therefore it can be concluded that in solution at pH 7.4, histidine is physisorbed on the TiO_2 NPs. Also these thermodynamic parameters obtained from the quantitative adsorption studies suggest that the interaction between histidine and TiO_2 nanoparticles to be H-bonding, dipole-dipole and/or electrostatic interactions. Adsorption of histidine was further conducted at different temperatures; 293, 298, 303, 310 and 320 K to obtain the enthalpy and the entropy changes associated with the adsorption process. The respective equilibrium constants and calculated free energies are given in Table 6.3. The thermodynamic parameters calculated from this data showed an exothermic adsorption with $\Delta H = -24.5 \pm 5.2$ kJ mol^{-1} and $\Delta S = -0.03 \pm 0.02$ kJ mol^{-1} K^{-1}. These values agree well with a typical physisorption process.

Additional experiments conducted under different ionic strength conditions gave decreasing surface adsorption with increasing ionic strength initially and approached a constant value at the highest salt concentrations investigated (Figure 6.11). Histidine that adsorb at high ionic strength are not bound electrostatically but consist of those which are H-bonded or coordinated with the surface. Therefore it can be concluded that only a portion of histidine adsorbs via electrostatic interactions and the remaining via H-bonding or coordination.

Table 6.3: Temperature dependent adsorption studies of histidine at pH 7.4.

Temperature (K)	**K_{ads} (L mol^{-1})**	**$\Delta G = -RT \ln K_{ads}$ (kJ mol^{-1})**
293	$4.2 \pm 0.5 \times 10^2$	-14.7 ± 0.3
298	$3.3 \pm 0.5 \times 10^2$	-14.4 ± 0.4
303	$3.0 \pm 0.5 \times 10^2$	-14.4 ± 0.4
310	$1.9 \pm 0.2 \times 10^2$	-13.5 ± 0.3
320	$1.9 \pm 0.5 \times 10^2$	-13.9 ± 0.6

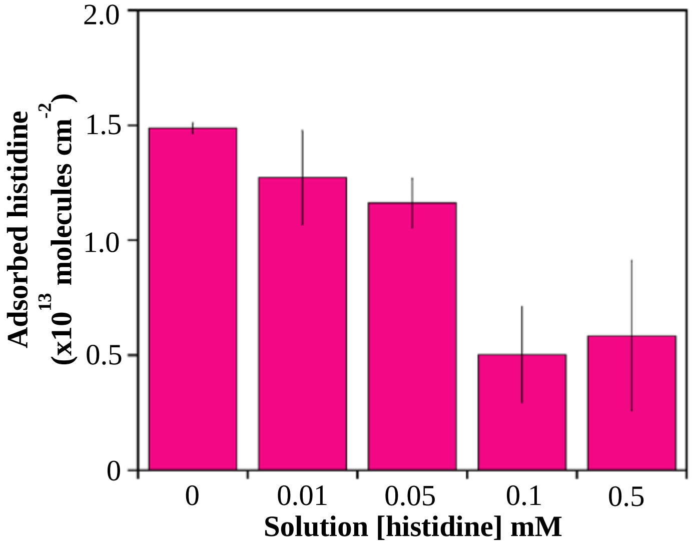

Figure 6.11: Ionic strength dependence of histidine adsorption at pH 7.4. Error bars represent the standard deviation for three replicates.

6.4.4 Aggregation Behavior of TiO_2 NPs in the Presence of Histidine

Aggregation plays a key role in determining the mobility, uptake and dissolution behavior of nanoparticles.[24,71,84] Therefore the current study investigated any changes that may occur in the aggregation behavior of TiO_2 nanoparticles upon adsorption of histidine. In the absence of histidine, the hydrodynamic diameter was nearly half-micron in size, 434 ± 33 nm. The aggregate size did not change significantly upon addition of histidine (Table 6.4). The zeta potential values for each of these solutions varied slightly but stayed within a small range of -36.0 ± 2.6 mV (0 mM histidine) to -30.7 ± 2.4 mV (0.1 mM histidine) indicating that no significant changes in the surface charge with histidine adsorption which is consistent with the lack of the change in aggregation behavior observed. The aggregation is controlled by the net interactive forces between the surfaces which can change with modifications to surface charge and steric repulsions.[84,99,246] At pH 7.4, histidine is in its neutral from and therefore does not introduce an additional charge to NP surface upon adsorption. Furthermore the saturation coverage of histidine ($6.2 \pm 0.3 \times 10^{13}$ molecules/cm^2) indicates only a single layer of histidine is on the NPs surface. Therefore the steric repulsions do not increase significantly upon histidine binding.

Table 6.4: Hydrodynamic diameter and zeta potential measurements as a function of histidine concentration using dynamic light scattering (DLS).

[Histidine] mM	D_h (nm)	Zeta potential (mV)
0	434 ± 33	-36.0 ± 2.6
0.01	568 ± 82	-33.0 ± 3.7
0.1	501 ± 34	-30.7 ± 2.4
1	500 ± 54	-31.7 ± 2.9
5	584 ± 36	-32.6 ± 2.6

6.5 Conclusions and Implications

The current study gives a detailed analysis of both bulk and microscopic behavior of 4 nm TiO_2 NPs in physiological pH aqueous solutions. The findings are briefly outlined as follows.

1. The equilibrium binding constant and maximum adsorption for histidine on TiO_2 NPs was $4.2 \pm 0.5 \times 10^{2}$ L mol^{-1} and $6.2 \pm 0.3 \times 10^{13}$ molecules/cm^{2} respectively at pH 7.4 at a temperature of 293 K. The adsorption was observed to be reversible.
2. The free energy change associated with the adsorption was -14.7 ± 0.3 kJ mol^{-1} at 293 K.
3. Temperature dependent studies over the range of 293-320 K gave enthalpy (ΔH) and entropy changes (ΔS) of -24.5 ± 5.2 kJ mol^{-1} and -0.03 ± 0.02 kJ mol^{-1} K^{-1}, respectively.
4. From the spectroscopic data, it is proposed that there are different modes of adsorption for histidine on the nanoparticle surface. These occur through the imidazole side chain and the carboxylate group via H-bonding and coordination with the surface Ti-atoms respectively.
5. Bulk adsorption studies and surface charge measurements also indicate electrostatic interactions between the protonated amine group and the negatively charged surface.
6. The aggregation behavior as measured by DLS was little affected as the surface charge did not change with histidine adsorption.

A detailed understanding of amino acid residues allows for insights into understanding the complexity and challenges of dynamic changes and complex interactions with proteins at the nano-bio interface. These single amino acid component studies can be used in prediction models for more complex systems. Xia *et al*. has developed a biological surface adsorption index (BSAI) to characterize these interactions under biologically relevant aqueous conditions.[247,248] In that study, the adsorption coefficients are correlated to a set of solute descriptors (R, π, α, β, V) by

$$\log K_i = c + rR_i + p\pi_i + a\alpha_i + b\beta_i + vV_i \qquad (Eq{:}\,6.3)$$

With known adsorption coefficients and regression analysis the coefficients [r, p, b, v] can be derived which correspond to the hydrophobic, H-bond acidity/basicity, dipolarity/polarizability and lone-pair interactions. The constant c is the electrostatic interactions which can be measured by the zeta potential. Therefore bulk measurements along with microscopic analysis can allow for the validation of such models.

Furthermore, several simulation and experimental studies have been conducted to understand the adsorption process of amino acids on nanoparticle surfaces and specifically histidine. Koppen *et al.* has studied the adsorption configurations of cysteine, lysine, glutamic acid and histidine on anatase (101) and (001) and rutile (110) and (100) using Carr-Parrinello simulations of aqueous solutions.[249] The calculated adsorption energies of glutamic acid and lysine using these configurations are given as 160 and 110 kJ mol^{-1} for rutile surface while on anatase surface it was reported to be largely dependent on the surface orientation. Feyer *et al.* used XPS and NEXAFS to study the adsorption of L-histidine from the gas phase on clean and oxygen coated Cu(110) surface at submonolayer, monolayer and multilayer coverage.[236] The spectra obtained have shown that at low coverage histidine interact only via the carboxylate group and the imidazole N-atoms and as the coverage increase the molecules were randomly oriented. This study was followed by investigating the adsorption of histidine and histidine containing peptides on Au(111) that has shown chemisorption via the imidazole ring and carboxylate group.[237] Furthermore differences were observed between the gly-his-gly and gly-gly-his peptide spectra highlighting the influence of amino acid sequence on the bonding geometry. All of the experimental studies noted above are conducted under highly controlled, gas phase, conditions which give insightful information on the amino acid - surface interactions. However, in terms of nanotoxicology, which deals with more complex matrices and in aqueous environments, the applicability of gas-phase investigations in the absence of solvent effects become questionable. Therefore, the current study focuses on an experimental approach to understand the adsorption of histidine on TiO_2 nanoparticle surfaces in aqueous solutions at physiological pH 7.4.

Acknowledgment

Although the research described in this article has been funded in part by the Environmental Protection Agency through grant number EPA RD-83171701-0 to VHG, it has not been subjected to the Agency's required peer and policy review and therefore does not necessarily reflect the views of the Agency and no official endorsement should be inferred.

CHAPTER 7

CONCLUSIONS AND FUTURE DIRECTIONS

As Wolfgang Pauli once famously said, "God made the bulk; surfaces were invented by the devil". Thus the research presented in here is focused on understanding the behavior of metal based nanomaterials in aqueous environment as it relates to surface properties and interactions leading to their transformations and potential implications. The primary focus is on the fundamental details of ligand adsorption on nanoparticle surfaces, analysis of changes in aqueous phase behavior due to surface adsorption and to extend this molecular based understanding to explain and predict the overall environmental processing of nanomaterials in aqueous environments, thus for their safe design.

In chapter 2, the details of bulk and spectroscopic techniques used in nanoparticle characterization, quantitative ligand adsorption, nanoparticle dissolution and analysis of particle-particle interactions were outlined. This suite of analytical techniques and methods allow for the correlation of surface and bulk properties of the metal based nanoparticles to the dynamic processes observed under complex environmental and biological conditions. Although in this study, the complexity of the medium matrices was relatively simple, this methodology allowed for the isolation and of the individual components that makes up the complex system.

In chapter 3, the details of citric acid adsorption on TiO_2 nanoparticles were discussed. The spectroscopic analysis showed deprotonating citrate species on the surface of TiO_2 nanoparticles which changed the net surface charge. This change in surface charge enhanced aggregation under acidic conditions and inhibited it under circumneutral conditions. This directly affects the mobility of these nanoparticles in the environment as particle aggregation result in sedimentation and limited distribution resulting in several different implications. (1) These nanoparticles can concentrate and deposit in a particular location or spread over a long range. (2) The aqueous environments are constantly changing and therefore this behavior can very well be interchangeable. (3) When the medium is within a biological system, changes in the transport properties can cause detrimental effects on organs where these particles accumulate especially if they reach the lethal dose limits. With citric acid and TiO_2 nanoparticles being abundant both in the environment and in biological systems these findings provide valuable insights into their aqueous phase behavior.

In chapter 4, the importance of accounting for the aging of nanomaterials which are used in the environmental health and safety studies was highlighted. The study clearly shows marked differences between the physicochemical properties which are reflected in their environmental processing. More specifically the copper nanoparticles which are focused in the study oxidized over time changing in their size, shape and chemical composition. Thus when they are subjected to ligand promoted dissolution the extent to which they dissolve reduced for the aged nanoparticles. Furthermore an important finding of this study was the “total mobilized concentration” of copper which was operationally defined as the sum of dissolved ions and dissolved smaller nanoparticles. This is potentially an important factor to consider in toxicological studies where enhanced toxicities are observed with nanoparticles. Furthermore the metallic core of the nanoparticles affects the overall surface features as observed by the differences between adsorption of oxalic acid on to aged copper and CuO nanoparticles. Therefore the oxidized surface of aged copper is not equivalent to CuO surfaces.

In chapter 5, the size dependent dissolution of ZnO nanoparticles was presented as well as how certain ligands inhibit this behavior while others retain it. The size dependent dissolution was studied at circumneutral pH and the ligands of interest were citric acid and bovine serum albumin (BSA). The size of the nanoparticles varied from 4 nm to 130 nm and smallest nanoparticles showed the highest dissolution. Normalizing to the nanoparticle surface area the dissolution was equivalent for all the sizes which highlighted that this enhanced dissolution was a consequence of larger surface area and increased sites of "dissolution hot spots". However, citric acid resulted in completely masking the size dependence as a result of nonspecific adsorption onto the nanoparticle surfaces. Ligand adsorption is known to polarizing and weakening the lattice structure at the surface promoting dissolution. Bovine serum albumin which is an equivalent of a human serum protein on the other hand forms a protein corona encapsulating the ZnO particles and can potentially inhibit dissolution. The surface energy of ZnO nanoparticles were estimated using the dissolution data and Ostwald–Freundlich model for size dependent dissolution. The value of 0.06 Jm^{-2} was an underestimation compared to the expected which highlights the lack of surface details incorporated into these classical models.

In chapter 6, specific nano-bio interactions at the TiO_2 nanoparticles surface using histidine, an essential amino acid is discussed. Extensive spectroscopic analysis revealed that the histidine interact with the surface mainly via its imidazole side chain and the carboxylic functional group. The adsorption was reversible and therefore the adsorption of histidine quantified using HPLC was modeled using Langmuir adsorption isotherms to obtain the thermodynamics of adsorption. Thermodynamic data suggested physisorption of histidine on adsorption and this does not impact the aggregation behavior of TiO_2 nanoparticles in contrast to what was observed with vitric acid. This study gives insights into side chain interactions of biological molecules which is crucial to understand the toxicological levels at the molecular scale.

The behavior of engineered nanoparticles will be dictated by the surface atoms and their high surface free energies. Surface structure, surface reconstruction, surface relaxation and surface adsorption will be driving forces in nearly all processes involving nanomaterials yet often the details of these driving forces are poorly understood especially in complex *milieu* such as those found in the environment. From the discussion presented here, it is evident that there are still many unexplored areas of investigations that need to be addressed in order to fully understand and evaluate the properties of nanomaterials in the environment. Greater focus is needed on nanomaterials having very small dimension where size-dependent properties are observed. Therefore future research conducted should be focused on gathering information with respect to complex interactions that connect functional properties to structure, bonding, composition and dynamics. Some of the grand challenges include:

1. Greater understanding of the size- and shape-dependent chemistry and/or properties of nanomaterials that are important in environmental processes (e.g redox behavior, surface chemistry).
2. Analysis of surfaces in complex environments and the use of in-situ characterization of surface structure and composition in complex milieu.
3. Identify the role of surface functional groups on the stability of nanomaterials and delineating the details of the surface adsorption process including the mode of adsorption and reversibility of adsorption and possible displacement reactions that can occur.
4. Determine the primary form of engineered nanomaterial release into the environment in terms of size, shape and surface functionality.
5. Identify various reaction mechanisms that nanoparticles can potentially undergo in the environment so as to better understand transformations that are most likely to occur.

To meet these challenges it is essential for there to be theoretical and experimental efforts devoted toward understanding nanomaterials and the properties that are important in their mobility, uptake and toxicity. While monitoring is a key aspect to environmental studies, simulations backed by solid scientific underpinnings can greatly expand the understanding of these materials.

REFERENCES

1. Fabrega, J.; Fawcett, S. R.; Renshaw, J. C.; Lead, J. R. Silver nanoparticle impact on bacterial growth: Effect of pH, concentration, and organic matter. *Environmental Science & Technology* **2009**, *43*, 7285-7290.

2. Hwang, G. L.; Hwang, K. C.; Shieh, Y.-T.; Lin, S.-J. Preparation of carbon nanotube encapsulated copper nanowires and their use as a reinforcement for Y-Ba-CuO superconductors. *Chemistry of Materials* **2003**, *15*, 1353-1357.

3. Song, W.; Li, G.; Grassian, V. H.; Larsen, S. C. Development of improved materials for environmental applications: Nanocrystalline NaY zeolites. *Environmental Science & Technology* **2005**, *39*, 1214-1220.

4. Masciangioli, T.; Zhang, W.-X. Peer reviewed: Environmental technologies at the nanoscale. *Environmental Science & Technology* **2003**, *37*, 102A-108A.

5. Zhang, D. W.; Chen, C. H.; Zhang, J.; Ren, F. Novel electrochemical milling method to fabricate copper nanoparticles and nanofibers. *Chemistry of Materials* **2005**, *17*, 5242-5245.

6. Athanassiou, E. K.; Grass, R. N.; Stark, W. J. Large-scale production of carbon-coated copper nanoparticles for sensor applications. *Nanotechnology* **2006**, *17*, 1668-1673.

7. Bo, Z.; Yu, K.; Lu, G.; Mao, S.; Chen, J.; Fan, F.-g. Nanoscale discharge electrode for minimizing ozone emission from indoor corona devices. *Environmental Science & Technology* **2010**, *44*, 6337-6342.

8. Lowry, G. V.; Hotze, E. M.; Bernhardt, E. S.; Dionysiou, D. D.; Pedersen, J. A.; Wiesner, M. R.; Xing, B. Environmental occurrences, behavior, fate, and ecological effects of nanomaterials: An introduction to the special series. *Journal of Environmental Quality* **2010**, *39*, 1867-1874.

9. Nowack, B.; Ranville, J. F.; Diamond, S.; Gallego-Urrea, J. A.; Metcalfe, C.; Rose, J.; Horne, N.; Koelmans, A. A.; Klaine, S. J. Potential scenarios for nanomaterial release and subsequent alteration in the environment. *Environmental Toxicology and Chemistry* **2012**, *31*, 50-59.

10. Gottschalk, F.; Sonderer, T.; Scholz, R. W.; Nowack, B. Modeled environmental concentrations of engineered nanomaterials (TiO_2, ZnO, Ag, CNT, Fullerenes) for different regions. *Environmental Science & Technology* **2009**, *43*, 9216-9222.

11. Nowack, B. Nanosilver revisited downstream. *Science* **2010**, *330*, 1054-1055.

12. Liu, J.; Hurt, R. H. Ion release kinetics and particle persistence in aqueous ano-silver colloids. *Environmental Science & Technology* **2010**, *44*, 2169-2175.

13. Buzea, C.; Pacheco, I. I.; Robbie, K. Nanomaterials and nanoparticles: Sources and toxicity. *Biointerphases* **2007**, *2,* MR17-MR71.

14. Auffan, M.; Rose, J.; Wiesner, M. R.; Bottero, J.-Y. Chemical stability of metallic nanoparticles: A parameter controlling their potential cellular toxicity *in vitro*. *Environmental Pollution* **2009**, *157*, 1127-1133.

15. Wiesner, M. R.; Lowry, G. V.; Alvarez, P.; Dionysiou, D.; Biswas, P. Assessing the risks of manufactured nanomaterials. *Environmental Science & Technology* **2006**, *40*, 4336-4345.

16. Nowack, B.; Bucheli, T. D. Occurrence, behavior and effects of nanoparticles in the environment. *Environmental Pollution* **2007**, *150*, 5-22.

17. Adamcakova-Dodd, A.; Thorne, P. S.; Grassian, V. H.: *In vivo* toxicity studies of metal and metal oxide nanoparticles. *General, Applied and Systems Toxicology*; John Wiley & Sons, Ltd, 2009.

18. Lai, C.-H.; Lu, M.-Y.; Chen, L.-J. Metal sulfide nanostructures: Synthesis, properties and applications in energy conversion and storage. *Journal of Materials Chemistry* **2012**, *22*, 19-30.

19. Shen, S.; Wang, Q. Rational tuning the optical properties of metal sulfide nanocrystals and their applications. *Chemistry of Materials* **2012**.

20. Lai, C.-H.; Huang, K.-W.; Cheng, J.-H.; Lee, C.-Y.; Hwang, B.-J.; Chen, L.-J. Direct growth of high-rate capability and high capacity copper sulfide nanowire array cathodes for lithium-ion batteries. *Journal of Materials Chemistry* **2010**, *20*, 6638-6645.

21. Mueller, N. C.; Nowack, B. Exposure modeling of engineered nanoparticles in the environment. *Environmental Science & Technology* **2008**, *42*, 4447-4453.

22. Moore, M. N. Do Nanoparticles present ecotoxicological risks for the health of the aquatic environment? *Environment International* **2006**, *32*, 967-976.

23. Baun, A.; Hartmann, N. B.; Grieger, K. D.; Hansen, S. F. Setting the limits for engineered nanoparticles in european surface waters - Are current approaches appropriate? *Journal of Environmental Monitoring* **2009**, *11*, 1774-1781.

24. Colvin, V. L. The potential environmental impact of engineered nanomaterials. *Nature Biotechnology* **2003**, *21*, 1166.

25. AshaRani, P. V.; Low Kah Mun, G.; Hande, M. P.; Valiyaveettil, S. Cytotoxicity and genotoxicity of silver nanoparticles in human cells. *ACS Nano* **2008**, *3*, 279-290.

26. Braydich-Stolle, L. K.; Speshock, J. L.; Castle, A.; Smith, M.; Murdock, R. C.; Hussain, S. M. Nanosized aluminum altered immune function. *ACS Nano* **2010**, *4*, 3661-3670.

27. Brunner, T. J.; Wick, P.; Manser, P.; Spohn, P.; Grass, R. N.; Limbach, L. K.; Bruinink, A.; Stark, W. J. *In vitro* cytotoxicity of oxide nanoparticles: Comparison to asbestos, silica, and the effect of particle solubility. *Environmental Science & Technology* **2006**, *40*, 4374-4381.

28. Liu, J.; Sonshine, D. A.; Shervani, S.; Hurt, R. H. Controlled release of biologically active silver from nanosilver surfaces. *ACS Nano* **2010**, *4*, 6903-6913.

29. Choi, O.; Hu, Z. Size dependent and reactive oxygen species related nanosilver toxicity to nitrifying bacteria. *Environmental Science & Technology* **2008**, *42*, 4583-4588.

30. Sotiriou, G. A.; Pratsinis, S. E. Antibacterial activity of nanosilver ions and particles. *Environmental Science & Technology* **2010**, *44*, 5649-5654.

31. Fritz, G.; Schädler, V.; Willenbacher, N.; Wagner, N. J. Electrosteric stabilization of colloidal dispersions. *Langmuir* **2002**, *18*, 6381-6390.

32. Limbach, L. K.; Li, Y.; Grass, R. N.; Brunner, T. J.; Hintermann, M. A.; Muller, M.; Gunther, D.; Stark, W. J. Oxide nanoparticle uptake in human lung fibroblasts: Effects of particle size, agglomeration, and diffusion at low concentrations. *Environmental Science & Technology* **2005**, *39*, 9370-9376.

33. Xia, T.; Kovochich, M.; Liong, M.; Mädler, L.; Gilbert, B.; Shi, H.; Yeh, J. I.; Zink, J. I.; Nel, A. E. Comparison of the mechanism of toxicity of zinc oxide and cerium oxide nanoparticles based on dissolution and oxidative stress properties. *ACS Nano* **2008**, *2*, 2121-2134.

34. Thill, A.; Zeyons, O. l.; Spalla, O.; Chauvat, F.; Rose, J. m.; Auffan, M. l.; Flank, A. M. Cytotoxicity of CeO_2 nanoparticles for *Escherichia coli*. Physico-chemical insight of the cytotoxicity mechanism. *Environmental Science & Technology* **2006**, *40*, 6151-6156.

35. Johnston, B. D.; Scown, T. M.; Moger, J.; Cumberland, S. A.; Baalousha, M.; Linge, K.; van Aerle, R.; Jarvis, K.; Lead, J. R.; Tyler, C. R. Bioavailability of nanoscale metal oxides TiO_2, CeO_2, and ZnO to fish. *Environmental Science & Technology* **2010**, *44*, 1144-1151.

36. Griffitt, R. J.; Weil, R.; Hyndman, K. A.; Denslow, N. D.; Powers, K.; Taylor, D.; Barber, D. S. Exposure to copper nanoparticles causes gill injury and acute lethality

in zebrafish (*Danio rerio*). *Environmental Science & Technology* **2007**, *41*, 8178-8186.

37. Karlsson, H. L.; Cronholm, P.; Gustafsson, J.; Möller, L. Copper oxide nanoparticles are highly toxic: A comparison between metal oxide nanoparticles and carbon nanotubes. *Chemical Research in Toxicology* **2008**, *21*, 1726-1732.

38. Heinlaan, M.; Ivask, A.; Blinova, I.; Dubourguier, H.-C.; Kahru, A. Toxicity of nanosized and bulk ZnO, CuO and TiO_2 to bacteria *Vibrio fischeri* and crustaceans *Daphnia magna* and *Thamnocephalus platyuru*s. *Chemosphere* **2008**, *71*, 1308-1316.

39. Pettibone, J. M.; Adamcakova-Dodd, A.; Thorne, P. S.; O'Shaughnessy, P. T.; Weydert, J. A.; Grassian, V. H. Inflammatory response of mice following inhalation exposure to iron and copper nanoparticles. *Nanotoxicology* **2008**, *2*, 189-204.

40. Miller, R. J.; Lenihan, H. S.; Muller, E. B.; Tseng, N.; Hanna, S. K.; Keller, A. A. Impacts of metal oxide nanoparticles on marine phytoplankton. *Environmental Science & Technology* **2010**, *44*, 7329-7334.

41. Franklin, N. M.; Rogers, N. J.; Apte, S. C.; Batley, G. E.; Gadd, G. E.; Casey, P. S. Comparative toxicity of nanoparticulate ZnO, bulk ZnO, and $ZnCl_2$ to a freshwater microalga (*Pseudokirchneriella subcapitata*): The importance of particle solubility. *Environmental Science & Technology* **2007**, *41*, 8484-8490.

42. Quadros, M. E.; Marr, L. C. Environmental and human health risks of aerosolized silver nanoparticles. *Journal of the Air & Waste Management Association* **2010**, *60*, 770-781.

43. Carlson, C.; Hussain, S. M.; Schrand, A. M.; Braydich-Stolle, L. K.; Hess, K. L.; Jones, R. L.; Schlager, J. J. Unique cellular interaction of silver nanoparticles: Size-dependent generation of reactive oxygen species. *Journal of Physical Chemistry B* **2008**, *112*, 13608-13619.

44. Zheng, N.; Wang, H. J. Discovery of anatase in atmospheric inhalable particles and its significance. *Spectroscopy and Spectral Analysis* **2009**, *29*, 1570-1572.

45. Kaegi, R.; Ulrich, A.; Sinnet, B.; Vonbank, R.; Wichser, A.; Zuleeg, S.; Simmler, H.; Brunner, S.; Vonmont, H.; Burkhardt, M.; Boller, M. Synthetic TiO_2 nanoparticle emission from exterior facades into the aquatic environment. *Environmental Pollution* **2008**, *156*, 233-239.

46. Zhang, H. Z.; Penn, R. L.; Hamers, R. J.; Banfield, J. F. Enhanced adsorption of molecules on surfaces of nanocrystalline particles. *Journal of Physical Chemistry B* **1999**, *103*, 4656-4662.

47. Nagarajan, R.: Nanoparticles: Building blocks for nanotechnology. *Nanoparticles: Synthesis, Stabilization, Passivation, and Functionalization*; ACS Symposium Series; American Chemical Society, 2008; Vol. 996; pp 2-14.

48. Rao, C. N. R.; Kulkarni, G. U.; Thomas, P. J.; Edwards, P. P. Size-dependent chemistry: Properties of nanocrystals. *Chemistry – A European Journal* **2002**, *8*, 28-35.

49. Zhang, H.; Chen, B.; Banfield, J. F. Particle size and pH effects on nanoparticle dissolution. *The Journal of Physical Chemistry C* **2010**, *114*, 14876-14884.

50. Nützenadel, C.; Züttel, A.; Chartouni, D.; Schmid, G.; Schlapbach, L. Critical size and surface effect of the hydrogen interaction of palladium clusters. *The European Physical Journal D - Atomic, Molecular, Optical and Plasma Physics* **2000**, *8*, 245-250.

51. Grassian, V. H. When size really matters: Size-dependent properties and surface chemistry of metal and metal oxide nanoparticles in gas and liquid phase environments. *Journal of Physical Chemistry C* **2008**, *112*, 18303-18313.

52. Chopkar, M.; Sudarshan, S.; Das, P. K.; Manna, I. Effect of particle size on thermal conductivity of nanofluid. *Metallurgical and Materials Transactions A* **2008**, *39*, 1535-1542.

53. Comini, E.; Baratto, C.; Concina, I.; Faglia, G.; Falasconi, M.; Ferroni, M.; Galstyan, V.; Gobbi, E.; Ponzoni, A.; Vomiero, A.; Zappa, D.; Sberveglieri, V.; Sberveglieri, G. Metal oxide nanoscience and nanotechnology for chemical sensors. *Sensors and Actuators B-Chemical* **2013**, *179*, 3-20.

54. Enustun, B. V. T., J. Solubility of fine particles of strontium sulfate. *Journal of the American Chemical Society* **1960**, *82*, 4502.

55. Evans, J. W.; Thiel, P. A. A little chemistry helps the big get bigger. *Science* **2010**, *330*, 599-600.

56. Navrotsky, A.; Mazeina, L.; Majzlan, J. Size-driven structural and thermodynamic complexity in iron oxides. *Science* **2008**, *319*, 1635-1638.

57. Navrotsky, A. Energetics of oxide nanoparticles. *International Journal of Quantum Chemistry* **2009**, *109*, 2647-2657.

58. Radha, A. V.; Bomati-Miguel, O.; Ushakov, S. V.; Navrotsky, A.; Tartaj, P. Surface enthalpy, enthalpy of water adsorption, and phase stability in nanocrystalline monoclinic zirconia. *Journal of the American Ceramic Society* **2009**, *92,* 133-140.

59. Navrotsky, A.; Ma, C.; Lilova, K.; Birkner, N. Nanophase transition metal oxides show large thermodynamically driven shifts in oxidation-reduction equilibria. *Science* **2010**, *330*, 199-201.

60. Chen, C. H.; Yamaguchi, T.; Sugawara, K.; Koga, K. Role of stress in the self-limiting oxidation of copper nanoparticles. *Journal of Physical Chemistry B* **2005**, *109*, 20669-20672.

61. Zhang, P.; Xu, F.; Navrotsky, A.; Lee, J. S.; Kim, S.; Liu, J. Surface enthalpies of nanophase ZnO with different morphologies. *Chemistry of Materials* **2007**, *19*, 5687-5693.

62. Park, T.-J.; Levchenko, A. A.; Zhou, H.; Wong, S. S.; Navrotsky, A. Shape-dependent surface energetics of nanocrystalline TiO_2. *Journal of Materials Chemistry* **2010**, *20*, 8639-8645.

63. Fang, X.; Li, B.; Chernyshova, I. V.; Somasundaran, P. Ranking of as-received micro/nanoparticles by their surface energy values at ambient conditions. *The Journal of Physical Chemistry C* **2010**, *114*, 15473-15477.

64. Huang, W. J.; Sun, R.; Tao, J.; Menard, L. D.; Nuzzo, R. G.; Zuo, J. M. Coordination-dependent surface atomic contraction in nanocrystals revealed by coherent diffraction. *Nature Materials* **2008**, *7*, 308-313.

65. Gilbert, B.; Huang, F.; Zhang, H. Z.; Waychunas, G. A.; Banfield, J. F. Nanoparticles: Strained and stiff. *Science* **2004**, *305*, 651-654.

66. Gilbert, B.; Huang, F.; Lin, Z.; Goodell, C.; Zhang, H.; Banfield, J. F. Surface chemistry controls crystallinity of ZnS nanoparticles. *Nano Letters* **2006**, *6*, 605-610.

67. Bernhardt, E. S.; Colman, B. P.; Hochella, M. F., Jr.; Cardinale, B. J.; Nisbet, R. M.; Richardson, C. J.; Yin, L. An ecological perspective on nanomaterial impacts in the environment. *Journal of Environmental Quality* **2010**, *39*, 1954-1965.

68. Safi, M.; Courtois, J.; Seigneuret, M.; Conjeaud, H.; Berret, J. F. The effects of aggregation and protein corona on the cellular internalization of iron oxide nanoparticles. *Biomaterials* **2011**, *32*, 9353-9363.

69. Alkilany, A. M.; Nagaria, P. K.; Hexel, C. R.; Shaw, T. J.; Murphy, C. J.; Wyatt, M. D. Cellular uptake and cytotoxicity of gold nanorods: Molecular origin of cytotoxicity and surface effects. *Small* **2009**, *5*, 701-708.

70. Lin, D.; Xing, B. Root uptake and phytotoxicity of ZnO nanoparticles. *Environmental Science & Technology* **2008**, *42*, 5580-5585.

71. Delay, M.; Frimmel, F. H. Nanoparticles in aquatic systems. *Analytical and Bioanalytical Chemistry* **2012**, *402,* 583-592.

72. Lowry, G. V.; Gregory, K. B.; Apte, S. C.; Lead, J. R. Transformations of nanomaterials in the environment. *Environmental Science & Technology* **2012**, *46*, 6893-6899.

73. von der Kammer, F.; Ferguson, P. L.; Holden, P. A.; Masion, A.; Rogers, K. R.; Klaine, S. J.; Koelmans, A. A.; Horne, N.; Unrine, J. M. Analysis of engineered nanomaterials in complex matrices (environment and biota): General considerations and conceptual case studies. *Environmental Toxicology and Chemistry* **2012**, *31*, 32-49.

74. Bian, S.-W.; Mudunkotuwa, I. A.; Rupasinghe, T.; Grassian, V. H. Aggregation and dissolution of 4 nm ZnO nanoparticles in aqueous environments: Influence of pH, ionic strength, size, and adsorption of humic acid. *Langmuir* **2011**, *27*, 6059-6068.

75. Borm, P.; Klaessig, F. C.; Landry, T. D.; Moudgil, B.; Pauluhn, J.; Thomas, K.; Trottier, R.; Wood, S. Research strategies for safety evaluation of nanomaterials, Part V: Role of dissolution in biological fate and effects of nanoscale particles. *Toxicological Sciences* **2006**, *90*, 23-32.

76. Slingenbergh, W.; de Boer, S. K.; Cordes, T.; Browne, W. R.; Feringa, B. L.; Hoogenboom, J. P.; De Hosson, J. T. M.; van Dorp, W. F. Selective functionalization of tailored nanostructures. *ACS Nano* **2012**, *6*, 9214-9220.

77. Phenrat, T.; Saleh, N.; Sirk, K.; Kim, H.-J.; Tilton, R.; Lowry, G. Stabilization of aqueous nanoscale zerovalent iron dispersions by anionic polyelectrolytes: Adsorbed anionic polyelectrolyte layer properties and their effect on aggregation and sedimentation. *Journal of Nanoparticle Research* **2008**, *10*, 795-814.

78. Froimowicz, P.; Munoz-Espi, R.; Landfester, K.; Musyanovych, A.; Crespy, D. Surface-functionalized particles: From their design and synthesis to materials science and bio-applications. *Current Organic Chemistry* **2013**, *17*, 900-912.

79. Hakkinen, H. The Gold-sulfur interface at the nanoscale. *Nature Chemistry* **2012**, *4*, 443-455.

80. Lundqvist, M.; Stigler, J.; Cedervall, T.; Berggård, T.; Flanagan, M. B.; Lynch, I.; Elia, G.; Dawson, K. The evolution of the protein corona around nanoparticles: A test study. *ACS Nano* **2011**, *5*, 7503-7509.

81. Ma, Y.; Chechik, V. Aging of gold nanoparticles: Ligand exchange with disulfides. *Langmuir* **2011**, *27*, 14432-14437.

82. Tsai, D.-H.; Davila-Morris, M.; DelRio, F. W.; Guha, S.; Zachariah, M. R.; Hackley, V. A. Quantitative determination of competitive molecular adsorption on gold nanoparticles using attenuated total reflectance-fourier transform infrared spectroscopy. *Langmuir* **2011**, *27*, 9302-9313.

83. Tsai, D.-H.; DelRio, F. W.; Keene, A. M.; Tyner, K. M.; MacCuspie, R. I.; Cho, T. J.; Zachariah, M. R.; Hackley, V. A. Adsorption and conformation of serum albumin protein on gold nanoparticles investigated using dimensional measurements and *in situ* spectroscopic methods. *Langmuir* **2011**, *27*, 2464-2477.

84. Domingos, R. F.; Tufenkji, N.; Wilkinson, K. J. Aggregation of titanium dioxide nanoparticles: Role of a fulvic acid. *Environmental Science & Technology* **2009**, *43*, 1282-1286.

85. Tso, C. P.; Zhung, C. M.; Shih, Y. H.; Tseng, Y. M.; Wu, S. C.; Doong, R. A. stability of metal oxide nanoparticles in aqueous solutions. *Water Science and Technology* **2010**, *61*, 127-133.

86. Yang, K.; Lin, D. H.; Xing, B. S. Interactions of humic acid with nanosized inorganic oxides. *Langmuir* **2009**, *25*, 3571-3576.

87. Zhang, Y.; Chen, Y.; Westerhoff, P.; Crittenden, J. Impact of natural organic matter and divalent cations on the stability of aqueous nanoparticles. *Water Research* **2009**, *43*, 4249-4257.

88. Shemetov, A. A.; Nabiev, I.; Sukhanova, A. Molecular interaction of proteins and peptides with nanoparticles. *ACS Nano* **2012**, *6*, 4585-4602.

89. Stark, W. J. Nanoparticles in biological systems. *Angewandte Chemie-International Edition* **2011**, *50*, 1242-1258.

90. Casals, E.; Pfaller, T.; Duschl, A.; Oostingh, G. J.; Puntes, V. Time evolution of the nanoparticle protein corona. *ACS Nano* **2010**, *4*, 3623-3632.

91. Di Felice, R.; Corni, S. Simulation of peptide-surface recognition. *Journal of Physical Chemistry Letters* **2011**, *2*, 1510-1519.

92. Mahmoudi, M.; Lynch, I.; Ejtehadi, M. R.; Monopoli, M. P.; Bombelli, F. B.; Laurent, S. Protein-nanoparticle interactions: Opportunities and challenges. *Chemical Reviews* **2011**, *111*, 5610-5637.

93. Moyano, D. F.; Rotello, V. M. Nano meets biology: Structure and function at the nanoparticle interface. *Langmuir* **2011**, *27*, 10376-10385.

94. Selvakannan, P. R.; Mandal, S.; Phadtare, S.; Pasricha, R.; Sastry, M. Capping of gold nanoparticles by the amino acid lysine renders them water-dispersible. *Langmuir* **2003**, *19*, 3545-3549.

95. Zhao, L.; Peralta-Videa, J. R.; Varela-Ramirez, A.; Castillo-Michel, H.; Li, C.; Zhang, J.; Aguilera, R. J.; Keller, A. A.; Gardea-Torresdey, J. L. Effect of surface coating and organic matter on the uptake of CeO_2 NPs by corn plants grown in soil: Insight into the uptake mechanism. *Journal of Hazardous Materials* **2012**, *225-226*, 131-138.

96. Caracciolo, G.; Callipo, L.; De Sanctis, S. C.; Cavaliere, C.; Pozzi, D.; Laganà , A. Surface adsorption of protein corona controls the cell internalization mechanism of DC-Chol-DOPE/DNA lipoplexes in serum. *Biochimica et Biophysica Acta (BBA) - Biomembranes* **2010**, *1798*, 536-543.

97. Raghupathi, K. R.; Koodali, R. T.; Manna, A. C. Size-dependent bacterial growth inhibition and mechanism of antibacterial activity of zinc oxide nanoparticles. *Langmuir* **2011**, *27,* 4020-4028.

98. Rivera Gil, P.; Oberdörster, G. n.; Elder, A.; Puntes, V. c.; Parak, W. J. Correlating physico-chemical with toxicological properties of nanoparticles: The present and the future. *ACS Nano* **2010**, *4,* 5527-5531.

99. Stebounova, L.; Guio, E.; Grassian, V. Silver nanoparticles in simulated biological media: A study of aggregation, sedimentation, and dissolution. *Journal of Nanoparticle Research* **2010**, 1-12.

100. Elzey, S.; Grassian, V. H. Nanoparticle dissolution from the particle perspective: Insights from particle sizing measurements. *Langmuir* **2010**, *26*, 12505-12508.

101. Mudunkotuwa, I. A.; Grassian, V. H. The devil is in the details (or the surface): Impact of surface structure and surface energetics on understanding the behavior of nanomaterials in the environment. *Journal of Environmental Monitoring* **2011**, *13,* 1135-1144.

102. Rubasinghege, G.; Lentz, R. W.; Park, H.; Scherer, M. M.; Grassian, V. H. Nanorod dissolution quenched in the aggregated state. *Langmuir* **2009**, *26,* 1524-1527.

103. Liu, J.; Aruguete, D. M.; Jinschek, J. R.; Donald Rimstidt, J.; Hochella Jr, M. F. The non-oxidative dissolution of galena nanocrystals: Insights into mineral dissolution rates as a function of grain size, shape, and aggregation state. *Geochimica et Cosmochimica Acta* **2008**, *72,* 5984-5996.

104. Hibara, A.; Saito, T.; Kim, H.-B.; Tokeshi, M.; Ooi, T.; Nakao, M.; Kitamori, T. Nanochannels on a fused-silica microchip and liquid properties investigation by time-resolved fluorescence measurements. *Analytical Chemistry* **2002**, *74,* 6170-6176.

105. Liu, J.; Aruguete, D. M.; Murayama, M.; Hochella, M. F. Influence of size and aggregation on the reactivity of an environmentally and industrially relevant nanomaterial (PbS). *Environmental Science & Technology* **2009**, *43,* 8178-8183.

106. Tang, R.; Wang, L.; Nancollas, G. H. Size-effects in the Dissolution of Hydroxyapatite: An understanding of biological demineralization. *Journal of Materials Chemistry* **2004**, *14,* 2341-2346.

107. Schmidt, J.; Vogelsberger, W. Dissolution kinetics of titanium dioxide nanoparticles: The observation of an unusual kinetic size effect. *Journal of Physical Chemistry B* **2006**, *110,* 3955-3963.

108. Erbs, J. J.; Gilbert, B.; Penn, R. L. Influence of size on reductive dissolution of six-line ferrihydrite. *The Journal of Physical Chemistry C* **2008**, *112*, 12127-12133.

109. Tsukahara, T.; Hibara, A.; Ikeda, Y.; Kitamori, T. NMR study of water molecules confined in extended nanospaces. *Angewandte Chemie International Edition* **2007**, *46*, 1180-1183.

110. Keller, A. A.; Wang, H.; Zhou, D.; Lenihan, H. S.; Cherr, G.; Cardinale, B. J.; Miller, R.; Ji, Z. Stability and aggregation of metal oxide nanoparticles in natural aqueous matrices. *Environmental Science & Technology* **2010**, *44*, 1962-1967.

111. Suttiponparnit, K.; Jiang, J.; Sahu, M.; Suvachittanont, S.; Charinpanitkul, T.; Biswas, P. Role of surface area, primary particle size, and crystal phase on titanium dioxide nanoparticle dispersion properties. *Nanoscale Research Letters* **2010**, 1-8.

112. French, R. A.; Jacobson, A. R.; Kim, B.; Isley, S. L.; Penn, R. L.; Baveye, P. C. Influence of ionic strength, pH, and cation valence on aggregation kinetics of titanium dioxide nanoparticles. *Environmental Science & Technology* **2009**, *43*, 1354-1359.

113. Domingos, R. F.; Baalousha, M. A.; Ju-Nam, Y.; Reid, M. M.; Tufenkji, N.; Lead, J. R.; Leppard, G. G.; Wilkinson, K. J. Characterizing manufactured nanoparticles in the environment: Multimethod determination of particle sizes. *Environmental Science & Technology* **2009**, *43,* 7277-7284.

114. Guzman, K. A. D.; Finnegan, M. P.; Banfield, J. F. Influence of surface potential on aggregation and transport of titania nanoparticles. *Environmental Science & Technology* **2006**, *40*, 7688-7693.

115. Petosa, A. R.; Jaisi, D. P.; Quevedo, I. R.; Elimelech, M.; Tufenkji, N. Aggregation and deposition of engineered nanomaterials in aquatic environments: Role of physicochemical interactions. *Environmental Science & Technology* **2010**, *44*, 6532-6549.

116. Abbas, Z.; Labbez, C.; Nordholm, S.; Ahlberg, E. Size-dependent surface charging of nanoparticles. *The Journal of Physical Chemistry C* **2008**, *112*, 5715-5723.

117. Jolivet, J.-P.; Froidefond, C.; Pottier, A.; Chaneac, C.; Cassaignon, S.; Tronc, E.; Euzen, P. Size tailoring of oxide nanoparticles by precipitation in aqueous medium. A semi-quantitative modelling. *Journal of Materials Chemistry* **2004**, *14,* 3281-3288.

118. Li, X.; Lenhart, J. J.; Walker, H. W. Dissolution-accompanied aggregation kinetics of silver nanoparticles. *Langmuir* **2010**, *26*, 16690-16698.

119. Elzey, S.; Grassian, V. H. Agglomeration, isolation and dissolution of commercially manufactured silver nanoparticles in aqueous environments. *Journal of Nanoparticle Research* **2010**, *12*, 1945-1958.

120. Romero-Cano, M. S.; Martín-Rodríguez, A.; de las Nieves, F. J. Electrosteric stabilization of polymer colloids with different functionality. *Langmuir* **2001**, *17*, 3505-3511.

121. Lindvig, T.; Michelsen, M. L.; Kontogeorgis, G. M. A Flory-Huggins model based on the Hansen solubility parameters. *Fluid Phase Equilibria* **2002**, *203*, 247-260.

122. Shah, P. S.; Holmes, J. D.; Johnston, K. P.; Korgel, B. A. Size-selective dispersion of dodecanethiol-coated nanocrystals in liquid and supercritical ethane by density tuning. *The Journal of Physical Chemistry B* **2002**, *106*, 2545-2551.

123. Klaine, S. J.; Alvarez, P. J. J.; Batley, G. E.; Fernandes, T. F.; Handy, R. D.; Lyon, D. Y.; Mahendra, S.; McLaughlin, M. J.; Lead, J. R. Nanomaterials in the environment: Behavior, fate, bioavailability, and effects. *Environmental Toxicology and Chemistry* **2008**, *27*, 1825-1851.

124. Boncagni, N. T.; Otaegui, J. M.; Warner, E.; Curran, T.; Ren, J. H.; De Cortalezzi, M. M. F. Exchange of TiO_2 nanoparticles between streams and streambeds. *Environmental Science & Technology* **2009**, *43*, 7699-7705.

125. Borm, P. J. A.; Robbins, D.; Haubold, S.; Kuhlbusch, T.; Fissan, H.; Donaldson, K.; Schins, R.; Stone, V.; Kreyling, W.; Lademann, J.; Krutmann, J.; Warheit, D.; Oberdorster, E. The potential risks of nanomaterials: A review carried out for ECETOC. *Particle and Fibre Toxicology* **2006**, *3*, 11.

126. Hamers, R. J.; Wang, X.; Franking, R.; Ruther, R.; Stavis, C.; Chabal, C. M. P. A. Y. J.: Chapter 3 - Infrared spectroscopy for characterization of biomolecular interfaces. *Biointerface Characterization by Advanced IR Spectroscopy*; Elsevier: Amsterdam, 2011; pp 57-82.

127. Hase, M.; Scheffelmaier, R.; Hayden, S.; Rivera, D. Quantitative *in situ* attenuated total internal reflection Fourier transform infrared study of the isotherms of poly(sodium 4-styrene sulfonate) adsorption to a TiO_2 surface over a range of cetylpyridinium bromide monohydrate concentration. *Langmuir* **2010**, *26*, 5534-5543.

128. Ojea-Jimenez, I.; Puntes, V. Instability of cationic gold nanoparticle bioconjugates: The role of citrate ions. *Journal of the American Chemical Society* **2009**, *132*, 5322-5322.

129. Xue, C.; Metraux, G. S.; Millstone, J. E.; Mirkin, C. A. Mechanistic study of photomediated triangular silver nanoprism growth. *Journal of the American Chemical Society* **2008**, *130*, 8337-8344.

130. Ji, X. H.; Song, X. N.; Li, J.; Bai, Y. B.; Yang, W. S.; Peng, X. G. Size control of gold nanocrystals in citrate reduction: The third role of citrate. *Journal of the American Chemical Society* **2007**, *129*, 13939-13948.

131. Ozkar, S.; Finke, R. G. Nanocluster formation and stabilization fundamental studies: Ranking commonly employed anionic stabilizers via the development, then application, of five comparative criteria. *Journal of the American Chemical Society* **2002**, *124*, 5796-5810.

132. Yin, H. B.; Wada, Y.; Kitamura, T.; Sumida, T.; Hasegawa, Y.; Yanagida, S. Novel synthesis of phase-pure nano-particulate anatase and rutile TiO_2 using $TiCl_4$ aqueous solutions. *Journal of Materials Chemistry* **2002**, *12*, 378-383.

133. Liu, Y.; Liu, C. Y.; Zhang, Z. Y. Effects of carboxylic acids on the microstructure and performance of titania nanocrystals. *Chemical Engineering Journal* **2008**, *138*, 596-601.

134. Dakanali, M.; Raptopoulou, C. P.; Terzis, A.; Lakatos, A.; Banyai, I.; Kiss, T.; Salifogiou, A. A novel dinuclear species in the aqueous distribution of aluminum in the presence of citrate. *Inorganic Chemistry* **2003**, *42*, 252-254.

135. Huang, P. M.; Wang, M. K.; Chiu, C. Y. Soil mineral-organic matter-microbe interactions: Impacts on biogeochemical processes and biodiversity in soils. *Pedobiologia* **2005**, *49*, 609-635.

136. Kubicki, J. D.; Schroeter, L. M.; Itoh, M. J.; Nguyen, B. N.; Apitz, S. E. Attenuated total reflectance fourier-transform infrared spectroscopy of carboxylic acids adsorbed onto mineral surfaces. *Geochimica Et Cosmochimica Acta* **1999**, *63*, 2709-2725.

137. Lackovic, K.; Johnson, B. B.; Angove, M. J.; Wells, J. D. Modeling the adsorption of citric acid onto Muloorina illite and related clay minerals. *Journal of Colloid and Interface Science* **2003**, *267*, 49-59.

138. Lindegren, M.; Loring, J. S.; Persson, P. Molecular structures of citrate and tricarballylate adsorbed on α-FeOOH particles in aqueous suspensions. *Langmuir* **2009**, *25*, 10639-10647.

139. Grassian, V. H.; O'Shaughnessy, P. T.; Adamcakova-Dodd, A.; Pettibone, J. M.; Thorne, P. S. Inhalation exposure study of titanium dioxide nanoparticles with a primary particle size of 2 to 5 nm. *Environmental Health Perspectives* **2007**, *115*, 397-402.

140. Pirmin, C. H.; Thomas, J. G.; Ludwig, J. G. Citric acid;A dispersant for aqueous alumina suspensions. *Journal of the American Ceramic Society* **1996**, *79*, 1857-1867.

141. Johnson, S. B.; Yoon, T. H.; Slowey, A. J.; Brown, G. E. Adsorption of organic matter at mineral/water interfaces: 3. Implications of surface dissolution for adsorption of oxalate. *Langmuir* **2004**, *20*, 11480-11492.

142. Hug, S. J.; Bahnemann, D. Infrared spectra of oxalate, malonate and succinate adsorbed on the aqueous surface of rutile, anatase and lepidocrocite measured with *in situ* ATR-FTIR. *Journal of Electron Spectroscopy and Related Phenomena* **2006**, *150*, 208-219.

143. Ojamae, L.; Aulin, C.; Pedersen, H.; Kall, P. O. IR and Quantum-chemical studies of carboxylic acid and glycine adsorption on rutile TiO_2 nanoparticles. *Journal of Colloid and Interface Science* **2006**, *296*, 71-78.

144. Max, J. J.; Chapados, C. Infrared spectroscopy of aqueous carboxylic acids: Comparison between different acids and their salts. *Journal of Physical Chemistry A* **2004**, *108*, 3324-3337.

145. Borer, P.; Hug, S. J.; Sulzberger, B.; Kraemer, S. M.; Kretzschmar, R. Photolysis of citrate on the surface of lepidocrocite: An in situ attenuated total reflection infrared spectroscopy study. *Journal of Physical Chemistry C* **2007**, *111*, 10560-10569.

146. Pasilis, S. P.; Pemberton, J. E. Spectroscopic investigation of uranyl(VI) and citrate coadsorption to Al_2O_3. *Geochimica Et Cosmochimica Acta* **2008**, *72*, 277-287.

147. Martyanov, I. N.; Savinov, E. N.; Klabunde, K. J. Influence of solution composition and ultrasonic treatment on optical spectra of TiO_2 aqueous suspensions. *Journal of Colloid and Interface Science* **2003**, *267*, 111-116.

148. Pettibone, J. M.; Cwiertny, D. M.; Scherer, M.; Grassian, V. H. Adsorption of organic acids on TiO_2 nanoparticles: Effects of pH, nanoparticle size, and nanoparticle aggregation. *Langmuir* **2008**, *24*, 6659-6667.

149. Sharma, V. K. Aggregation and toxicity of titanium dioxide nanoparticles in aquatic environments"A Review. *Journal of Environmental Science and Health, Part A: Toxic/Hazardous Substances and Environmental Engineering* **2009**, *44*, 1485 - 1495.

150. Hadjiivanov, K. I.; Klissurski, D. G. Surface chemistry of titania (anatase) and titania-supported catalysts. *Chemical Society Reviews* **1996**, *25*, 61-&.

151. Chen, H.; Nanayakkara, C. E.; Grassian, V. H. Titanium dioxide photocatalysis in atmospheric chemistry. *Chemical Reviews* **2012**, *112*, 5919-5948.

152. Ridley, M. K.; Hackley, V. A.; Machesky, M. L. Characterization and surface-reactivity of nanocrystalline anatase in aqueous solutions. *Langmuir* **2006**, *22*, 10972-10982.

153. Lee, J.; Mahendra, S.; Alvarez, P. J. J. Nanomaterials in the construction industry: A review of their applications and environmental health and safety considerations. *ACS Nano* **2010**, *4*, 3580-3590.

154. Zhou, W.; Han, Z.; Wang, J.; Zhang, Y.; Jin, Z.; Sun, X.; Zhang, Y.; Yan, C.; Li, Y. Copper catalyzing growth of single-walled carbon nanotubes on substrates. *Nano Letters* **2006**, *6*, 2987-2990.

155. Taberna, P. L.; Mitra, S.; Poizot, P.; Simon, P.; Tarascon, J. M. High rate capabilities Fe_3O_4-based Cu nano-architectured electrodes for lithium-ion battery applications. *Nature Materials* **2006**, *5*, 567-573.

156. Li, X.; Zhu, D.; Wang, X. Experimental investigation on viscosity of Cu-H_2O nanofluids. *Journal of Wuhan University of Technology--Materials Science Edition* **2009**, *24*, 48-52.

157. Nair, M. T. S.; Guerrero, L.; Arenas, O. L.; Nair, P. K. Chemically deposited copper oxide thin films: structural, optical and electrical characteristics. *Applied Surface Science* **1999**, *150*, 143-151.

158. Salavati-Niasari, M.; Davar, F.; Mir, N. Synthesis and characterization of metallic copper nanoparticles via thermal decomposition. *Polyhedron* **2008**, *27*, 3514-3518.

159. Yin, M.; Wu, C.-K.; Lou, Y.; Burda, C.; Koberstein, J. T.; Zhu, Y.; O'Brien, S. Copper oxide nanocrystals. *Journal of the American Chemical Society* **2005**, *127*, 9506-9511.

160. Wang, X.; Zhang, F.; Xia, B.; Zhu, X.; Chen, J.; Qiu, S.; Zhang, P.; Li, J. Controlled modification of multi-walled carbon nanotubes with CuO, Cu_2O and Cu nanoparticles. *Solid State Sciences* **2009**, *11*, 655-659.

161. Boccuzzi, F.; Chiorino, A.; Manzoli, M.; Andreeva, D.; Tabakova, T.; Ilieva, L.; Iadakiev, V. Gold, silver and copper catalysts supported on TiO_2 for pure hydrogen production. *Catalysis Today* **2002**, *75*, 169-175.

162. Mailänder, V.; Landfester, K. Interaction of nanoparticles with cells. *Biomacromolecules* **2009**, *10*, 2379-2400.

163. Liang, M.; Lin, I. C.; Whittaker, M. R.; Minchin, R. F.; Monteiro, M. J.; Toth, I. Cellular uptake of densely packed polymer coatings on gold nanoparticles. *ACS Nano* **2009**, *4*, 403-413.

164. Schrand, A. M.; Rahman, M. F.; Hussain, S. M.; Schlager, J. J.; Smith, D. A.; Syed, A. F. Metal-based nanoparticles and their toxicity assessment. *Wiley Interdisciplinary Reviews: Nanomedicine and Nanobiotechnology* **2010**, *2*, 544-568.

165. Pan, Z.; Tao, J.; Zhu, Y.; Huang, J.-F.; Paranthaman, M. P. Spontaneous growth of $ZnCO_3$ nanowires on ZnO nanostructures in normal ambient environment: Unstable ZnO nanostructures. *Chemistry of Materials* **2009**, *22*, 149-154.

166. Slowey, A. J.; Johnson, S. B.; Rytuba, J. J.; Brown, G. E. Role of organic acids in promoting colloidal transport of mercury from mine tailings. *Environmental Science & Technology* **2005**, *39*, 7869-7874.

167. Furrer, G.; Stumm, W. The coordination chemistry of weathering: I. Dissolution kinetics of δ-Al_2O_3 and BeO. *Geochimica et Cosmochimica Acta* **1986**, *50*, 1847-1860.

168. Johnson, S. B.; Brown, G. E.; Healy, T. W.; Scales, P. J. Adsorption of organic matter at mineral/water interfaces. 6. Effect of inner-sphere versus outer-sphere adsorption on colloidal stability. *Langmuir* **2005**, *21*, 6356-6365.

169. Di Palma, L.; Mecozzi, R. Heavy metals mobilization from harbour sediments using EDTA and citric acid as chelating agents. *Journal of Hazardous Materials* **2007**, *147*, 768-775.

170. Nybroe, O.; Brandt, K. K.; Ibrahim, Y. M.; Tom-Petersen, A.; Holm, P. E. Differential bioavailability of copper complexes to bioluminescent Pseudomonas fluorescens reporter strains. *Environmental Toxicology and Chemistry* **2008**, *27*, 2246-2252.

171. Maketon, W.; Ogden, K. L. Synergistic effects of citric acid and polyethyleneimine to remove copper from aqueous solutions. *Chemosphere* **2009**, *75*, 206-211.

172. Chen, J.-H.; Huang, C.-E. Selective separation of Cu and Zn in the citric acid leachate of industrial printed wiring board sludge by D2EHPA-modified amberlite XAD-4 resin. *Industrial & Engineering Chemistry Research* **2007**, *46*, 7231-7238.

173. Subramanian, T.; Wayne, H.; Srini, R.; Robert, S. Potential-pH diagrams of interest to chemical mechanical planarization of copper. *Journal of The Electrochemical Society* **2002**, *149*, G638-G642.

174. Mudunkotuwa, I. A.; Grassian, V. H. Citric acid adsorption on TiO_2 nanoparticles in aqueous suspensions at acidic and circumneutral pH: Surface coverage, surface speciation, and its impact on nanoparticle-nanoparticle interactions. *Journal of the American Chemical Society* **2010**, *132*, 14986-14994.

175. Baltrusaitis, J.; Cwiertny, D. M.; Grassian, V. H. Adsorption of sulfur dioxide on hematite and goethite particle surfaces. *Physical Chemistry Chemical Physics* **2007**, *9*, 5542-5554.

176. Wu, C.-K.; Yin, M.; O'Brien, S.; Koberstein, J. T. Quantitative analysis of copper oxide nanoparticle composition and structure by X-ray photoelectron spectroscopy. *Chemistry of Materials* **2006**, *18*, 6054-6058.

177. Shchukarev, A.; Korolkov, D. XPS study of group IA carbonates. *Central European Journal of Chemistry* **2004**, *2*, 347-362.

178. Miller, D. J.; Biesinger, M. C.; McIntyre, N. S. Interactions of CO_2 and CO at fractional atmosphere pressures with iron and iron oxide surfaces: one possible mechanism for surface contamination? *Surface and Interface Analysis* **2002**, *33*, 299-305.

179. Magdassi, S.; Grouchko, M.; Berezin, O.; Kamyshny, A. Triggering the sintering of silver nanoparticles at room temperature. *ACS Nano* **2010**, *4*, 1943-1948.

180. Grouchko, M.; Popov, I.; Uvarov, V.; Magdassi, S.; Kamyshny, A. Coalescence of silver nanoparticles at room temperature: Unusual crystal structure transformation and dendrite formation induced by self-assembly. *Langmuir* **2009**, *25*, 2501-2503.

181. Duckworth, O. W.; Martin, S. T. Surface complexation and dissolution of hematite by C1-C6 dicarboxylic acids at pH = 5.0. *Geochimica et Cosmochimica Acta* **2001**, *65*, 4289-4301.

182. Degenhardt, J.; McQuillan, A. J. Mechanism of oxalate ion adsorption on chromium oxide-hydroxide from pH dependence and time evolution of ATR-IR spectra. *Chemical Physics Letters* **1999**, *311*, 179-184.

183. Hug, S. J.; Sulzberger, B. *In situ* Fourier transform infrared spectroscopic evidence for the formation of several different surface complexes of oxalate on TiO_2 in the aqueous phase. *Langmuir* **1994**, *10*, 3587-3597.

184. Elzey, S.; Baltrusaitis, J.; Bian, S.; Grassian, V. H. Formation of paratacamite nanomaterials via the conversion of aged and oxidized copper nanoparticles in hydrochloric acidic media. *Journal of Materials Chemistry* **2010**, *21*, 3162-3169.

185. Harveth, G.; Christofer, L. Quantitative *in situ* analysis of initial atmospheric corrosion of copper induced by acetic acid. *Journal of The Electrochemical Society* **2007**, *154*, C272-C278.

186. Abdullah, S.; Abdullah, M. F.; Ariffin, A. K.; Jalar, A. Effect of leadframe oxidation on the reliability of a quad flat no-lead package. *Journal of Electronic Packaging* **2009**, *131*, 031002.

187. Axe, K.; Persson, P. Time-dependent surface speciation of oxalate at the water-boehmite (γ-AlOOH) interface: implications for dissolution. *Geochimica et Cosmochimica Acta* **2001**, *65*, 4481-4492.

188. Sabine, R.; Christophe, H.; Cecile, V.; Michael, M. Complexation chemistry in copper plating from citrate baths. *Journal of The Electrochemical Society* **2004**, *151*, C405-C411.

189. Connor, E. E.; Mwamuka, J.; Gole, A.; Murphy, C. J.; Wyatt, M. D. Gold nanoparticles are taken up by human cells but do not cause acute cytotoxicity. *Small* **2005**, *1*, 325-327.

190. Maysinger, D. Nanoparticles and cells: good companions and doomed partnerships. *Organic & Biomolecular Chemistry* **2007**, *5*, 2335-2342.

191. Chen, Z.; Meng, H.; Xing, G.; Chen, C.; Zhao, Y.; Jia, G.; Wang, T.; Yuan, H.; Ye, C.; Zhao, F.; Chai, Z.; Zhu, C.; Fang, X.; Ma, B.; Wan, L. Acute toxicological effects of copper nanoparticles in vivo. *Toxicology Letters* **2006**, *163*, 109-120.

192. Gunawan, C.; Teoh, W. Y.; Marquis, C. P.; Amal, R. Cytotoxic origin of copper(II) oxide nanoparticles: Comparative studies with micron-sized particles, leachate, and metal Salts. *ACS Nano* **2011**, *5(9)*, 7214-7225.

193. Baek, Y.-W.; An, Y.-J. Microbial toxicity of metal oxide nanoparticles (CuO, NiO, ZnO, and Sb_2O_3) to *Escherichia coli*, *Bacillus subtilis*, and *Streptococcus aureus. Science of The Total Environment* **2011**, *409*, 1603-1608.

194. Brayner, R.; Ferrari-Iliou, R.; Brivois, N.; Djediat, S.; Benedetti, M. F.; Fiévet, F. Toxicological impact studies based on *Escherichia coli* bacteria in ultrafine ZnO nanoparticles colloidal medium. *Nano Letters* **2006**, *6*, 866-870.

195. Zhang, Y.; Chen, Y.; Westerhoff, P.; Hristovski, K.; Crittenden, J. C. Stability of commercial metal oxide nanoparticles in water. *Water Research* **2008**, *42*, 2204-2212.

196. Tiede, K.; Hassellöv, M.; Breitbarth, E.; Chaudhry, Q.; Boxall, A. B. A. Considerations for environmental fate and ecotoxicity testing to support environmental risk assessments for engineered nanoparticles. *Journal of Chromatography A* **2009**, *1216*, 503-509.

197. Zhao, Q.; Xie, T.; Peng, L.; Lin, Y.; Wang, P.; Peng, L.; Wang, D. Size and orientation-dependent photovoltaic properties of ZnO nanorods. *The Journal of Physical Chemistry C* **2007**, *111*, 17136-17145.

198. Chen, M. S.; Goodman, D. W. The structure of catalytically active gold on titania. *Science* **2004**, *306*, 252-255.

199. Meier, D. C.; Goodman, D. W. The influence of metal cluster size on adsorption energies: CO adsorbed on Au clusters supported on TiO_2. *Journal of the American Chemical Society* **2004**, *126*, 1892-1899.

200. Van Eerdenbrugh, B.; Vermant, J.; Martens, J. A.; Froyen, L.; Humbeeck, J. V.; Van den Mooter, G.; Augustijns, P. Solubility increases associated with crystalline drug nanoparticles: Methodologies and significance. *Molecular Pharmaceutics* **2010**, *7*, 1858-1870.

201. Letellier, P. M., A.; Turmine, M. . Solubility of nanoparticles: nonextensive thermodynamics approach. *Journal of Physics: Condensed Matter* **2007**, *19*, 496229.

202. Meulenkamp, E. A. Size dependence of the dissolution of ZnO nanoparticles. *The Journal of Physical Chemistry B* **1998**, *102*, 7764-7769.

203. Dundon, M. L. M., E. . The solubilty and surface energy of calcium sulfate *Journal the American Chemical Socity* **1923**, *45*, 2658.

204. Mihranyan, A.; Strømme, M. Solubility of fractal nanoparticles. *Surface Science* **2007**, *601*, 315-319.

205. Zhou, D. X.; Keller, A. A. Role of morphology in the aggregation kinetics of ZnO nanoparticles. *Water Research* **2010**, *44*, 2948-2956.

206. Peng, X.; Palma, S.; Fisher, N. S.; Wong, S. S. Effect of morphology of ZnO nanostructures on their toxicity to marine algae. *Aquatic Toxicology* **2011**, *102*, 186-196.

207. Hu, Z.; Oskam, G.; Searson, P. C. Influence of solvent on the growth of ZnO nanoparticles. *Journal of Colloid and Interface Science* **2003**, *263*, 454-460.

208. Brayner, R.; Dahoumane, S. A.; Yéprémian, C.; Djediat, C.; Meyer, M. l.; Couté, A.; Fiévet, F. ZnO nanoparticles: Synthesis, characterization, and ecotoxicological studies. *Langmuir* **2010**, *26*, 6522-6528.

209. Song, W. H.; Zhang, J. Y.; Guo, J.; Zhang, J. H.; Ding, F.; Li, L. Y.; Sun, Z. T. Role of the dissolved zinc ion and reactive oxygen species in cytotoxicity of ZnO nanoparticles. *Toxicol. Lett.* **2010**, *199*, 389-397.

210. Adams, L. K.; Lyon, D. Y.; Alvarez, P. J. J. Comparative eco-toxicity of nanoscale TiO_2, SiO_2, and ZnO water suspensions. *Water Research* **2006**, *40*, 3527-3532.

211. Poynton, H. C.; Lazorchak, J. M.; Impellitteri, C. A.; Smith, M. E.; Rogers, K.; Patra, M.; Hammer, K. A.; Allen, H. J.; Vulpe, C. D. Differential gene expression in *Daphnia magna* suggests distinct modes of action and bioavailability for ZnO nanoparticles and Zn ions. *Environmental Science & Technology* **2011**, *45*, 762-768.

212. Li, M.; Zhu, L.; Lin, D. Toxicity of ZnO nanoparticles to *Escherichia coli*: Mechanism and the influence of medium components. *Environmental Science & Technology* **2011**, *45*, 1977-1983.

213. Wu, C.-M.; Baltrusaitis, J.; Gillan, E. G.; Grassian, V. H. Sulfur dioxide adsorption on ZnO nanoparticles and nanorods. *The Journal of Physical Chemistry C* **2011**.

214. Lu, J.; Ng, K. M.; Yang, S. Efficient, one-step mechanochemical process for the synthesis of ZnO nanoparticles. *Industrial & Engineering Chemistry Research* **2008**, *47*, 1095-1101.

215. Joshi-Tope, G.; Francis, A. J. Mechanisms of biodegradation of metal-citrate complexes by Pseudomonas fluorescens. *J. Bacteriol.* **1995**, *177*, 1989-1993.

216. Degen, A.; Kosec, M. Effect of pH and impurities on the surface charge of zinc oxide in aqueous solution. *Journal of the European Ceramic Society* **2000**, *20*, 667-673.

217. Yamabi, S.; Imai, H. Growth conditions for wurtzite zinc oxide films in aqueous solutions. *Journal of Materials Chemistry* **2002**, *12*, 3773-3778.

218. Harbury, L. Solubility and melting point as functions of particle size. *Journal of Physical Chemistry* **1946**, *50*, 190-199.

219. Valtiner, M.; Borodin, S.; Grundmeier, G. Stabilization and acidic dissolution mechanism of single-crystalline ZnO(0001) surfaces in electrolytes studied by *in-situ* AFM imaging and *ex-situ* LEED. *Langmuir* **2008**, *24*, 5350-5358.

220. Moghimi, S. M.; Hunter, A. C.; Murray, J. C. Nanomedicine: current status and future prospects. *Faseb Journal* **2005**, *19*, 311-330.

221. Joshi, S.; Ghosh, I.; Pokhrel, S.; Mädler, L.; Nau, W. M. Interactions of amino acids and polypeptides with metal oxide nanoparticles probed by fluorescent indicator adsorption and displacement. *ACS Nano* **2012**, *6*, 5668-5679.

222. Tenzer, S.; Docter, D.; Rosfa, S.; Wlodarski, A.; Kuharev, J.; Rekik, A.; Knauer, S. K.; Bantz, C.; Nawroth, T.; Bier, C.; Sirirattanapan, J.; Mann, W.; Treuel, L.; Zellner, R.; Maskos, M.; Schild, H.; Stauber, R. H. Nanoparticle size is a critical physicochemical determinant of the human blood plasma corona: A comprehensive quantitative proteomic analysis. *ACS Nano* **2011***5*, 7155-7167.

223. Barrán-Berdön, A. L.; Pozzi, D.; Caracciolo, G.; Capriotti, A. L.; Caruso, G.; Cavaliere, C.; Riccioli, A.; Palchetti, S.; Laganà , A. Time evolution of nanoparticle-protein corona in human plasma: Relevance for targeted drug delivery. *Langmuir* **2013**, *29*, 6485-6494.

224. Monteiro-Riviere, N. A.; Samberg, M. E.; Oldenburg, S. J.; Riviere, J. E. Protein binding modulates the cellular uptake of silver nanoparticles into human cells: Implications for *in vitro* to *in vivo* extrapolations? *Toxicology Letters* **2013**, *220*, 286-293.

225. Monopoli, M. P.; Walczyk, D.; Campbell, A.; Elia, G.; Lynch, I.; Baldelli Bombelli, F.; Dawson, K. A. Physical-chemical aspects of protein corona: Relevance to *in vitro* and *in vivo* biological impacts of nanoparticles. *Journal of the American Chemical Society* **2011**, *133*, 2525-2534.

226. Lundqvist, M.; Stigler, J.; Elia, G.; Lynch, I.; Cedervall, T.; Dawson, K. A. Nanoparticle size and surface properties determine the protein corona with possible

implications for biological impacts. *Proceedings of the National Academy of Sciences* **2008**, *105*, 14265-14270.

227. Walkey, C. D.; Chan, W. C. W. Understanding and controlling the interaction of nanomaterials with proteins in a physiological environment. *Chemical Society Reviews* **2012**, *41*, 2780-2799.

228. Pan, H.; Qin, M.; Meng, W.; Cao, Y.; Wang, W. How do proteins unfold upon adsorption on nanoparticle surfaces? *Langmuir* **2012**, *28*, 12779-12787.

229. Wang, D.; Nap, R. J.; Lagzi, I.; Kowalczyk, B.; Han, S.; Grzybowski, B. A.; Szleifer, I. How and why nanoparticle's curvature regulates the apparent pK_a of the coating ligands. *Journal of the American Chemical Society* **2011**, *133*, 2192-2197.

230. Podila, R.; Vedantam, P.; Ke, P. C.; Brown, J. M.; Rao, A. M. Evidence for charge-transfer-induced conformational changes in carbon Nanostructure-Protein Corona. *The Journal of Physical Chemistry C* **2012**, *116*, 22098-22103.

231. Schaefer, J.; Schulze, C.; Marxer, E. E. J.; Schaefer, U. F.; Wohlleben, W.; Bakowsky, U.; Lehr, C.-M. Atomic force microscopy and analytical ultracentrifugation for probing nanomaterial protein interactions. *ACS Nano* **2012**, *6*, 4603-4614.

232. Rimola, A.; Corno, M.; Marcelo Zicovich-Wilson, C.; Ugliengo, P. Ab initio modeling of protein/biomaterial interactions: Glycine adsorption at hydroxyapatite surfaces. *Journal of the American Chemical Society* **2008**, *130*, 16181-16183.

233. Rimola, A.; Sakhno, Y.; Bertinetti, L.; Lelli, M.; Martra, G.; Ugliengo, P. Toward a surface science model for biology: Glycine adsorption on nanohydroxyapatite with well-defined surfaces. *The Journal of Physical Chemistry Letters* **2011**, *2*, 1390-1394.

234. Weir, A.; Westerhoff, P.; Fabricius, L.; Hristovski, K.; von Goetz, N. Titanium dioxide nanoparticles in food and personal care products. *Environmental Science & Technology* **2012**, *46*, 2242-2250.

235. Li, S.; Hong, M. Protonation, tautomerization, and rotameric structure of histidine: A comprehensive study by magic-angle-spinning solid-state NMR. *Journal of the American Chemical Society* **2011**, *133*, 1534-1544.

236. Feyer, V.; Plekan, O.; Skála, T. s.; Cháb, V. r.; Matolín, V. r.; Prince, K. C. The electronic structure and adsorption geometry of l-Histidine on Cu(110). *The Journal of Physical Chemistry B* **2008**, *112*, 13655-13660.

237. Feyer, V.; Plekan, O.; Tsud, N.; Cháb, V. r.; Matolín, V. r.; Prince, K. C. Adsorption of histidine and histidine-containing peptides on Au(111). *Langmuir* **2010,** *26*, 8606-8613.

238. Özcan, A. A.; Say, R.; Denizli, A.; Ersöz, A. l-Histidine imprinted synthetic receptor for biochromatography applications. *Analytical Chemistry* **2006**, *78*, 7253-7258.

239. Gao, S.; Li, Z.; Zhang, H. Bioinspired green synthesis of nanomaterials and their applications. *Current Nanoscience* **2010**, *6*, 452-468.

240. Durupthy, O.; Bill, J.; Aldinger, F. Bioinspired synthesis of crystalline TiO_2: Effect of amino acids on nanoparticles structure and shape. *Crystal Growth & Design* **2007**, *7*, 2696-2704.

241. Barth, A. The infrared absorption of amino acid side chains. *Progress in Biophysics and Molecular Biology* **2000**, *74*, 141-173.

242. Kitadai, N.; Yokoyama, T.; Nakashima, S. Temperature dependence of molecular structure of dissolved glycine as revealed by ATR-IR spectroscopy. *Journal of Molecular Structure* **2010**, *981*, 179-186.

243. Wolpert, M.; Hellwig, P. Infrared spectra and molar absorption coefficients of the 20 alpha amino acids in aqueous solutions in the spectral range from 1800 to 500 cm^{-1}. *Spectrochimica Acta Part A: Molecular and Biomolecular Spectroscopy* **2006**, *64*, 987-1001.

244. Lausmaa, J.; Löfgren, P.; Kasemo, B. Adsorption and coadsorption of water and glycine on TiO_2. *Journal of Biomedical Materials Research* **1999**, *44*, 227-242.

245. Tsud, N.; Acres, R. G.; Iakhnenko, M.; Mazur, D.; Prince, K. C.; Matolín, V. Bonding of histidine to cerium oxide. *The Journal of Physical Chemistry B* **2013**, *117*, 9182-9193.

246. Xu, M.; Li, J.; Iwai, H.; Mei, Q.; Fujita, D.; Su, H.; Chen, H.; Hanagata, N. Formation of nano-bio-complex as nanomaterials dispersed in a biological solution for understanding nanobiological interactions. *Scientific Reports* **2012**, *2*.

247. Xia, X. R.; Monteiro-Riviere, N. A.; Mathur, S.; Song, X.; Xiao, L.; Oldenberg, S. J.; Fadeel, B.; Riviere, J. E. Mapping the surface adsorption forces of nanomaterials in biological systems. *ACS Nano* **2011**, *5*, 9074-9081.

248. Xia, X.-R.; Monteiro-Riviere, N. A.; Riviere, J. E. An index for characterization of nanomaterials in biological systems. *Nature Nanotechnology* **2010**, *5*, 671-675.

249. Köppen, S.; Bronkalla, O.; Langel, W. Adsorption configurations and energies of amino acids on anatase and rutile surfaces. *The Journal of Physical Chemistry C* **2008**, *112*, 13600-13606.